DEVELOPMENT AND OPTIMIZATION OF HIGH RESOLUTION MULTI-SHOT MAGNETIC RESONANCE ACQUISITIONS FOR DIFFUSION WEIGHTED IMAGING

BY

JOSEPH HOLTROP

DISSERTATION

Submitted in partial fulfillment of the requirements
for the degree of Doctor of Philosophy in Bioengineering
in the Graduate College of the
University of Illinois at Urbana-Champaign, 2016

Urbana, Illinois

Doctoral Committee:

Associate Professor Bradley P Sutton, Chair
Professor Zhi-Pei Liang
Professor Stephen Boppart
Professor Monica Fabiani

Abstract

Diffusion Weighted Imaging (DWI) has become a valuable tool for imaging tissue microstructure, finding use in both clinical and research settings. In order to better resolve finer structures it is desirable to acquire images with higher resolutions. Achieving higher resolutions in diffusion imaging faces several challenges with the primary challenges being low signal to noise ratio and motion induced phase errors. The work in this thesis aims at creating an acquisition that is able to image with a high SNR efficiency in order to achieve higher resolutions. This is accomplished through the use 3D excitations in order to optimize the repetition time in order to operate in a signal to noise ratio efficient regime. High SNR efficiency is also achieved by minimizing TE through the use of spiral readouts. In conjunction with the signal to noise ratio efficiency is the need for motion correction in high resolution diffusion imaging. In this work, the requirements for performing motion correction are analyzed through simulation and in-vivo experiments. The work on motion correction demonstrated the impact that b-value, gradient strength, and cardiac pulsation have on motion induced phase error correction. Results show that a 6 mm resolution navigator is sufficient for correction of motion induced phase errors due to cardiac pulsation at a b-value of 1000 s/mm^2 on most current hardware systems. By combining all the methods used in this dissertation, a high quality diffusion weighted imaging approach that uses a novel pulse sequence was developed that has produced high quality diffusion weighted images at a 0.8 mm isotropic resolution. Additionally this work takes several of the advances used in diffusion weighted imaging and applies them to magnet resonance elastography in order to improve the resolution and spatial coverage achievable with magnetic resonance elastography.

Acknowledgments

I am grateful for the opportunity to pursue a Ph.D. in the department of Bioengineering at the University of Illinois in Urbana-Champaign. I would like to thank my advisor, Brad Sutton, for the opportunity to work with him and provide guidance and funding throughout my time at the University of Illinois. I would specifically like to thank Anh Van who laid out the basic theoretical concepts for my research, Curtis Johnson who allowed me the opportunity to work in the area of magnetic resonance elastography, and the rest of the magnetic resonance functional imagining lab for all the support, discussions, encouragement, and help they provided along the way. I am also thankful for all the people that I have had the opportunity to collaborate with during my time at Illinois. I have been able to publish peer reviewed papers with 29 different people while at Illinois and while there is not space for me to list all of you here, I am extremely grateful for the work you all have done and everything you have taught me. I would like to also thank my committee for their willingness to participate in my Ph.D. work, for guidance they provided, and the insights into what it takes to achieve a Ph.D.

All of the work that I did would not have been possible without the loving support of my family and friends. I am especially thankful for my parents Dave and Judy that initially allowed me the opportunity to attend college and later encouraged me in my pursuit of a Ph.D. My friends have provided a large amount of support and encouragement to me throughout my graduate school career, especially the people within the Illinois GCF and CURL groups. I am finally and most importantly grateful for the work of Jesus Crist in my life. I am thankful for all the gifts and abilities that God has blessed me with and all the opportunities that have been given to not just develop professionally but also to grow and learn on a personal level.

Table of Contents

List of Tables

List of Figures

List of Abbreviations

DTI - Diffusion Tensor Imaging

DWI - Diffusion Weighted Imaging

FA-Fractional Anisotropy

FID – Free Induction Decay

FOV – Field of View

GRAPPA – Generalized Autocalibrating Partially Parallel Acquisitions

MR – Magnetic Resonance

MPE – Motion Induced Phase Errors

PGSE – Pulsed Gradient Spin Echo

PROPPELER – Periodically Rotated Overlapped Parallel Lines with Enhanced Reconstruction

SENSE – Sensitivity Encoding

SNR – Signal to Noise Ratio

TE – Echo Time

TR – Repetition Time

TRSE – Twice Refocused Spin Echo

Chapter 1: Introduction

Motivation

Magnetic resonance (MR) imaging is a powerful imaging modality that is used extensively in both clinical and research settings. The main strengths of the modality come in its ability to provide many different types of contrast *in vivo* without ionizing radiation.

The usefulness of images is highly dependent on the quality of data, both in signal-to-noise ratio (SNR) and imaging resolution, and the information about tissue that it reflects. In this work, the acquisition of data using motion encoding gradients to encode displacement will be assessed. The contrasts available from the motion encoding gradients can give information about microscale restrictions of diffusion, blood flow, or even forced movements of tissues in elastography. These types of contrasts are challenging due to the need to measure motion on the micrometer scale, which results in a low sensitivity signal. In particular, the components that are necessary to acquire high quality data will be analyzed.

Objectives

The objective of this thesis is to outline the parameters and considerations that are necessary for high quality and high spatial resolution diffusion weighted imaging. Based on the considerations, a pulse sequence is proposed that allows for the acquisition of high SNR, high spatial resolution data with motion encoding. The primary objectives that will be addressed are:

- How to achieve a high SNR efficiency
- How to achieve high spatial resolution
- How to minimize artifacts due to motion induced phase errors

Based on the results of the objectives, the ability to use the information from the diffusion weighted imaging acquisition can be applied to other areas, such as magnetic resonance

elastography (MRE) in order to look a fine structures that were previously inaccessible with conventional methods.

Organization of the Dissertation

The thesis is organized to progress through the technical developments that I have achieved in order to enable high resolution diffusion weighted imaging and then demonstrate how they have been applied to a variety of applications spanning from diffusion to blood flow to elastrography. The more specific layout of the thesis is as follows.

Chapter 2 presents background information on MR imaging including data acquisition and how to achieve diffusion weighting. A brief description of the image formation in MR is also given.

Chapter 3 presents the multi-slab multi-shot approach for high-SNR, high-resolution diffusion weighted imaging. This section discusses the motivation for the 3D acquisition and other parameters that need to be considered when designing an acquisition.

In chapter 4, several modifications to the approach proposed in chapter 3 will be discussed to create a multi-band approach that allows for higher acceleration factors and reduced slab boundary artifacts.

Chapter 5 discusses the role of motion induced phase errors in diffusion weighted imaging. Several examples are given to demonstrate how the errors impact data. A discussion of how they impact different acquisitions is given and specifically how they relate to the proposed approaches in chapters 3 and 4.

In chapter 6, the ability to use the lessons learned in diffusion weighted imaging and apply them to MR elastography will be shown.

Chapter 7 provides several concluding remarks and a short summary of key advances in this work. A few possibilities for future work will be presented to give an idea of how this work could be expanded on.

Chapter 2: Background

Magnetic Resonance Imaging

Magnetic resonance imaging is an imaging modality that uses the nuclear magnetic properties of nuclei to acquire information about an object and form an image. It has become popular due its ability to provide a variety of types of contrast while imaging in vivo. In MR, a large static magnetic field is used to align nuclear spins, creating a net magnetic moment vector. By manipulating the magnetic moment through radio frequency (RF) pulses and magnetic field gradients, many different types of contrasts are accessible.

Acquiring MR data

The net magnetic moment vector that is aligned with the main magnetic field can be moved by applying an RF pulse to the magnetic moment vector. By moving the net magnetic moment vector out of alignment with the main magnetic field the net magnetic moment vector will then precess around the main magnetic field, creating an RF signal that can be measured by an RF receiver coil. The rate of precession is proportional to the magnetic field and is equal to $\omega=\gamma B$, where ω is the processional frequency in radians/second, γ is the gyromagnetic ratio, and B is the magnetic field strength. The gyromagnetic ratio is unique for different nuclei, with the most common MR active nuclei being ^{1}H, but other nuclei such as ^{13}C, ^{17}O, and, ^{31}P can also be detected. By applying spatially varying magnetic fields, spins at different positions will precess at different frequencies. In this way, gradient fields are used to encode spatial information in the frequency and phase of the magnetization of the object.

Applying linear magnetic field gradients result in a specific spatial variation in the magnetic field across the object, inducing sine and cosine weightings across the complex-valued magnetization of the object with different spatial frequencies depending on the magnitude and direction of the spatial magnetic field gradients. Because the signal is the sum of the complex net

magnetic moments across the object, the produced signal is related to the spatial frequencies that exist in the distribution of ^{1}H in the contrast weighted object. In MRI, **k** is used to denote a particular, multidimensional spatial frequency of the object. With MRI it is then possible to sample data in spatial frequency domain, or k-space, where the location in k-space is determined by Equation 1. In this equation **G**(t) is an applied magnetic field gradient and k is the location in the spatial frequency domain.

$$\boldsymbol{k}(\tau) = \bar{\gamma} \int_0^{\tau} \boldsymbol{G}(t)\, dt$$

Equation 1

K-space sampling is often divided into two classes based on how k-space is sampled. K-space can be sampled on a Cartesian grid, or raster scanning or k-space can also be sampled using non-Cartesian sampling. The non-Cartesian k-space sampling trajectory can take many forms. Two of the most common non-Cartesian trajectories are radial sampling and spiral sampling. Several common k-space sampling schemes are shown in Figure 1.

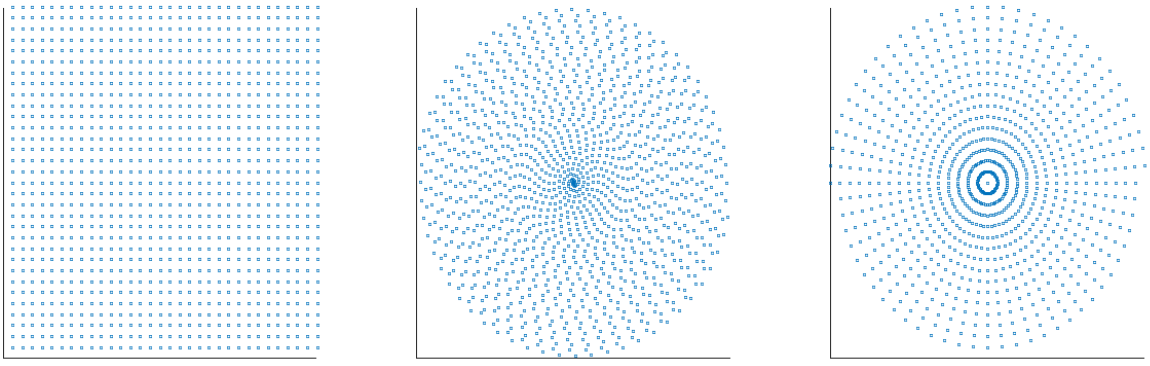

Figure 1: k-space sampling patterns. Cartesian (left), spiral (center), and radial (right)

Image Reconstruction

Image reconstruction in MR imaging aims to determine the most likely image from the k-space sampled data. In the simplest case, k-space data is sampled on a Cartesian grid allowing

reconstruction to be performed using the Fast Fourier Transform (FFT) [1]. If the k-space data was not sampled on a Cartesian grid, a Gridding reconstruction is commonly used to grid the data to Cartesian points before suing a FFT [2, 3].

Another option for image reconstruction that is often used when direct closed formed solutions are not practical is to use iterative techniques. The reconstruction problem can be put into the framework in Equation 2:

$$\hat{f} = \min_{f} \left\| Af - \tilde{Y} \right\|_2^2$$

Equation 2

Where f is s a guess of the contrast weighed object being measured. A is the system matrix representing the imaging physics forward problem, $\hat{f}$ is the object that minimizes the cost function. $\tilde{Y}$ is the measured k-space data.

Equation 2 can be minimized using iterative methods, such as conjugate gradient, when the form of A is not well conditioned and direct closed form solutions are not accurate or computationally efficient. This will result in an estimate for the measured object that best matches the acquired k-space data. By modifying the system matrix or cost function, other information can be incorporated. One possible adjustment is to incorporate coil sensitivities [4] into the system matrix, in this way data from multiple coils can be efficiently combined. Another aspect that can be used is to incorporate field inhomogeneity information [5]. This allows for some of the artifacts due to field inhomogeneity to be corrected. Additionally, the cost function can be modified to include a priori information about likely images, such as incorporation of a roughness penalty [6] to prefer images with smoothness that matches expected medical images.

Diffusion Weighted Imaging

One type of contrast that an MR image can be made sensitive to is the Brownian motion of diffusion [7-9]. In diffusion weighted imaging (DWI), magnetic field gradients are used to make the image contrast sensitive to motion. This diffusion contrast is useful for investigating tissue microstructure and has found many useful applications including stroke imaging [10, 11] and structural connectivity [12, 13].

Diffusion Encoding

Diffusion encoding is accomplished by the use of magnetic field gradients to encode displacement, Figure 2. A gradient is first used to encode the spatial position of protons by changing the phase of the magnetization. A second gradient of equal duration and amplitude and opposite polarity can then be used to undo the spatially varying phase. Any protons that have moved during the application of the gradients or between the gradient encodings will have a different resulting phase based on their net displacement relative to the direction of the motion encoding gradients. In the case of Brownian motion the movement of protons is randomly oriented, the random orientation results in a net signal loss when protons of different phase are summed. The amount of signal loss will depend on the net displacement and on the size of the diffusion weighting gradients. The parameter that describes what motions a DWI acquisition is sensitive to is referred to as the b-value. The amount of diffusion weighting is dependent on the size and timings of the diffusion weighted gradients, Equation 3, where **k**(t) represents the k-space trajectory of the diffusion gradients.

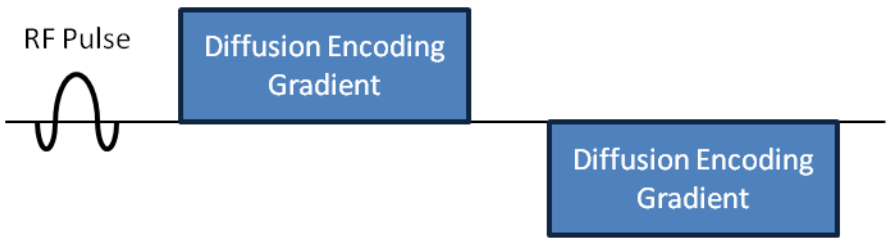

Figure 2: Signal preparation for diffusion weighted imaging

$$b = \int |\boldsymbol{k}(t)|^2 dt$$

Equation 3

The pulsed gradient spin echo (PGSE) sequence[14], Figure 3, is one of the earliest and most efficient methods to create diffusion weighting. The PGSE sequence uses two gradients of the same polarity with a 180° pulse between them. By placing the 180° pulse between the gradients a spin echo sequence is created that allows the sequence to have T2 weighting, enabling longer echo times and larger amounts of diffusion encoding to be used than what would be capable of in a gradient echo sequence. The b-value for a PGSE can be calculated using a simple equation, Equation 4. In this equation G is the strength of the diffusion weighted gradients, δ is the duration of a single diffusion weighting gradient, and Δ is the time between the start of the two diffusion weighting gradients.

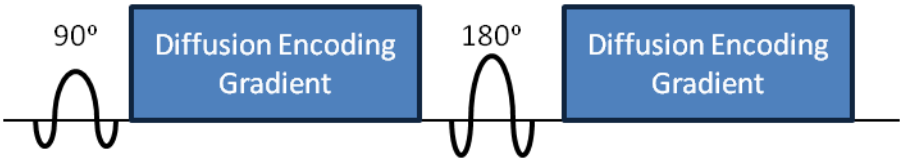

Figure 3: Pulsed gradient spin echo sequence

$$b = \gamma^2 G^2 \delta^2 (\Delta - \frac{\delta}{3})$$

Equation 4

There are several other diffusion encoding schemes that are also sometimes used. The twice refocused spin echo (TRSE) sequence [15] uses two 180° pulses to create a sequence that is more immune to eddy current effects. There have also been several techniques that have been used with a single 180° pulses to minimize eddy currents by using more than 2 diffusion gradients [16] . For some applications having shorter or longer time for the diffusion process to occur has led to

the oscillating gradient spin-echo (OGSE) [17] and stimulated echo acquisition mode (STEAM) [8, 18] acquisitions respectively.

Applications of diffusion weighted imaging

Diffusion weighted imaging provides a valuable type of contrast that has found extensive use in both clinical and research settings. In the clinical setting, the most common application of DWI has been the assessment of brain tissue after a stroke [10, 11, 19, 20]. While T1 and T2 weighted images provide little contrast immediately after a stroke, DWI provides a strong contrast as there are changes that impact the amount of intracellular fluid after a stroke. The diffusion weighted signal also changes in the weeks following a stroke to give a more clear view of the extent of tissue damage than other contrast types.

On the research side, diffusion weighted imaging is most commonly used to assess white matter integrity and structural connectivity [12, 13, 21-23]. In these approaches, the restrictions to diffusion within axons are measured in multiple orientations. From looking at many different orientations of restrictions, models of the white matter structure and integrity are made. The most commonly used method for modeling the signal in diffusion imaging is diffusion tensor imaging [24]. The tensor model uses a 3 x 3 tensor matrix to describe the magnitude of the diffusion in different directions. By taking the eigenvector of the tensor matrix the main orientation of diffusion can be determined, allowing information about the orientation of axons to be determined. By taking the eigenvalue of the tensor matrix the amount of diffusion in different directions can be determined. The amount of diffusion in the main direction of diffusion is commonly known as axial diffusivity. The average of the diffusion perpendicular to the axial diffusivity is known as the radial diffusivity. The average of the diffusion in all 3 directions is known as the mean diffusivity. All three of these parameters have been used as biomarkers of tissue microstructure. One common interpretation is that in the case of demyelination of a neural pathway the axial

diffusivity is unchanged while radial diffusivity increases [22]. Another commonly used metric in diffusion tensor imaging is fractional anisotropy (FA). Fractional anisotropy is a measure of how directed the diffusion is. For example a tissue where diffusion is primarily in one direction would have a FA of close to 1 where a tissue with diffusion equal in all direction would have an FA of 0. Axonal pathways where the diffusion is primarily in one direction have a high value for FA, Figure 4. Based on the orientation information of the axonal pathways in the brain, models of the pathways and their structural connectivity can be made using diffusion weighted imaging, Figure 5.

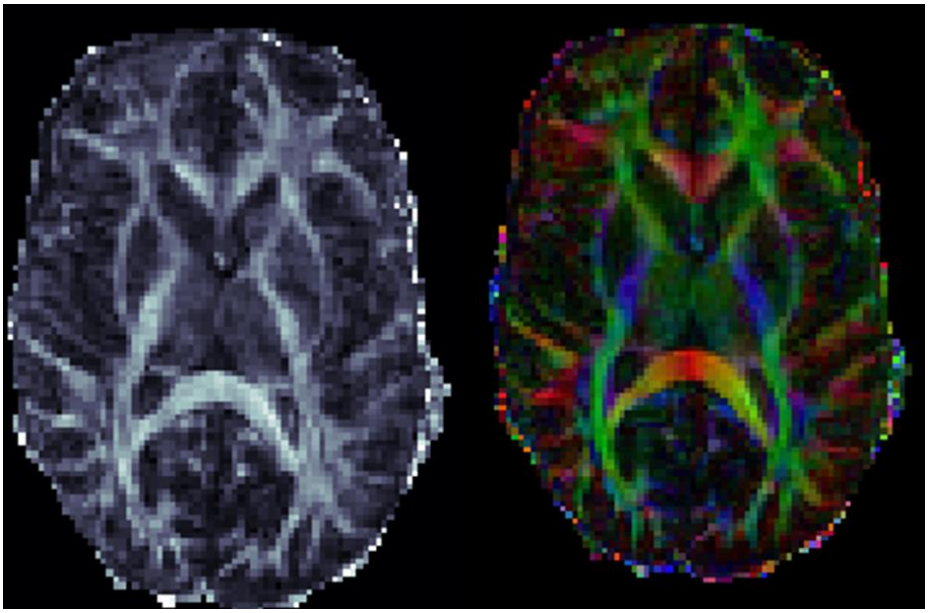

Figure 4: Fractional anisotropy image of an axial slice. The color on the right indicate the main direction of diffusion: read (left/right), green (anterior/superior), and blue (inferior/superior).

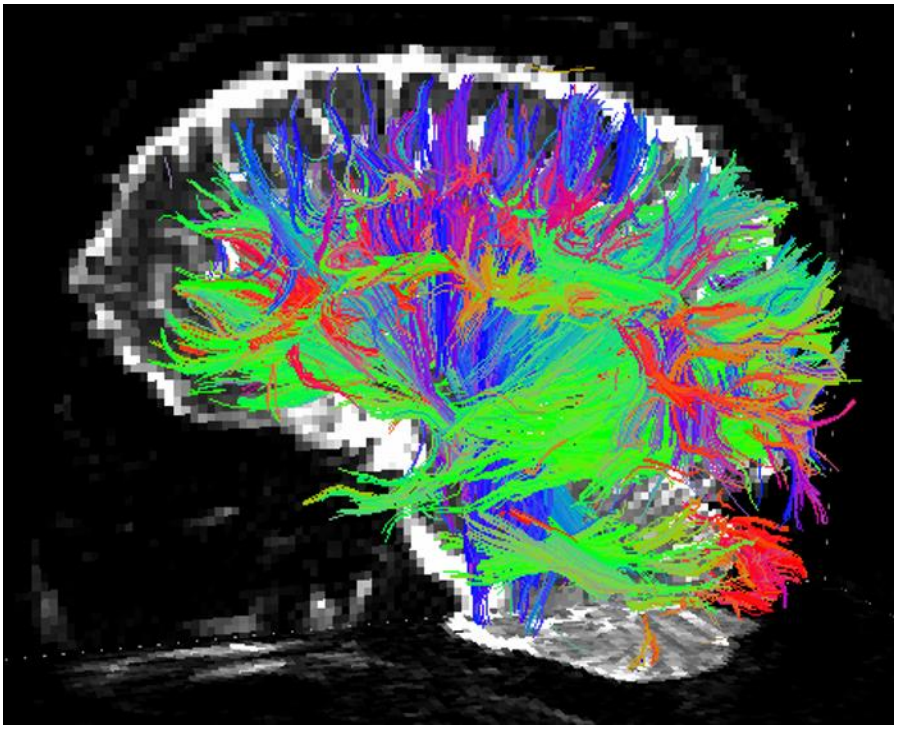

Figure 5: Pathways in the brain from deterministic tractography.

A specific example of what can be done using diffusion weighted imaging includes the ability to investigate fine motor pathways [25]. In this study, tractography using diffusion weighted imaging was used to identify separate neural pathways used for fine motor control of the finger, lips, and tongue, Figure 6. From the identified tracks, metrics of neural structure through the diffusion tensor model were able to be extracted to make conclusions about the relationship between the structural integrity of the identified motor neural pathways and changes in fine motor control with age.

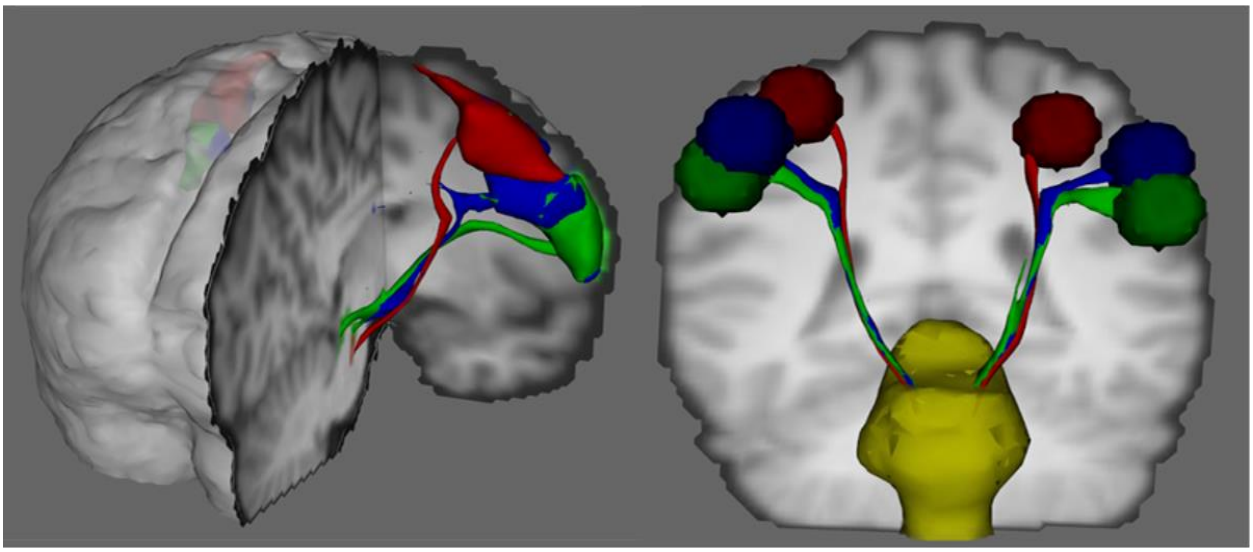

Figure 6: Tractography results connecting regions in the motor cortex to the brainstem for the finger (red), lips (red), and tongue (green).

The use of the DTI model has been the most commonly used model to study diffusion in the brain, however a wide range of other models have emerged and are seeing increased use to provide other information including neurite orientation dispersion and density imaging (NODDI) [26], composite hindered and restricted model of diffusion (CHARMED) [27], intra voxel incoherent motion (IVIM) [28]. While the primary use of diffusion imaging has been in the brain, it has found use in imaging other tissue types. DWI has also been used in muscle as a biomarker of muscle health [29-31]. Due to the orientation dependence of muscle fibers, the directional dependence of DWI make it useful for modeling muscle tissue. The areas that diffusion weighted imaging are being used continues to grow and includes many areas including: cancer [32-34], liver [35, 36], heart [37, 38], and many more.

Motion Induced Phase Error

While diffusion weighted imaging has mainly used single shot imaging in the past, there has been increasing desire to go to higher spatial resolutions leading to a need for multi-shot imaging sequences to prevent artifacts associated with long data readouts. While multi-shot DWI has the potential to capitalize on the benefits of decreased distortion due to field inhomogeneity

and ability to acquire higher resolutions, it faces a unique the additional challenge of motion induced phase error that is not found in most other MRI imaging techniques.

In diffusion weighted imaging gradients are used to sensitize the acquisition to motion. Typically, the motion of interest is the Brownian motion of water, which manifests as a loss in signal intensity when diffusion weighted imaging gradients are used. However, the gradients used in DWI are similar to the ones used in velocity encoding and in addition to being sensitive to Brownian motion, are also sensitive other forms of motion. If the motion is coherent, the motion during the motion encoding gradients changes the phase of the object.

The signal received in diffusion weighted imaging follows Equation 5.

$$s(t,m) = \int_{-\infty}^{\infty} I_{b0}(r) e^{i\varphi(r,m)} e^{-bD(r)} e^{-i2\pi k(t,m)r} dr$$

Equation 5

Equation 5 relates the signal from an image with no diffusion weighting I_{b0} to the received signal from the diffusion weighting. The $e^{i\varphi(r,m)}$ describes the phase due to coherent motion during the diffusion encoding. $\varphi(r,m)$ is the resulting phase from the coherent motion at the r^{th} spatial location for the m^{th} shot. The $e^{-bD(r)}$ is the amount of signal loss due to incoherent motion of molecules within a voxel. The final term, along with the integration, describes the Fourier encoding of the object into k-space. Without coherent motion, $\varphi(r,m)$ would be zero and therefore is refrenced as the motion induced phase error (MPE) throughout this work.

The phase caused by differences in motion induced phase errors from different shots will cause artifacts in reconstructed images if not accounted for, as shown in Figure 7. This section will review several of the approaches used for motion induced phase error correction, then proceed to discuss considerations that need to be made when designed a pulse sequence.

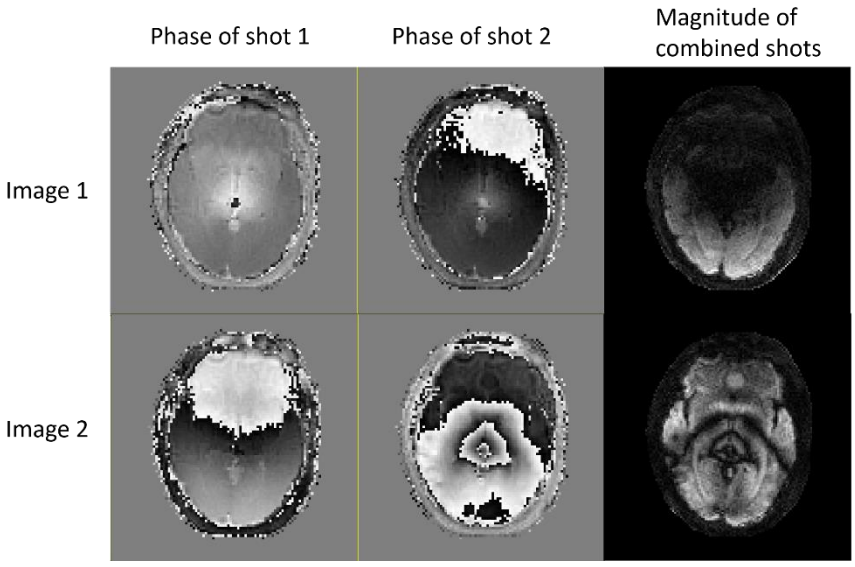

Figure 7: Diffusion weighted imaging with motion induced phase error.

Due to the errors that can result from combining shots with different amounts of coherent phase, methods to correct for the artifacts associated with this problem have been developed. These methods generally involve collecting information about $\varphi(r,m)$ through some sort of navigator and applying some correction to the data to reduce artifacts. The coherent phase can come from any movement during the diffusion encoding gradient, however the most common sources are due to rigid body motion of the head due to small movements by the subject and the non-rigid pulsatile motion of the brainstem due to cardiac pulsation.

Methods to remove motion induced phase errors

A wide variety of methods have been developed that allow for correction of artifacts associated with motion induced phase error [39-59]. These are commonly divided into 3 classes: separate navigator, self-navigated, and navigator free, based on where the information to correct for MPE comes from. However, the distinctions between these 3 classes has become increasingly vague as some newer methods fall in between these classifications. The major methods are explained here with more emphasis being placed on how the MPE is corrected and less on classifying on where the information comes form.

Direct Phase Subtraction

Several different approaches have been developed that rely on the concept of direct phase subtraction [40, 60, 61] which corrects for the MPE in image space. While the specific sequence implementation varies depending on how navigator data for each shot is acquired, separate navigator or self-navigating through variable density spiral or PROPELLER, the main idea in image reconstruction is the same. The forward signal model is defined by the linear relationship in Equation 6.

$$y = FPx$$

Equation 6

If *M* shots are used to acquire the data and there are D k-space data points in each shot, y is the acquired k-space that is a MDx1 vector. x is an Nx1 vector where N represents the number of voxels in the image. P represents the object motion induced phase that is unique to each shot and has dimensions MN x N. The Fourier encoding is described by F, depending on the k-space trajectory used there are several efficient options for this operator are possible. In the most general case F is a block-diagonal combination of M discrete Fourier transforms with dimensions MD x MN.

$$\hat{x} = (P^H F^H FP)^{-1} P^H F^H y$$

Equation 7

Descriptively this approach results in taking aliased images from each shot and then subtracting the measured MPE from each shot. The shots are then added back together to create an alias free image. If the estimated MPE is not correct, the resulting images will have residual aliasing that has not been corrected for. This method is most commonly used in cases where the image reconstruction is well conditioned such as with fully sampled Cartesian trajectories.

Iterative Reconstruction with Phase Correction

The direct phase subtraction method can face challenges with the inversion step in the reconstruction when inverse term cannot be approximated by an identity matrix. When the encoding matrix becomes large, it becomes impractical to perform the inverse operation in Equation 6. Due to this challenge the CG phase method was developed [41], this method is similar to the commonly used CG-SENSE formulation for parallel imaging. Instead of directly solving Equation 6, the CG phase correction method solves Equation 8 using iterative methods.

$$P^H F^H F P x = P^H F^H y$$

Equation 8

This method is most frequently used in cases were non-Cartesian data readouts are used. The CG phase method is desirable as it does have any limitations on how k-space is sampled, unlike many direct phase subtraction methods where a continuous section of k-space needs to be sampled, in order to provide the correction over a unaliased field of view.

Other methods

There are also methods that can be applied that perform the motion correction in k-space [46, 47, 62, 63]. If the phase due to coherent motion is due to rigid body the resulting signal only results in shifts in k-space and a phase offset for rotations and translations respectively [64]. Equation 9 shows the signal formulation in the case of rigid body motion. Instead of the spatially varying phase due to coherent motion there is now just an offset $\Delta\varphi(m)$ for each shot. The k-space is also now shifted for each shot. This formulation is useful in cases where only rigid body motion is present and is convenient because it is easily extendable to 3D imaging methods.

$$s(t,m) = \int_{-\infty}^{\infty} I_{b0}(r) e^{i\Delta\varphi(m)} e^{-bD(r)} e^{-i2\pi(k(t,m)+\Delta k(m))r} dr$$

Equation 9

Another approach that is commonly used when cardiac motion is the primary type of motion of concern is to either do cardiac reordering of shots or reacquisition of shots [59]. Because the amount of phase variations will be larger during pulsation, one method that can be used is to acquire the "important" shots at times when there is minimal cardiac motion. This is done by using cardiac gating to predict when the cardiac motion will occur and then avoid acquiring the "important" central parts of k-space during this time period. Additionally, cardiac gating could be used to ensure that the cardiac pulsation is avoid, however that increases scan time and can have an impact on steady state signal fluctuations [65].

Another method that is sometimes used is to reacquire shots that have been corrupted by motion induced phase [59]. This can be assessed by examining a low resolution navigator image, the point spread of the k-space data, or by looking at cardiac cycle information through PPG, ECG, or other motion tracking devices. Figure 8 shows an example of phase images with diffusion encoding and the associated k-space data. From these images it can be observed that images with more complex phase patters have a wider spread in k-space. Based on this type of analysis a variety of criteria have made for reacquiring data. The reacquisition of data will have the downside of increased scan time.

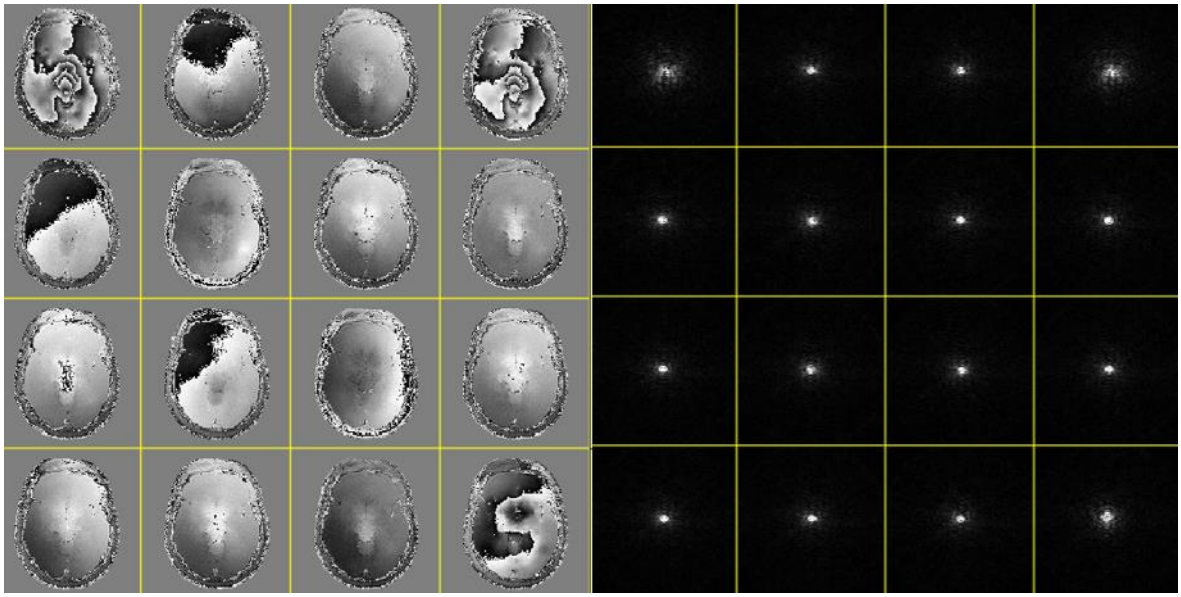

Figure 8: Phase maps (left) and the corresponding k-space data (right) from a 16 repeats of the same slice with diffusion weighting.

There has recently been several proposals to use a GRAPPA based framework to correct for the MPE [66, 67]. These methods rely on acquiring a new grappa kernel for each shot that captures the phase variation. These methods show good promise, but due to their recent development still require more testing

Chapter 3: Spiral Multi-slab Diffusion Weighted Imaging[1]

Motivation

For both clinical and research applications, the desire for improved spatial resolutions has driven technological developments in diffusion weighted imaging. Researchers and clinicians want to study fine-scale structures that have important functional implications in the brain and reduce the partial-voluming effect from other structures. Many approaches have been proposed to address the challenges of high quality diffusion weighted imaging and have included specialized scanning hardware, pulse sequence modifications, and image reconstruction advances [68].

With the advent of the human connectome MRI scanner [69], much of the improvements in diffusion imaging have focused on improved hardware, while better hardware does provide an advantage it is often not a practical approach for someone that already has an MR system. In this work several approaches to design an acquisition will be outlined that do not require new hardware to implement.

SNR Analysis

The addition of diffusion weighting contrasts inherently lowers the signal of a diffusion weighted image. For example, if an acquisition had a b-value of 1000 s/mm^2 and the object being imaged had a diffusion coefficient of 1 μm^2/ms, the resulting image would have 37% of the original signal, making diffusion weighted imaging have inherently lower signal than standard structural images without diffusion contrast.

[1] Portions of this chapter are adapted from Holtrop, J. L. and B. P. Sutton "High spatial resolution diffusion weighted imaging on clinical 3 T MRI scanners using multislab spiral acquisitions." Journal of Medical Imaging (2016), **3**(2): 023501-023501.

Two main relationships are important for optimizing the SNR for a diffusion weighted imaging scheme. The first relationship is the amount of signal based on the T2 and T1 of the object being imaged, along with the impact of acquisition parameters of TR and TE. For a spin echo pulse sequence acquisition, which is commonly used in diffusion, the amount of signal, S, follows the relationship in Equation 10:

$$s \propto (1 - 2e^{-(TR-\frac{TE}{2})/T1} + e^{-TR/T1})e^{-TE/T2}$$

Equation 10

where T1 and T2 would be the relaxation parameters of white matter at 3 T for our particular case, as white matter is usually the target for diffusion weighted imaging in the brain. To increase the signal with this relationship the repetition time should be made as long as possible and the echo time should be made as short as possible. Performing these optimizations will produce the highest signal from a signal recovery perspective. However, the time spent acquiring data and how the data is collected also needs to be considered.

$$SNR \propto \Delta V \sqrt{T_{acq}}$$

Equation 11

Equation 11 gives the relationship for the SNR when the voxel volume, ΔV, and time spent acquiring data for an image, T_{acq}, are considered. The voxel volume is important as it highlights the challenge of achieving higher resolutions. For example, if the resolution was decreased by a factor of 2 in each dimension the resulting voxel volume would be one-eighth and would have one-eighth the SNR. The challenge of recovering the SNR that is lost due to the increase in spatial resolution is demonstrated by T_{acq}. In order to maintain the SNR in the example, the total acquisition time would need to be increased by a factor of 64 to maintain SNR with the new resolution.

There are several subtleties about the T_{acq} parameter that need to be considered when assessing this relationship. The T_{acq} duration can be changed in variety of ways. One way that T_{acq} can be increased is to increase the length of an ADC readout, or how long the data acquisition card is turned on for sampling data. When this is done, more data is acquired for every excitation of the object. From an SNR perspective the longer the readout the higher the SNR would be. However in practicality there are limitation on the length of data readouts. The two main limitations to the readout duration are signal decay and field inhomogeneity. As the readout is made longer, the T2 and T2* decay will cause a loss of signal. If the readout is long enough this would result in the signal dissipating as the signal returns to steady state. Additionally with long readouts, depending on the trajectory, there is concern about mismatch in k-space as points at the beginning and end of the readout will have different amounts of weighting from T2 and T2*.

Often the bigger limitation of readout duration is magnetic field inhomogeneity and off-resonance spins. Due to differences in magnetic susceptibility between air and tissue spaces in and around the brain, the magnetic field experienced in some voxels will not be determined solely by the main field and spatial field gradients. Off-resonance during a readout will cause a signal variation through time that can create artifacts in resulting images. In EPI scans these often appear as ghosting in the phase encode direction [70], in spiral the artifact appears more as a radial blur [71]. Because of these effects, readout durations are often limited. However the length of readout duration can be increased by using techniques that correct for off resonance artifacts.

The other way to increase T_{acq} is to excite the object a larger number of times and acquire k-space data for the object again. The extra data could be repeats of the same k-space data, which can be considered just averaging, or could be data from a new part of k-space. In the formulation used here, there is no difference in SNR from averaging compared to covering new parts of k-

space. However in practice the k-space coverage needs to be considered more carefully. The way k-space is covered has the potential to impact estimated images, especially in under sampled cases, with different trajectories having the potential for different artifacts and noise amplification based on the part of k-space that was covered.

The use of multiple excitations interferes with the optimization of Equation 10 as full T1 recovery can no longer be achieved. To demonstrate the trade-off for repetition time between Equation 10and Equation 11 several simulations are demonstrated. These equations use white matter values of 1.1 s for T1 and 69 ms for T2 [72] at 3T. In order to look at the impact of field strength, the field strengths of 1.5T and 9.4T will also be shown in simulation with values of 0.79 s for T1 and 90 ms for T2 at 1.5T and 1.8 s for T1 and 45 ms for T2 at 9.4 T.

Impact of repetition time

If we first look at Equation 10, an idea about the TR needed can be gained. Figure 9 shows the amount of signal that has recovered using different repetition times at three different field strengths. From this figure it can be seen that, at 3 T, after 2.5 seconds the white matter has already recovered 90% of the signal and at a TR of 5 seconds 99% of the signal has recovered, this would mean that any additional time spent waiting for signal recovery after these times would not lead to significant increases in signal. Looking at the different field strengths it can also be seen that at higher field strengths more time is needed for signal recovery.

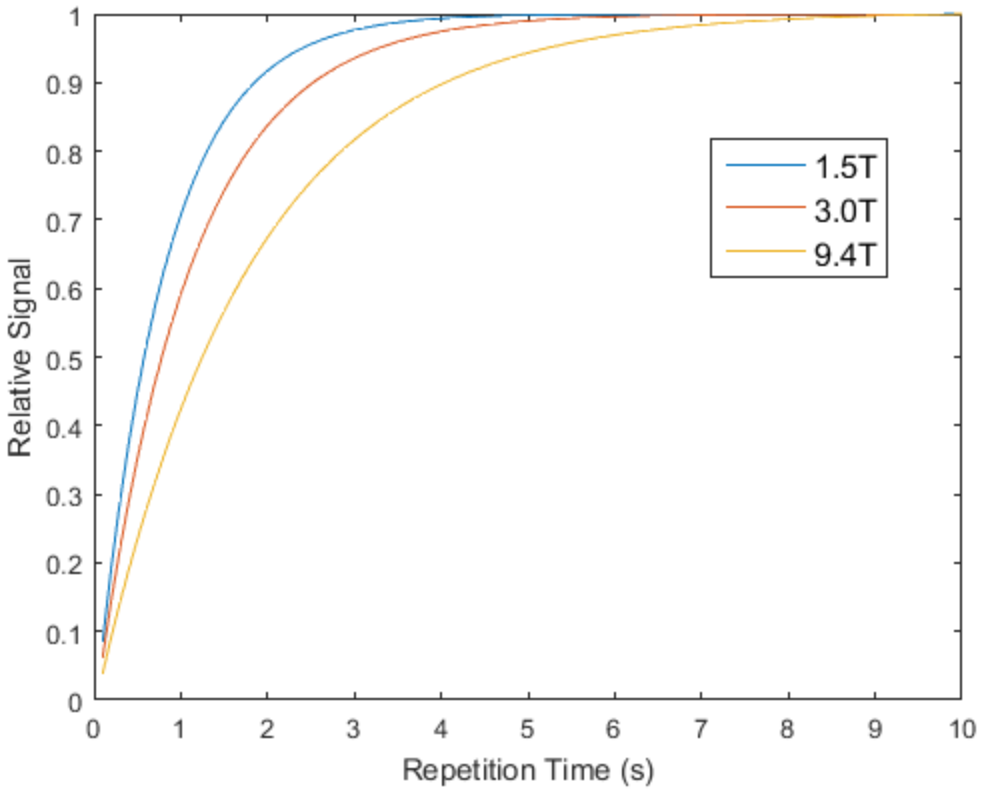

Figure 9: Signal recovery for a spin echo

Impact of echo time

The T2 decay (or T2* when it is significantly shorter) will determine how long the transverse magnetization lasts. In Figure 10 the amount of signal remaining due to T2 decay at various field strengths is given. The exponential loss of signal can be clearly seen from the graph. The rapid loss of signal is important in diffusion weighted imaging as achieving a short TE has a major impact on the signal level. By looking at the different fields it can be seen that lower field strengths do not decay as rapidly, causing the signal decay factor to be even more important at higher field strengths.

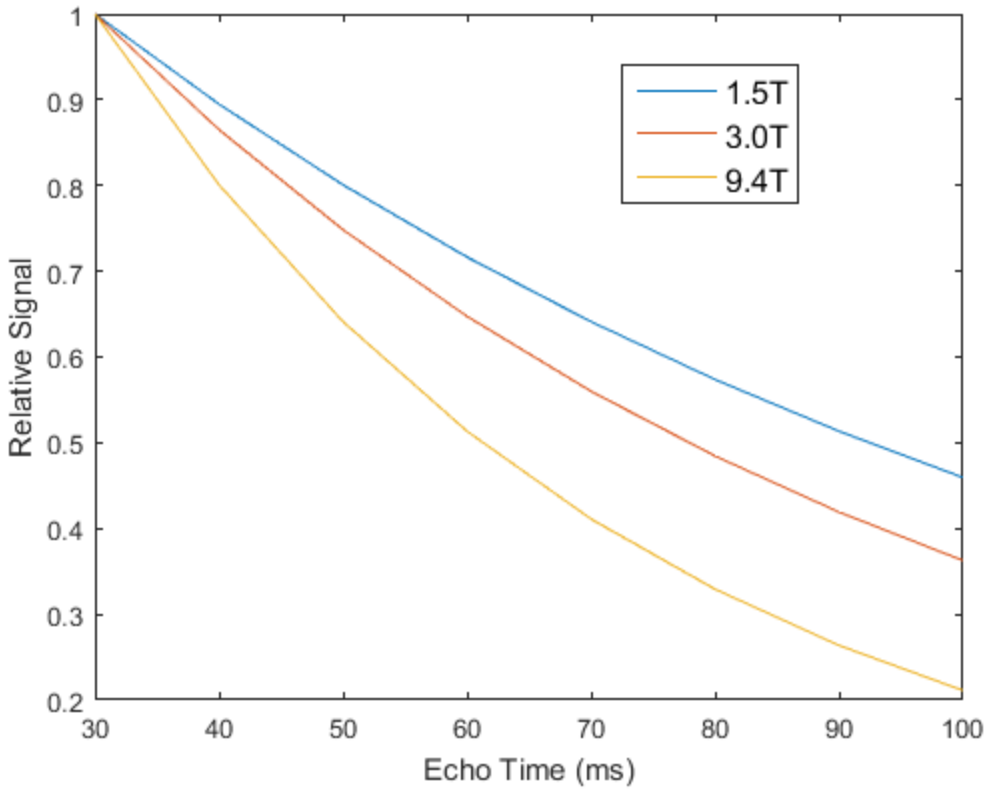

Figure 10: T2 signal decay for white matter at 1.5T, 3.0T, and 9.4T

Overall SNR efficiency

If the signal recovery and decay is considered in conjunction with how often data is collected, as in Equation 7, the optimal TR for an acquisition can be determined. Figure 11 shows the SNR efficiency where the values for each field strength are normalized by the max efficiency for each field strength. At 1.5 T the most efficient TR is at 1 second, 1.5 seconds at 3 T, and 2.5 seconds at 9.4 T. At these target TRs the SNR efficiency is the highest and an acquisition that uses this TR will be as SNR efficient as possible from a signal recovery and averaging perspective, given a fixed amount of scan time

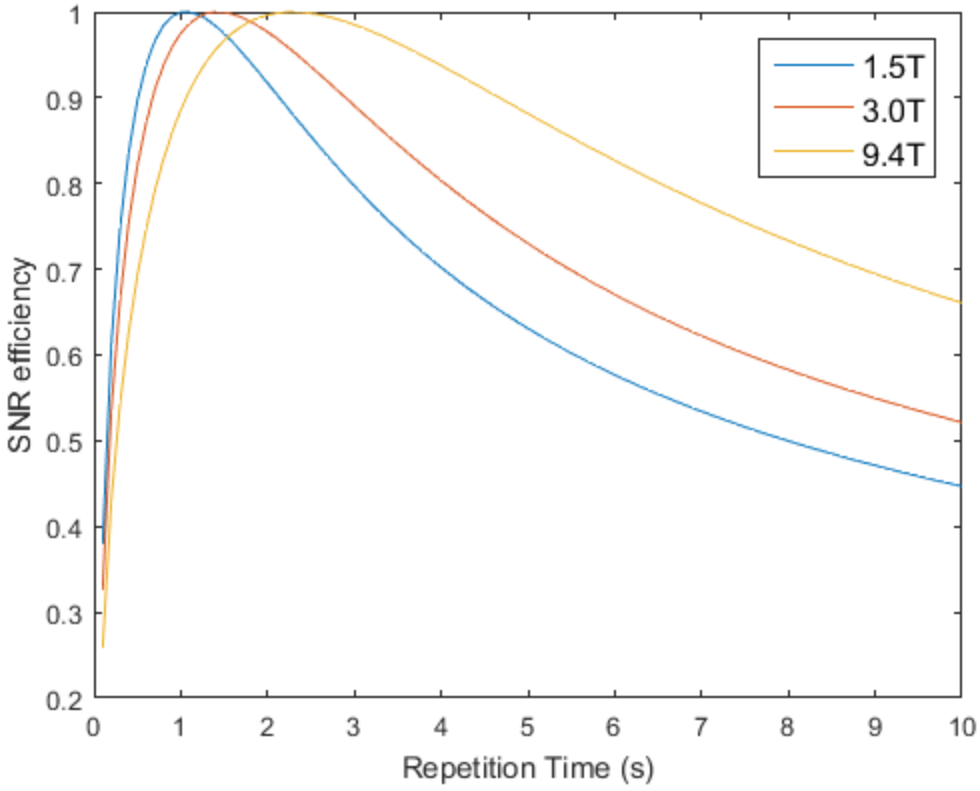

Figure 11: SNR efficiency of imaging white matter at 1.5T, 3.0T and 9.4T

The one parameter that is not included in Figure 11 is the impact of TE, However if we are only concerned about the location of the peak of the SNR efficiency curve and not the amplitude, Figure 12 can be used. From Figure 12 it can be seen that the TE has basically no impact on the selection of TR. This relationship will remain true for a spin echo sequence as while the TE is small relative to T1 recovery.

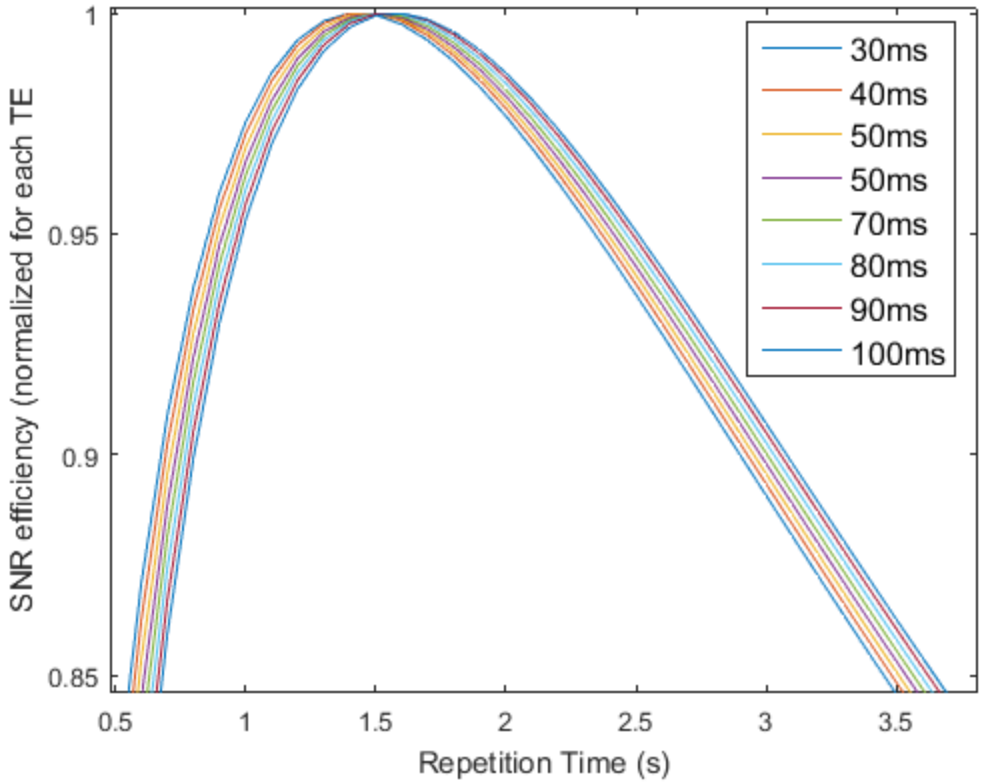

Figure 12: Normalized SNR efficiency at 3T with different echo times

The TE that is able to be achieved will primarily be determined by the hardware along with several choices about diffusion encoding and k-space trajectory that will be discussed in future sections. With these considerations the position of the peak is more important than the relative size of the signal for maximizing SNR. However when the signal loss due to T2 decay is displayed along with the impact of SNR a more clear perspective on all the tradeoffs can be seen, as shown in Figure 13. Figure 13 reinforces the fact that changing the TE does not change the optimal TR, but it additionally shows how large of an effect having a shorter TE has on the SNR efficiency. For example, if a 50 ms TE is being used, it will be always achieve a higher SNR than a 100 ms TE for all the TRs investigated here. This is important as it shows that being able to achieve a short TE is extremely important. However, the TR is still a very important determinant of SNR efficiency as it can give a 45% increase in signal from a 10 second TR to an optimal TR.

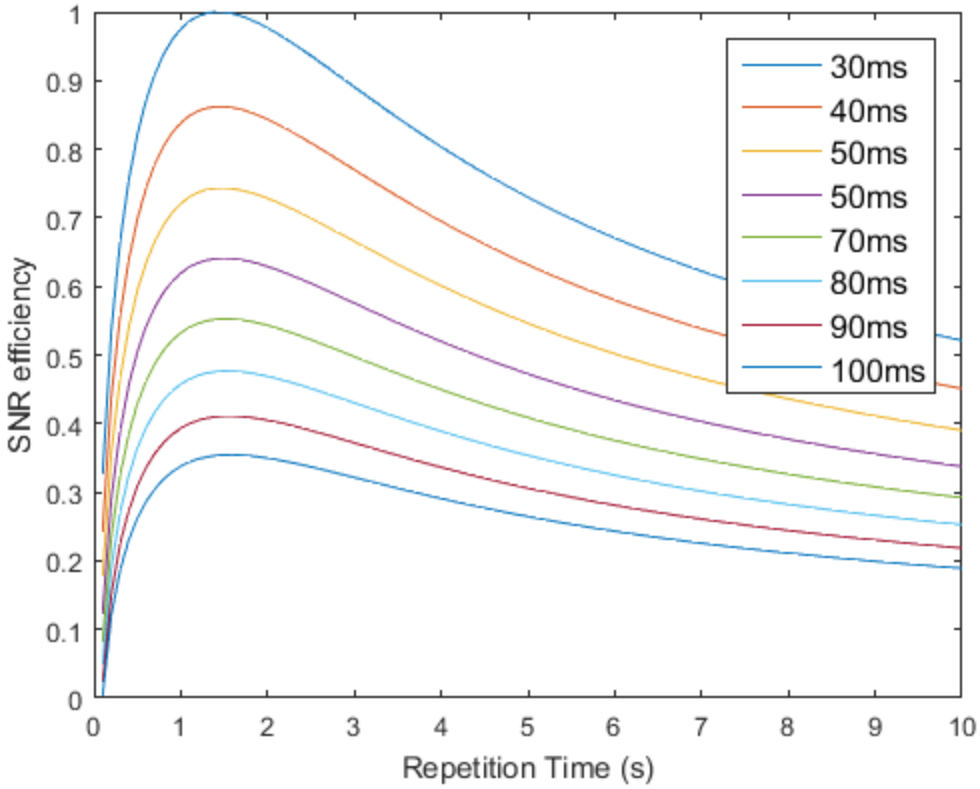

Figure 13: SNR efficiency at 3T at different echo times

SNR efficiency for other tissue types

All of the above results presented were based on imaging white matter in the brain. White matter is the mostly commonly studied area in research settings in the brain, however diffusion imaging is also used in a variety of other applications. To provide a reference for other tissue types, several other graphs of SNR efficiency are given here. The T1 and T2 values used are in Table 1[72].

Table 1: T1 and T2 of various Tissues at 3T

	T1 (ms)	T2 (ms)
Liver	812	42
Skeletal muscle	1412	50
Heart	1471	47
Kidney	1194	56
Gray matter	1820	99
Blood	1932	275

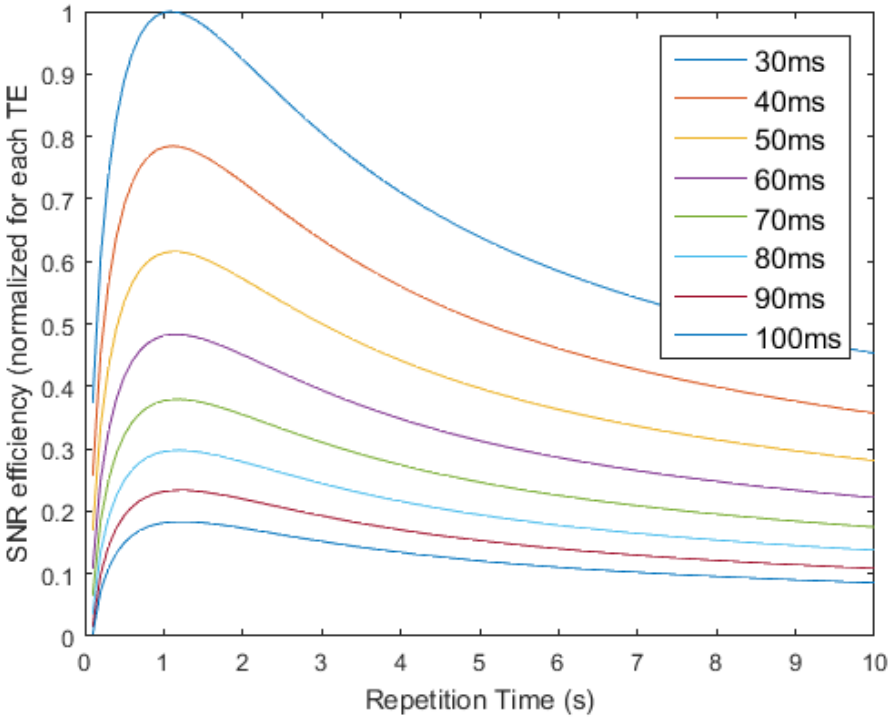

Figure 14: SNR Efficiency of Liver at 3T

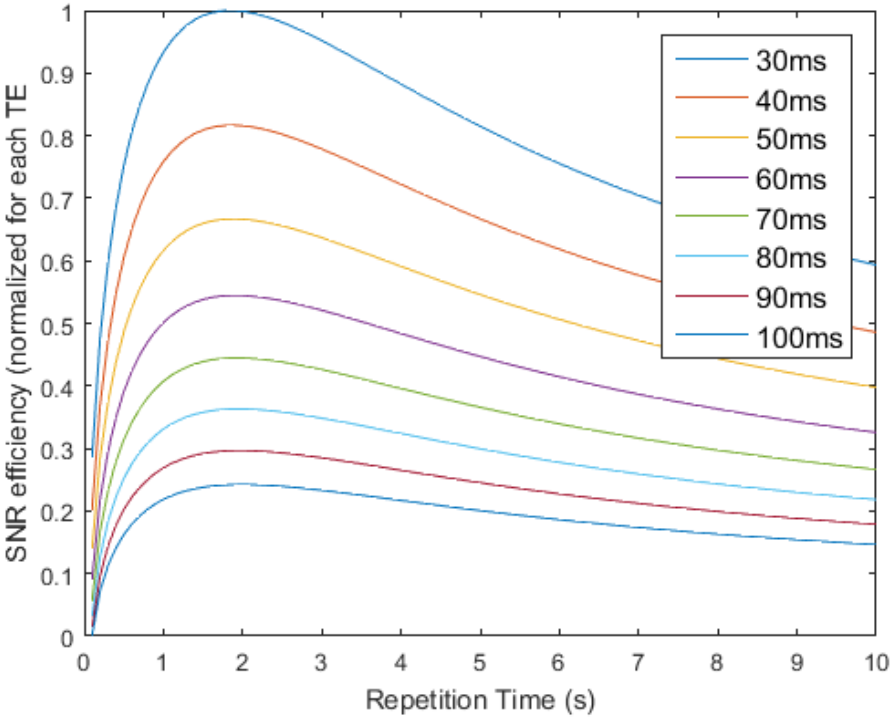

Figure 15: SNR Efficiency of skeletal muscle at 3T

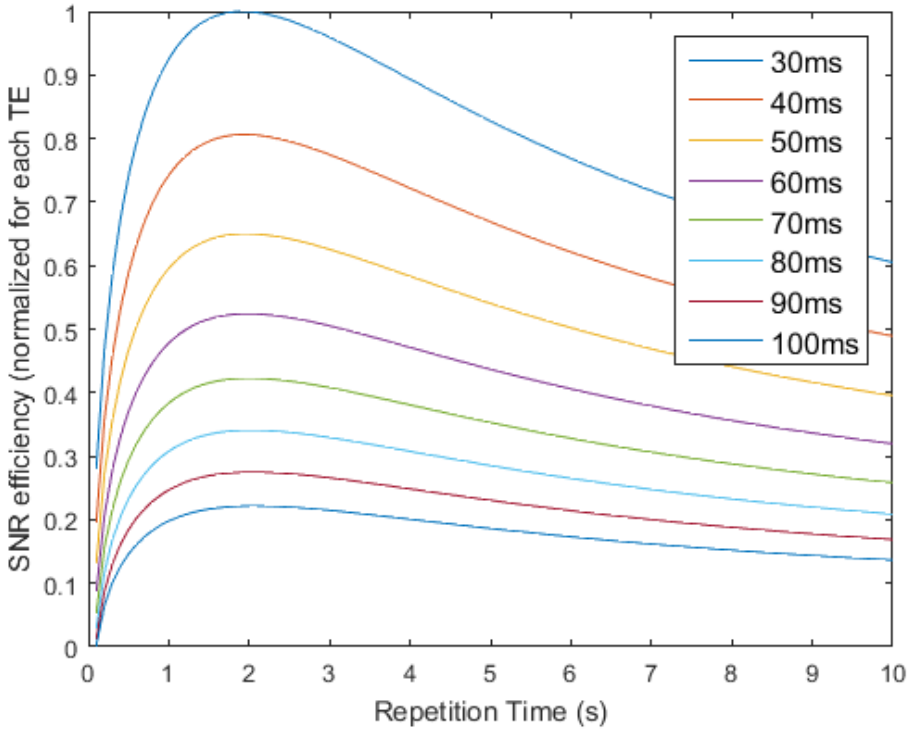

Figure 16: SNR Efficiency of heart at 3T

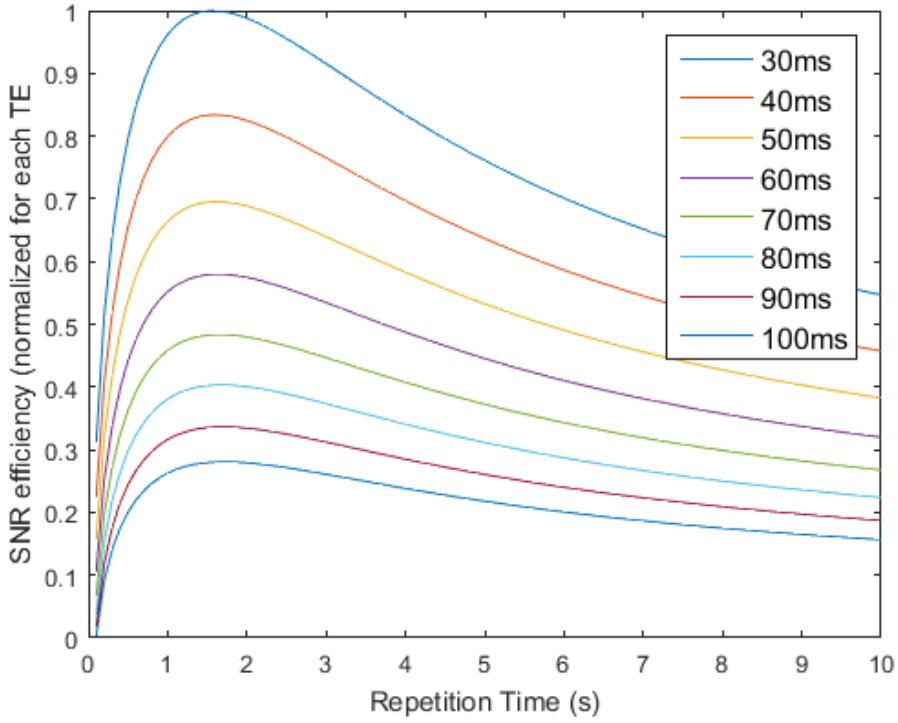

Figure 17: SNR Efficiency of kidney at 3T

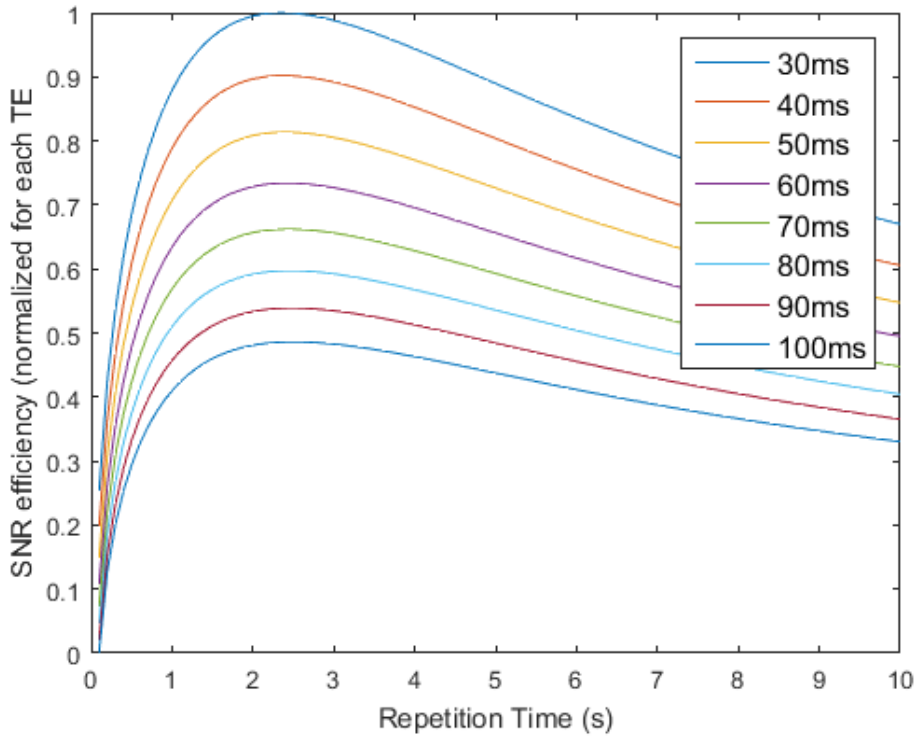

Figure 18: SNR Efficiency of gray matter at 3T

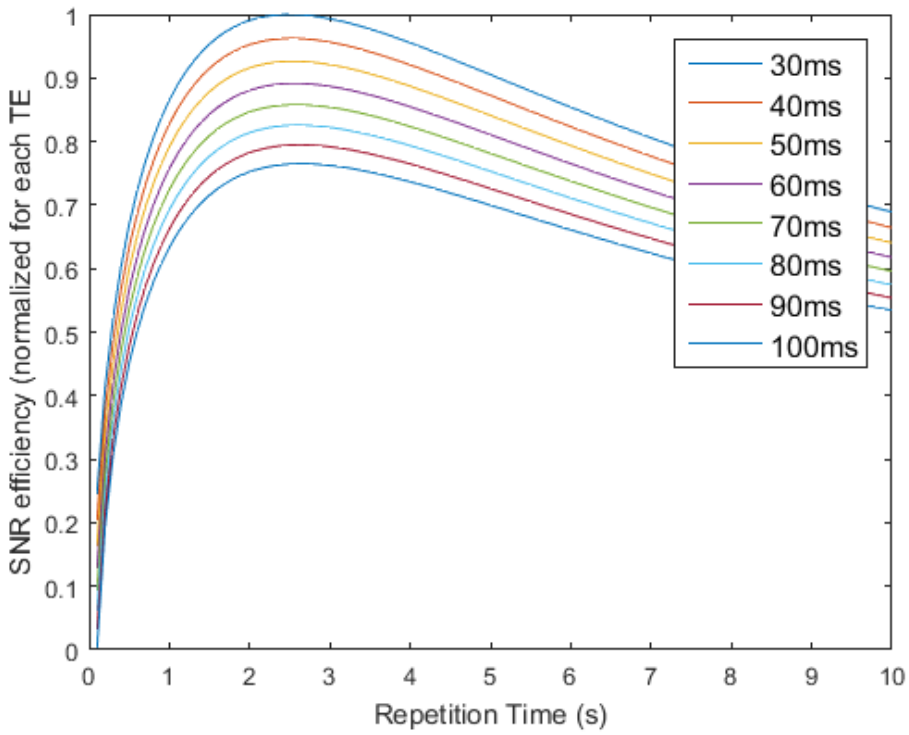

Figure 19: SNR Efficiency of blood at 3T

These plots of SNR efficiency other tissues provide several interesting insights into optimizing SNR. For tissues with short T2 signal decay, such as liver and skeletal muscle, the gain in SNR efficiency by using a shorter TE is much larger than in tissues with longer T2 signal decay. Also of interest is that the peak TR is different for the different tissues types. When imaging organs such as the brain consideration may need to be made in regards to which tissue type to optimize SNR for as the brain contains white matter, gray matter, and blood that have different peak SNR efficiencies.

3D k-space encoding for optimal repetition time

From Figure 13 a sequence that is able to achieve a TR of 1.5s is desired as it will be the most SNR efficient. If slice coverage is not a concern, i.e. a limited imaging volume is desired, then this can be accomplished by a standard 2D imaging approach. When many slices are desired the short TR is not possible and multiple slices must be excited simultaneously, this can be

accomplished by grouping slices into 3D slabs. By switching to a 3D excitation scheme which samples data for multiple slices in a 3D volume, the SNR efficiency can be increased by 50% or more in the same total imaging time compared to a standard 2D acquisition when imaging a large number of slices [73-76].

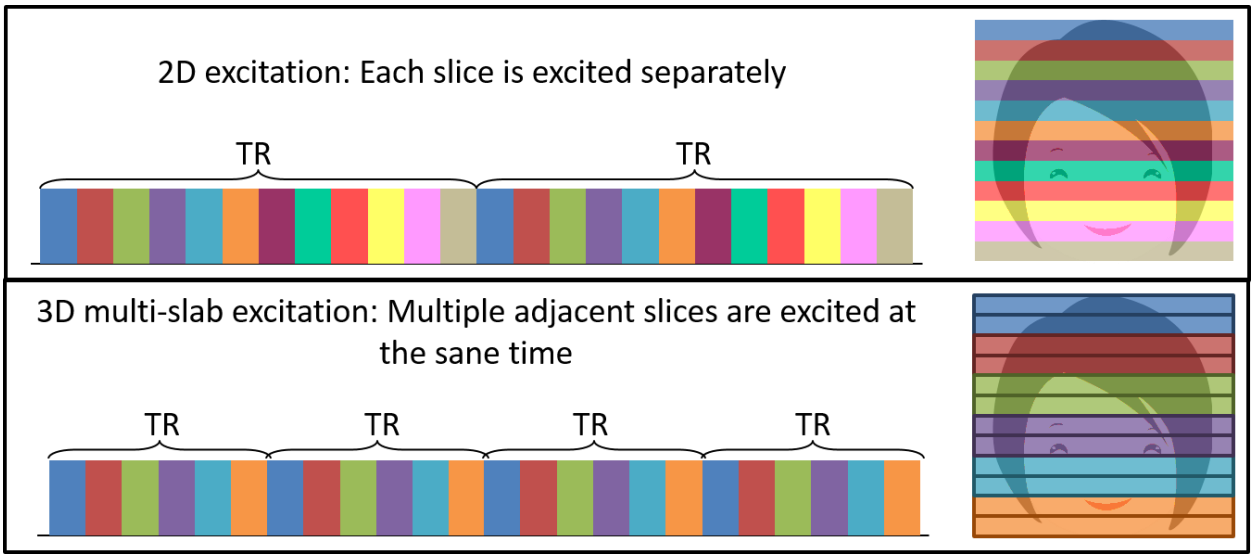

Figure 20: Diagram of multi-band excitation. A standard 2D excitation is shown on top and the 3D multi-slab excitation is on the bottom panel. Slices that are excited with the same excitation pulse are colored the same.

Spiral Readouts for short echo time

From the SNR analysis, achieving a short echo time is extremely important. One way to reduce the echo time is to use k-space trajectories that sample the center of k-space first. The most commonly used trajectory in diffusion-weighted MR imaging is echo planar imaging (EPI) [77]. In this trajectory a raster scan of lines through k-space is performed starting with an edge of k-space and ending with the opposite edge. This EPI trajectory samples the center of k-space at the center of the readout, causing half the k-space needed to be sampled before the TE and preventing short TEs. The spiral trajectory provides a readout that is able to sample the center of k-space first and is a frequently used due to its ability to efficiently cover k-space by better leveraging gradient hardware limitations than the EPI trajectory. This is in contrast to commonly used EPI acquisitions which suffer from expanding echo times when the spatial resolution of the acquisition is increased.

EPI trajectories have the potential to incur large TE penalties, especially as the spatial resolution of the scan increases. However, some of this TE penalty can be reduced by using parallel imaging combined with a partial Fourier acquisition. The spiral trajectory is also extremely flexible in its design allowing an arbitrary number of shots to be designed to cover k-space in multiple acquisitions. This allows for fine control over the amount of undersampling per shot and the readout duration, to limit susceptibility distortions and T_2*-induced blurring. Long readouts are desirable as they will limit the total number of shots required to form an image; however, longer readouts come with increased magnetic susceptibility-induced distortion which must be addressed during image reconstruction.

Diffusion encoding for short echo time

In terms of minimizing TE, the pulsed gradient spin echo (PGSE) sequence [14] allows for the shortest diffusion encoding preparation time. However, being able to achieve a short echo time using PGSE encoding is dependent on the k-space trajectory being used. Center out k-space trajectories, such as spiral, are able to achieve the shortest echo times. The gain due to TE by switching to center-out k-space trajectories is not as large in the commonly used twice refocused spin echo (TRSE) EPI acquisition [15] that is frequently used on 3 T clinical hardware. By using center-out k-space trajectories with PGSE diffusion encoding, a reduction of 10-15 ms in TE could be expected on most clinical systems when compared to trajectories that do not sample the center of k-space early in the readout. The switch to PGSE has the potential to significantly increase artifacts due to eddy currents on some hardware, but recent processing tools, such as the 'eddy' tool in FSL [39], have been able to greatly reduce these concerns, especially in combination with advances in hardware [78] that reduce the impact of eddy currents.

Motion correction for multi-shot diffusion weighted imaging

At high resolutions, a multi-shot acquisition becomes necessary to limit the duration of the long data readouts to limit the T2* blurring and image distortions. In DWI, using multiple shots leads to motion-induced phase errors (MPE) due to different shots having differences in small amounts of motion during diffusion encoding [64]. These phase errors lead to artifacts and signal cancellations in the reconstructed image if not corrected, Figure 21. A wide variety of techniques have been developed to handle these errors [40, 41, 43, 44, 46, 47, 49, 63, 79]. In addition to subject motion during DWI, these phase errors can be caused by cardiac pulsation or other physiological motions, which may result in non-linear MPE. Being able to correct for MPE is important and will be discussed in more detail in Chapter 5. For a multi-slab sequence, a 2D navigator can be used to estimate the phase for a 3D slab assuming that the spatial variation of MPE in the slice direction is small, which has been shown to be accurate as long as the slabs are thin [73, 80].

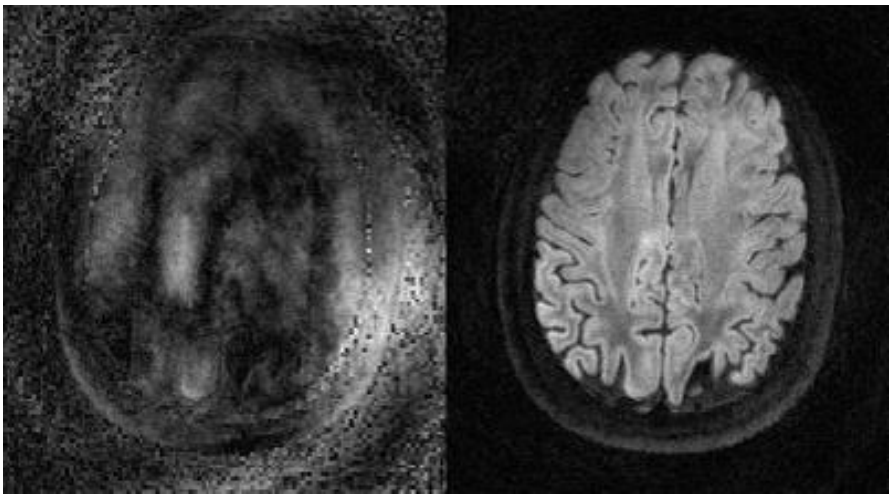

Figure 21: Multi-shot diffusion weighted image without any correction for MPE (left). Diffusion weighted image with motion correction used (right)

Proposed Pulse Sequence

The proposed acquisition sequence is designed to achieve a high SNR efficiency by operating at an optimal TR and minimal TE. The acquisition uses a standard PGSE [14] approach

for encoding diffusion due to its efficient diffusion encoding and a 3D multi-slab excitation approach due to its ability to balance sampling time for a slice with adequate T1 recovery. The use of spiral readouts also enable the short echo time provided by the PGSE scheme to be realized, enabling higher SNR by shortening the TE. The pulse sequence used to achieve this is shown in Figure 23. Additionally, a spectrally selective lipid excitation and spoiler gradient is used for lipid suppression (not shown), FID crusher gradients are used for low b-values, and gradient spoiling is used after the spiral readout.

A short spiral-in navigator is placed immediately after the second diffusion-encoding gradient followed by a kz phase encoding gradient and then a spiral readout for imaging data. For a PGSE sequence, this spiral-in navigator does not add any time to the imaging sequence as long as it is shorter than the slice select rewinder plus one half the excitation pulse duration minus the duration of the kz encode, Figure 22. The placement of the navigator directly before the imaging readout instead of after a second refocusing pulse is beneficial because it does not impact scan time efficiency. The amount of time is available will depend on the duration of the RF pulse and the thickness of the slab, which will change the slice rewinder gradient. For the cases used in this work, this was typically between 8 and 10 ms of available time for a navigator. In the available time, a spiral navigator with a 40x40 matrix size acquired with a parallel imaging factor R=2 was acquired in this work.

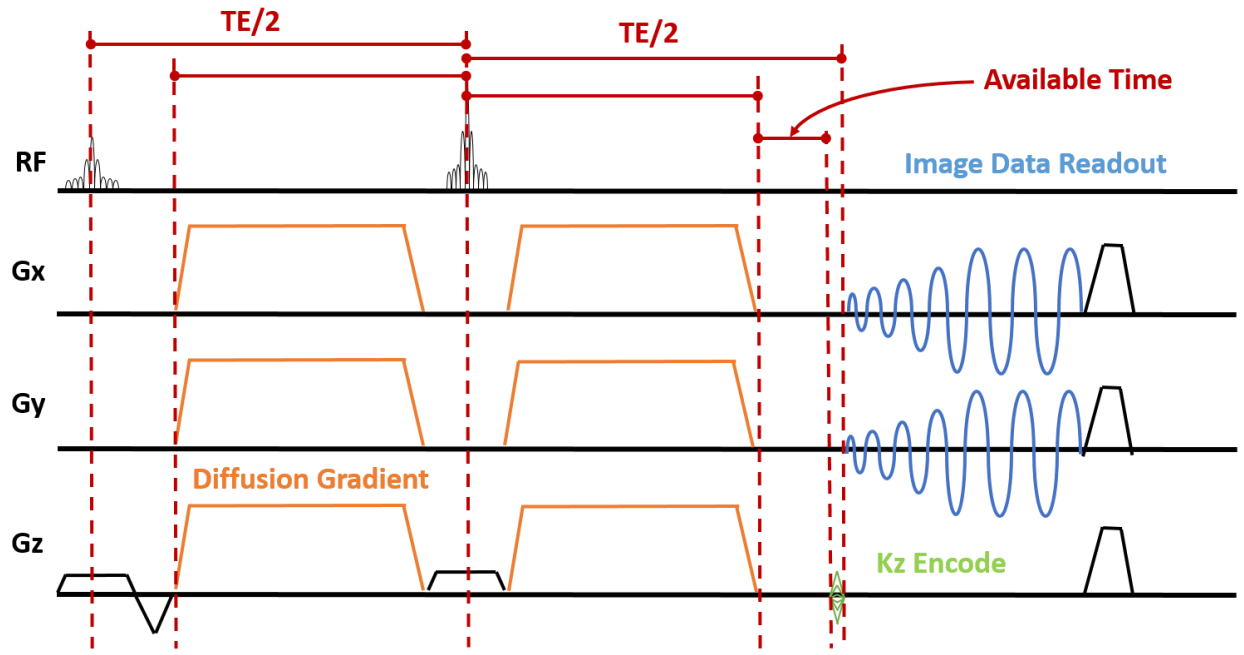

Figure 22: Timing of spiral PGSE spiral sequence showing available time for a navigator.

In order to minimize artifacts associated with imperfections in 3D slab excitation several considerations were made. First, relatively long (10 ms) RF pulses were designed using the SLR procedure [81] to result in sharp transition widths. Additionally, the number of slices in a slab was kept low in order to decrease the amount of signal loss that can sometimes be observed at edge slices. The slabs were also excited in an interleaved manner to reduce interactions between adjacent slabs. Finally, a TR is used that is slightly longer than the T1-optimal TR to enable further relaxation between adjacent slabs. Combining all these pieces enabled the use of the pulse sequence in Figure 23 to be used.

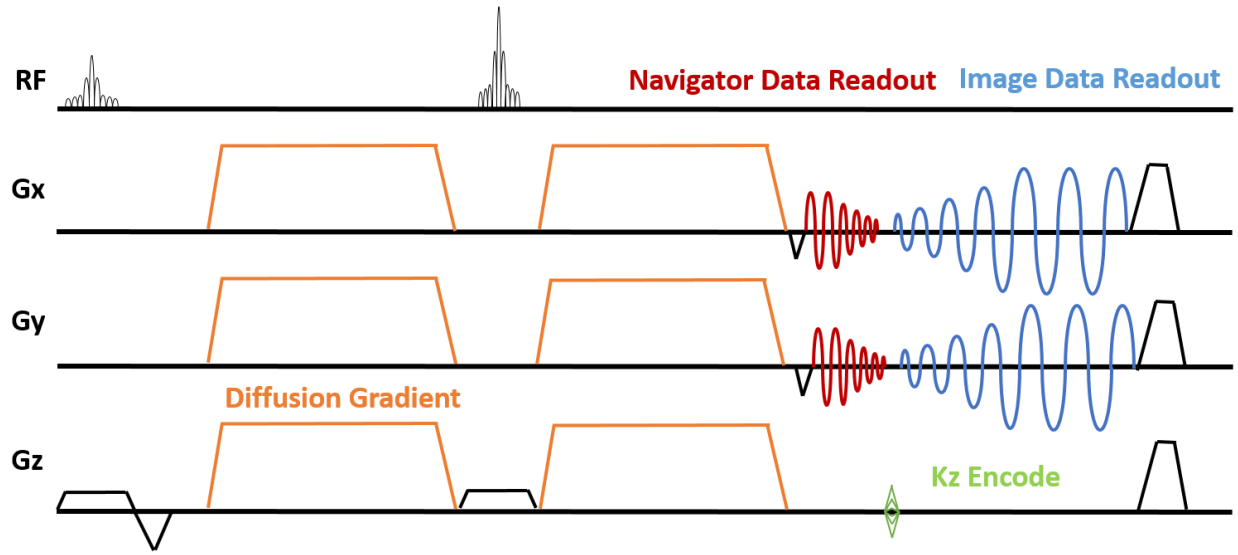

Figure 23: Multi-slab multi-shot spiral diffusion image pulse sequence

Image Reconstruction

An iterative, model-based image reconstruction scheme is used to allow modeling of non-Cartesian spiral readouts, non-linear MPE [41], parallel imaging using SENSE [4], and correction for magnetic susceptibility-induced image distortions [5]. The magnetic field inhomogeneity correction enables the use of longer readouts, reducing the total number of shots, with their diffusion encoding overhead, leading to a higher SNR efficiency [82].

In Vivo Results

A number of data sets were acquired in order to assess the ability of the proposed sequence to achieve improved SNR and determine if higher SNR values can be achieved. The parameters for the acquisitions are outlined in Table 2. All data were collected on Siemens 3 T Trio scanner using a 32-channel head coil. Scanning was done under local IRB approval with all subjects giving written consent before participating.

Table 2: Sequence Parameters

Name	Sequence	TE (ms)	TR (s)	Total scan time (s)	Resolution/ Matrix Size/ Coverage	Total Shots per Image	Readout Duration (ms)	Number of Images/ Diffusion Encoding
2D_epi	TRSE EPI (GRAPPA R=3)	92	9.60	480	2 mm isotropic 120x120 60 slices	1	27	25 (b =0) 25 (b = 1000)
2D_spiral	PGSE (spiral R=3)	73	7.26	363	2 mm isotropic 120x120 60 slices	1	20	25 (b =0) 25 (b = 1000)
3D_spiral	PGSE (spiral R=3)	81	1.97	394	2 mm isotropic 120x120x4 15 slabs 4 slices/slab	4	20	25 (b =0) 25 (b = 1000)
3D_spiral_HR1e	PGSE (spiral R=3)	83	3.10	396	1.25 mm isotropic 192x192x4 24 slabs 4 slices/slab	12	29	2 (b =0) 30 directions (b = 1000)
3D_spiral_HR2	PGSE (spiral R=2)	80	2.00	5,120	0.8 mm isotropic 300x300x20 1 slabs 20 slices/slab	80	52	2 (b =0) 30 direction (b = 1000)
2D_epi_DTI	TRSE EPI (GRAPPA R=2)	95	2.00	64	2 mm isotropic 120x120 8 slices	1	41	2 (b =0) 30 directions (b = 1000)

SNR Results

To compare the SNR achievable with the optimized, 3D multi-slab sequence, several datasets using EPI and spiral with a variety of imaging parameters were obtained, see Table 2 for a description of the parameters of these acquisitions. First, a standard spatial resolution of 2 mm isotropic was targeted, collecting DWI data with a 2D acquisition with both single-shot EPI (referred to as '2D_epi') and spiral readouts (referred to as '2D_spiral'). The 2D_epi acquisition was chosen as a basis of comparison as it is the most commonly used acquisition on clinical MRI scanners at 2 mm spatial resolution. The proposed 3D multi-slab acquisition with 2 mm isotropic resolution (referred to as '3D_spiral') was acquired with a single in-plane shot for each kz

encoding in order to match readout duration for single shot imaging with the 2D_spiral protocol. For all of these acquisitions, the same FOV and slice coverage were used with the minimum TE and TR possible for each technique. Notably these acquisitions all require the exact same number of excitations to do the imaging as all are single-shot in a kz plane or single-shot within a 2D slice. A high resolution T1-weighted MPRAGE (TE: 2.3 ms, TR: 1900 ms, TI: 900ms, FOV: 230x172x230 mm, matrix 256x192x256) was acquired. Additionally, reference images with different echo times were acquired for field map estimation [83] to enable field inhomogeneity correction [5] and to estimate the coil sensitivity map [4]. This scan used an asymmetric spin echo, spin echo TE of 17 ms, gradient echo TE was 1 ms delayed, matrix size: 120x120, FOV: 240x240 mm, slices: 40 , slice thickness: 3 mm ,TR: 1800ms.

Table 3 provides the parameters related to the SNR efficiency for each acquisition protocol along with the theoretical relative SNR efficiency from those protocols, compared to the parameters used in the 2D EPI acquisition. The "SNR ratio from TR" is the theoretical change in signal due to changing TR using a standard spin echo recovery equation, assuming the sequences have the same readout and TE. The "SNR ratio from TE" is the amount of signal gained by reducing the TE due to a spiral trajectory assuming the TR and readout are the same between sequences.

Table 3: Theoretical SNR efficiency for Multi-slab Acquisition

Name	TE (ms)	TR (s)	Total ADC Time (ms)	SNR ratio from TR	SNR ratio from TE	SNR ratio for single image	SNR efficiency ratio
2D_epi	92	9.60	16.8	-	-	-	-
2D_spiral	73	7.26	20.0	0.99	1.32	1.44	1.65
3D_spiral	81	1.97	80.0	0.83	1.71	2.11	2.33

SNR measurements were derived by taking the temporal mean divided by the temporal standard deviation from 25 repeats of each measurement for a single diffusion encoding direction. A white matter mask was obtained in the subject's DTI space by segmenting the MPRAGE image

using FAST [84] in FSL (http://fsl.fmrib.ox.ac.uk) and then registering the segmentations to the diffusion weighted images using FLIRT [85, 86]. The pixel-wise SNR was then averaged across the mask to create a single image SNR value for each of the acquisitions: 2D_EPI, 2D_spiral, 3D_spiral. SNR efficiency was calculated by taking the SNR in the image and dividing it by the square root of scan time required to acquire the image.

Table 4: Measured SNR values for Multi-slab Acquisition

	2D_epi (b = 1000)	2D_spiral (b = 1000)	3D_spiral (b = 1000)
S1	7.0	9.6	10.6
S2	7.5	9.8	11.3
S3	7.5	10.1	11.6
S4	8.2	11.0	12.8
S5	7.5	9.7	11.5
Average (+- Std)	7.5 (0.4)	10.0 (0.6)	11.6 (0.8)
SNR ratio from 2D_epi	-	1.33	1.55
SNR efficiency ratio from 2D_epi	-	1.53	1.71

Table 4 summarizes the SNR measurements from 5 subjects across the 2D_epi, 2D_spiral, and 3D_spiral acquisitions that all had 2 mm isotropic resolution. The SNR ratio from 2D_epi is the ratio of SNR obtained in each of the three methods, divided by the SNR measure from the 2D_epi acquisition. The SNR efficiency ratio was calculated by dividing the SNR by the square root of the acquisition time, and then normalizing to the 2D_epi value. Table 4 also gives the estimated SNR efficiency increase of 53% from the shorter TE and TR associated with spiral by comparing the 2D_epi with the 2D_spiral acquisitions. It also gives the estimated SNR efficiency increase of 71% for the 3D encoding and spiral acquisition over the 2D EPI, by taking into account the shorter overall imaging time. Figure 24 shows a comparison of the reconstruction of a single slice for the 3 different acquisitions used for the SNR analysis.

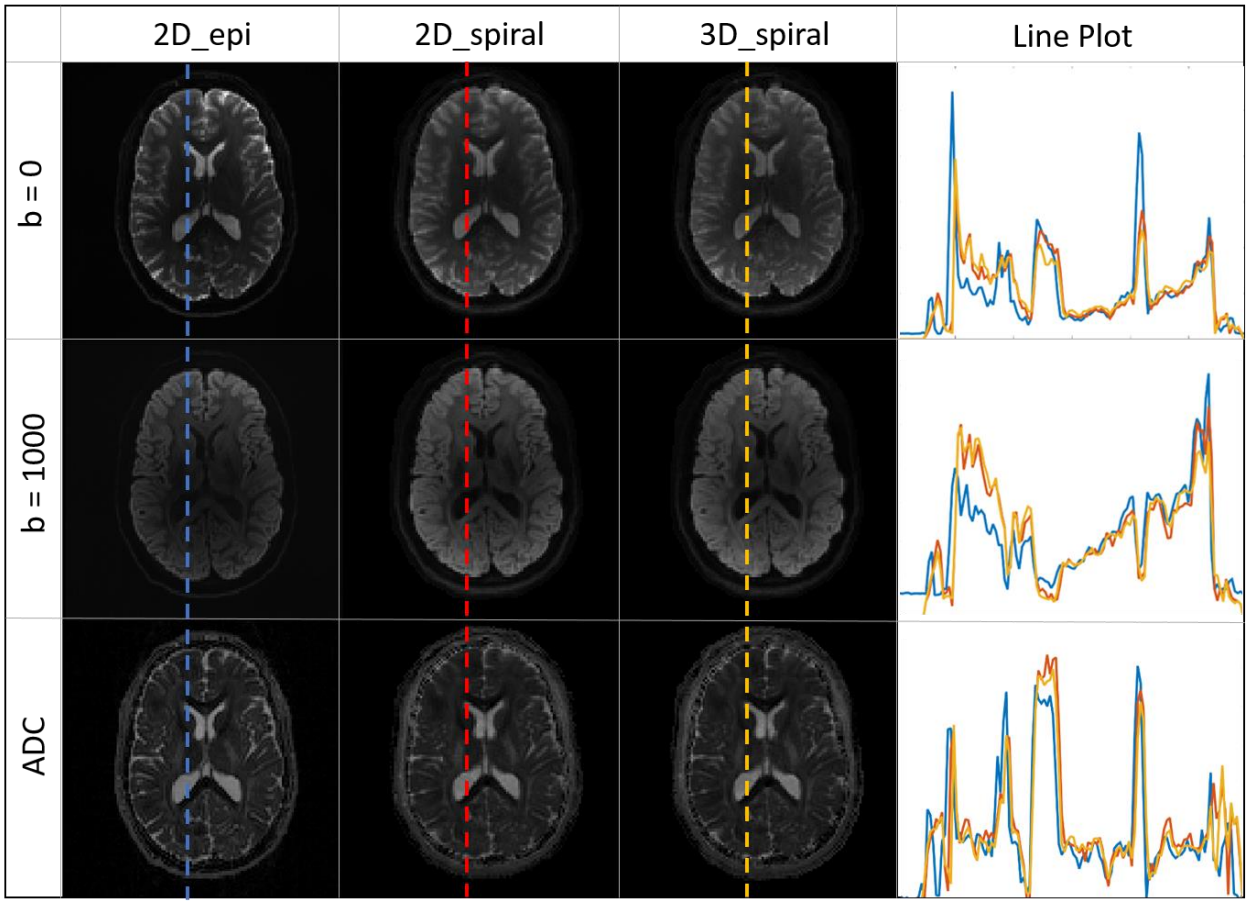

Figure 24: Image Reconstruction comparison between EPI, spiral, and multilsab spiral acquisitions.

The use of a 3D multi-slab spiral acquisition provided SNR efficiency gains over the commonly used 2D EPI acquisition for the same coverage and without increasing scan time. The 2D spiral acquisition showed a 53% increase in SNR efficiency over the 2D EPI acquisition. This is in similar to the expected theoretical gain of 65%. For the 3D spiral acquisition, a 71% increase in SNR efficiency was achieved over the 2D EPI acquisition. Theoretically a gain of 133% was expected, significantly higher than the measured gain in SNR efficiency. Differences in SNR for this comparison could be due to decreases in signal at the edge of slabs in the 3D excitation or from incomplete motion induced phase error correction as the 3D acquisition uses multiple shots across kz to acquire an imaging volume.

DTI Images

To demonstrate that the proposed sequence can be used at higher resolutions, a 1.25 mm isotropic (3D_spiral_HR1) and 0.8 mm isotropic DWI datasets (3D_spiral_HR2) were acquired with the proposed sequence. A matched coverage 2 mm resolution data set (2d_epi_DTI) was acquired to compare 0.8mm to 2 mm resolution. Fractional Anisotropy (FA) images were created using DTIFit [87] in FSL. These data acquired 30 different diffusion directions for estimating a diffusion tensor in order to match what is most commonly done at lower resolutions. However, depending on the diffusion model being used it may be possible that other diffusion schemes may be better for estimating a tensor [88].

The ability of the proposed method to acquire multiple direction diffusion data at higher spatial resolution (1.25 mm isotropic) in a reasonable time (19.8 min for 30 direction DTI data) is demonstrated in Figure 25 using the 3D_spiral_HR1 data set.

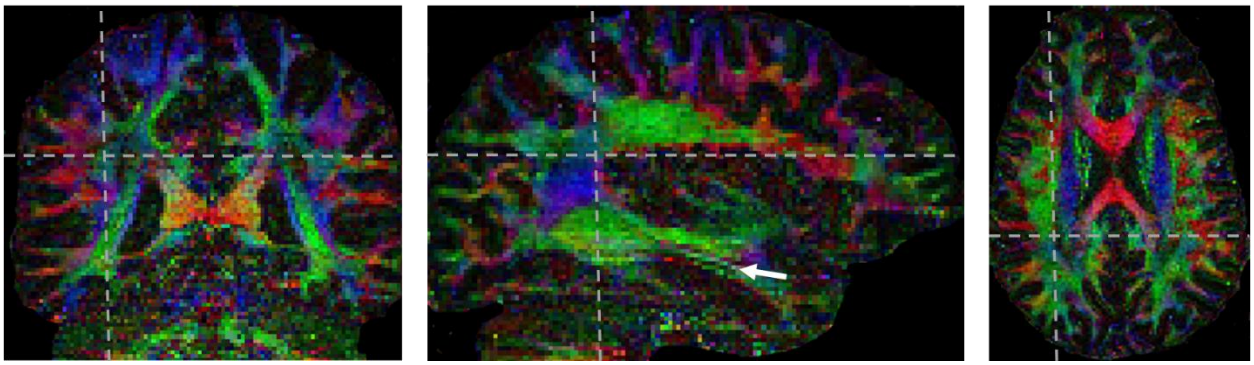

Figure 25: Fractional anisotropy images from a 1.25 mm resolution 30 direction DWI data set. Fine structures, such as parts of the hippocampus (arrow) are more easily delineated at higher resolutions.

To demonstrate the scalability to higher resolutions, the 3D multi-slab sequence was used to acquire a 30-direction data set at a 0.8 mm isotropic resolution (3D_spiral_HR2). Figure 26 shows the color-coded FA from the 0.8 mm isotropic acquisition. At this increased resolution, partial volume effects of fine white matter structures are greatly reduced.

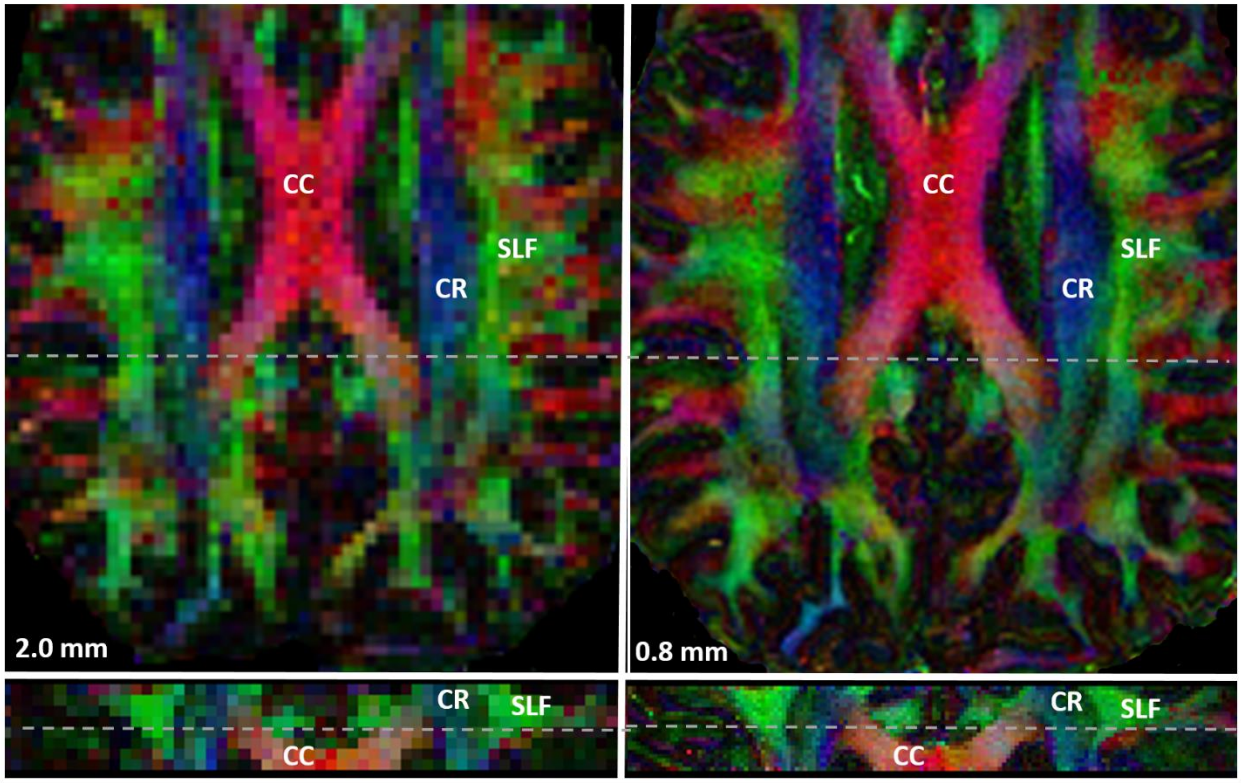

Figure 26: Comparison of fractional anisotropy images from 2.0 mm isotropic resolution (left) and 0.8 isotropic resolution (right).

In order to achieve a short total acquisition time and maintain a high acquisition efficiency, the collection of longer data readouts per diffusion encoding is desired. As previously stated, this results in a tradeoff with magnetic field inhomogeneity induced image distortion. Figure 27 demonstrates the image reconstruction results for a single slice in a 3D slab with and without field correction from the 3D_spiral_HR2 acquisition along with type of distortion observed when no motion correction is used. The spiral readout for this imaging data had a relatively long duration of 52 ms. The long data readout results in significant susceptibility-induced distortions in the image, which are radial blurs for spiral acquisitions. Using the magnetic field inhomogeneity corrected image reconstruction, a high-quality image was recovered from the data.

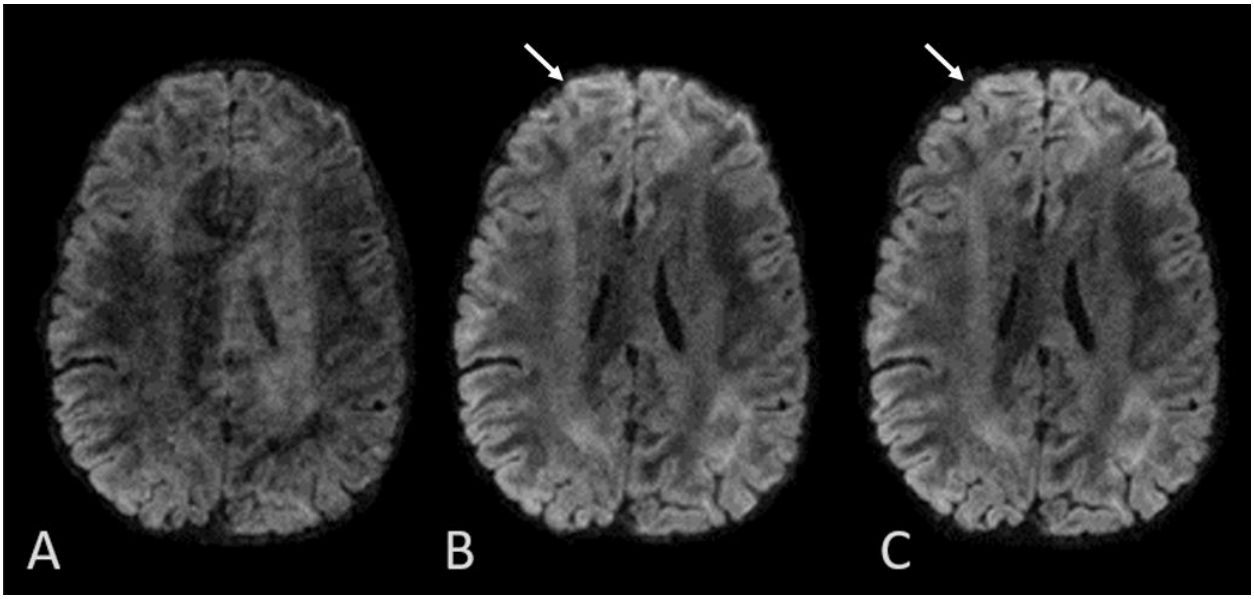

Figure 27: A single slice of a diffusion weighted image at 0.8mm isotropic resolution reconstruction in 3 ways: with no field or motion correct (A), with no field correction (B), with both field and motion correction (C). The arrow denotes the frontal area of the brain that was strongly impacted by the field correction.

Conclusion

This study demonstrated the feasibility of a multi-slab 3D spiral diffusion acquisition to achieve high-resolution DWI (sub-mm isotropic) on a clinical 3 T MRI scanner. The proposed sequence can achieve higher SNR than a standard 2D EPI acquisition with whole brain coverage at the same spatial resolution and same scan time. The gains in SNR come from using spiral readouts to shorten TE and from the SNR-optimized TR combined with a 3D multi-slab acquisition approach. While the spiral readout was chosen for this study, other center out k-space trajectories could also achieve SNR gains due to shorter echo times which are uncoupled from increases in spatial resolution. Additionally by using an iterative, model-based reconstruction scheme, a flexible approach was created capable of using non-Cartesian k-space trajectories, k-space under sampling, and correction for distortions due to long data readouts.

The navigator acquired with the proposed acquisition provided sufficient information to correct for non-linear motion induced phase errors. Additionally, the location of the navigator

allowed for shorter scan times as a second refocusing pulse for a separate navigator was not required.

The technique was successfully applied to achieve much higher resolutions than what are commonly acquired with whole brain coverage on clinical 3 T MRI scanners. The ability to achieve sub-mm isotropic resolutions (sub μL voxel volume) provides great promise for the field of diffusion neuroimaging. At this resolution partial volume effects are greatly reduced allowing for much better distinctions between fine white and grey matter structures, along with more accurate measures of diffusion properties in these fine structures.

Combining motion-induced phase measurement and correction, 3D multi-slab acquisitions, and magnetic field inhomogeneity correction, an acquisition approach was proposed and validated demonstrating significant gains in SNR efficiency over standard approaches. The proposed approach provides a promising technique to study fine white matter fiber structures in complex geometries, reducing partial volume effects.

Chapter 4: Spiral multi-band Diffusion Weighted Imaging

In chapter 3 a method based on multi-shot, multi-slab spiral readouts for high SNR efficiency was presented. In this section, several modifications to the pulse sequence will be demonstrated that enable higher acceleration factors and minimize the appearance of slice banding artifacts.

In the multi-slab sequence, a group of adjacent slices are simultaneously excited as a 3D slab of contiguous slices. By exciting multiple slices at the same time the total number of excitations required to image the entire volume of the brain is reduced. As previously discussed this now allows more fine control over the TR and can lead to an increase in SNR efficiency. An alternative approach to exciting multiple contiguous slices is to excite slices that are distributed throughout image space, Figure 28. This approach was popularized for recent applications in both fMRI and DTI [89-91].

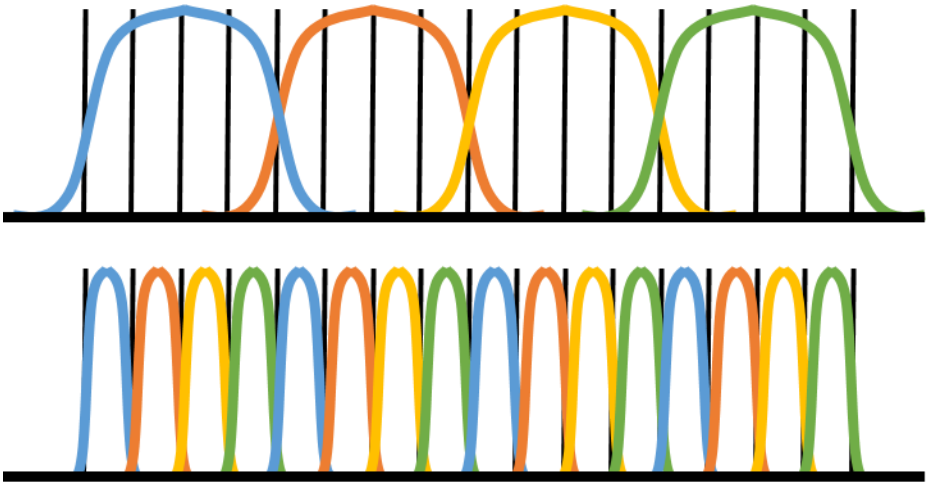

Figure 28 Multi-slab excitation (top) and multi-band excitation (bottom with the black lines representing the different slices and the area under the same color curves being excited at the same time

Multi-band RF pulses

In MR, RF pulses are typically designed to excite frequencies within a specific bandwidth. For small flip angles the excitation profile can be estimated by taking the Fourier transform of the

time domain RF pulse profile. If the time domain signal had an infinite sinc shape the excited frequency would be an ideal rect function and only excite spins within the designed frequency range. However, an infinite time sinc pulse is not possible so the pulse is truncated in time. The truncation results in a non-ideal rectangular shape giving rise to variations in slice profile with frequency.

One of the great features of the excitation in MR is that it is based on a linear system relating the slice profile to the Fourier transform of the RF pulse. The concept of linearity allows two RF pulses that excite different ranges of frequencies to be added together in the time domain and result in the excitation of the two different bandwidths in the frequency domain. Using this concept an RF pulse can be designed that excites multiple frequency bandwidths simultaneously, allowing for the excitation of multiple slices.

While the addition of the RF pulses in the time domain can be used to create a simple RF pulse that excites multiple slices, this approach suffers in practice with issues with RF power. Because the 2 pulses are added in the time domain the peaks of the pulses are typically added together and result in a larger peak RF power being necessary to excite the multiple slices. An elegant solution that can be used to minimize the RF power issue is to phase the RF pulses in the time domain before adding them together [92]. Wong proposed a minimization problem that minimizes the peak RF power given different number of slices. This method results in slices that each have a different phase offset when excited, however this is easily accommodated for most applications and results in a dramatic decrease in peak RF power.

Slice Banding Artifacts

In the proposed multi-band sequence, an RF pulse was designed using the SLR algorithm to create sharp slice profile. While the SLR design criteria allows for fine control over the passband ripple, rejection band ripple, and transition width, a perfectly rectangular profile is not able to be

achieved. The excitation profile is improved by using a higher bandwidth pulse, however that typically increases the peak RF power, causing limitations on how high of a bandwidth can be used. The imperfection in slice profile results in different slices being excited to different extents within an excitation band. For example, slice in the transition band of the RF pulse will not be excited to the same level as one in the middle of the passband, which can result in visible slice profile variability in the reconstructed images. One approach to minimizing this is to excite a larger region and discard extra slices in the transition region. However, this approach has two issues associated with it: The first issue is that by acquiring more slices than are needed, more sampling time is needed to fully sample the images, this will increase the total scan time. The second issue is that by exciting slices outside of the desired volume, the signal recovery time for the slices in the discarded region is different as the slices will also be excited by another RF pulse that is imaging these adjacent slices with the adjacent slab. Another issue that arises when exciting a band of slices is that the profile effect appears worse when a large number of slices in a slab is acquired due to a larger number of slices falling in the transition band of the RF pulse. An example of the type of slice banding that can be seen in multi-slab acquisitions can be seen in Figure 29

Figure 29: A sagittal (left) and coronal (right) view of a diffusion weighted image showing the slice profile effect in multi-slab imaging.

The variation in signal amplitude across the slices can result in decreased SNR in slices in the transition band region. However, in diffusion imaging where quantitative measures are made in reference to other images with the same slice profile artifacts, the decrease signal amplitude does not impact the estimation of parameters except for the slightly lower SNR. This is true as long as all the images in the time series used in the analysis have the same slice profile effects.

By exciting distributed slices together, the multi-band excitation provides a way to make the slice profile effects less visible. In standard single slice excitation, there is variation in the slice direction in signal intensity. However, the variation in intensity is not visible as only a single slice is resolved. In multi-band imaging the same RF pulses that are used in single slice imaging are used, allowing multi-band pulses to have similar slice profiles to the commonly observed single slice, 2D sequences.

Higher acceleration Factors

The other main benefit of multi-band excitation is the opportunities it offers for parallel imaging. In multi-slab and single slice imaging, the field of view for a single image in the slice dimension is small. For example, if a volume of 120 mm in the slice direction was imaged with 2 mm slices, the single slice excitation would have a FOV of 2 mm in the slice direction, the multi-slab approach would have a FOV of 8mm if 15 slabs were excited, while the multi-band sequence would have a FOV of 120 mm in the slice direction. This much larger field of view in the slice direction provides opportunities for higher acceleration factors on newer receiver coils with many elements in the slice direction. Instead of only using parallel imaging in the in-plane direction, comparable acceleration factors can be used in the slice direction when a larger FOV is used in the slice direction.

Sequence Design

The pulse sequence in Figure 23 can be modified slightly to provide a multi-band excitation. First the SLR pulses designed for extremely short transition widths in the multi-slab sequence are replaced with standard pulses used for single slice excitation and them modified for lower peak power for multi-band excitation [92]. The pulse duration for the RF pulses will depend on the RF power the scanner is capable of as well as the shape of the base RF pulse that is being combined. In this work RF pulses with durations of 10 ms were used for the multi-band case. In the multi-band case the 10 ms duration pulses did not have any issues with exceeding the peak RF power for any of the number of the bands tested, up to 12 bands. For smaller number of bands being excited a shorter RF pulse is able to be used with a 5 ms RF pulse being used for exciting 4 bands.

The other major modification to the sequence is the navigator for motion correction. In the multi-slab imaging case there was a small FOV in the slice direction, so the MPE could be approximated using a 2D phase profile. In the multi-band case the FOV in the slice direction is much larger and the 2D approximation is not adequate to represent phase variations in the slice direction. Therefore, a 3D navigator is now needed to accurately model the phase of the MPE, which needs to be accomplished in a single shot. To acquire a single shot navigator the blipped spiral trajectory was used [93]. The blipped spiral trajectory can be seen in Figure 30. The trajectory has a spiral shape in the in-plane direction and then changes the plane of kz sampling throughout the excitation. This trajectory has the benefit over 3D single shot trajectories such as echo volume imaging, in that the echo time can be at the start or end of the trajectory, depending on if a spiral-in or spiral-out design is used. This allows this trajectory to synergize well with the proposed sequence as it allows the echo time between the image data and navigator data to be the very close. However, due to the limited amount of available time to play out the navigator without

adding time to the sequence, a lower in-plane resolution than what was used in the multi-band case, 40, is typically acquired to avoid increasing the TE.

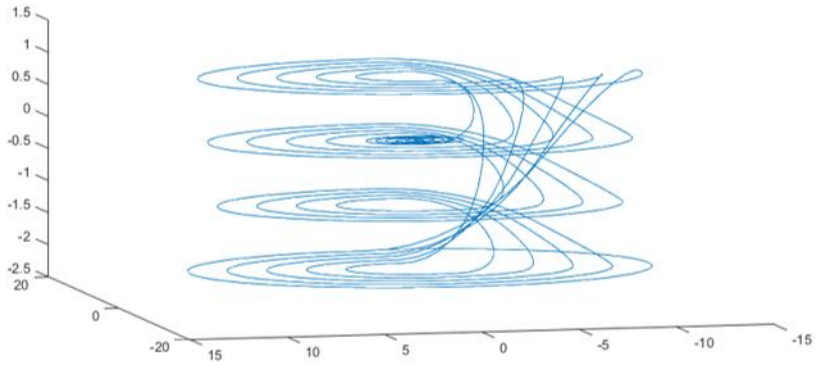

Figure 30: Single shot blipped spiral trajectory for navigation

For the imaging data, a stack of spirals 3D trajectory can still be used. However, the design of the encoding in the slice direction is modified as the FOV in the slice direction is now much larger. This allows for the possibility of acceleration factors in the slice direction to be used. An example of a trajectory that is better for accelerating in the slice direction is the rotated stack of spirals trajectory [93].

Applying the modifications results in the proposed acquisition in Figure 32. This sequence closely resembles the multi-band approach but allows for higher slice acceleration and reduced slice profile artifacts. This sequence retains the placement of the navigator before the imaging data, this has the benefit of not needing a second refocusing pulse to acquire a separate navigator that other multi-band and multi-slab acquisitions are using. This allows for more excitations in the same amount of time to be made, giving more flexibility in setting up sequence parameters.

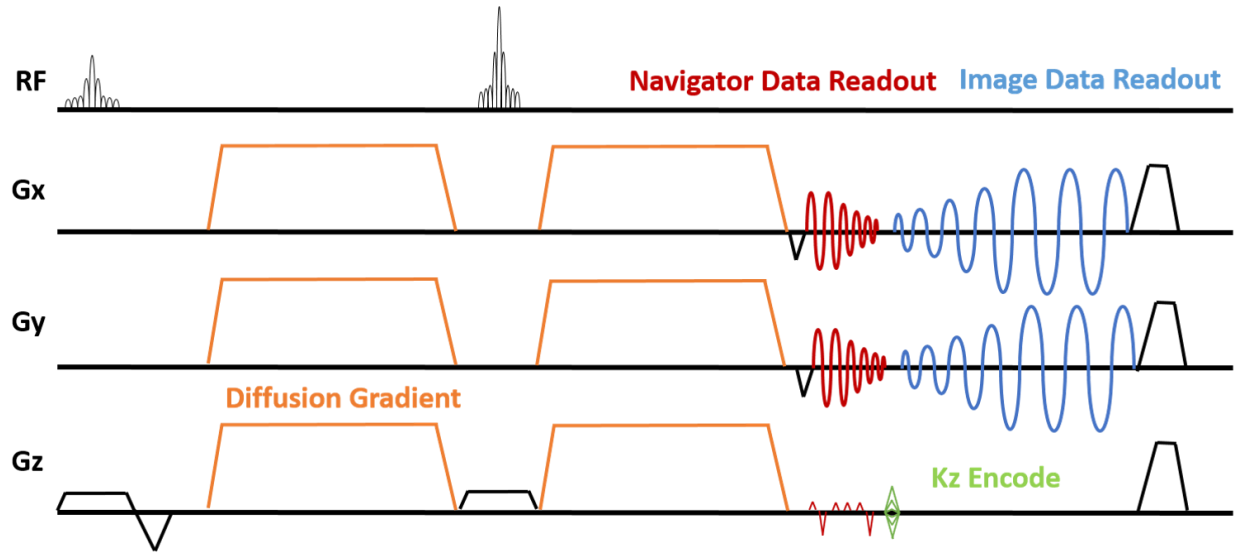

Figure 31: Proposed pulse sequence for multi-band diffusion weighted imaging

In Vivo Results

The proposed pulse sequence in Figure 31 was tested in vivo on a Siemens trio scanner. Image reconstruction was the same as in chapter 3 with a coil sensitivity map and field map being acquired separately in order to perform SENSE and field correction. The key difference in the reconstruction is that the navigator is now 3D, varying with the slice position.

First, to demonstrate that the pulse sequence can acquire standard resolutions at high speeds and with high quality images a data set at 2 mm isotropic resolution with a FOV of 240 mm in-plane and 4 slices acquired. The sequence achieved a TE of 88ms and a TR of 2.1 seconds. This sequence used 4 shots per image in order to match the number of excitations that would have been needed if this was done with standard 2D imaging. The resulting images along with FA maps can be seen in Figure 32.

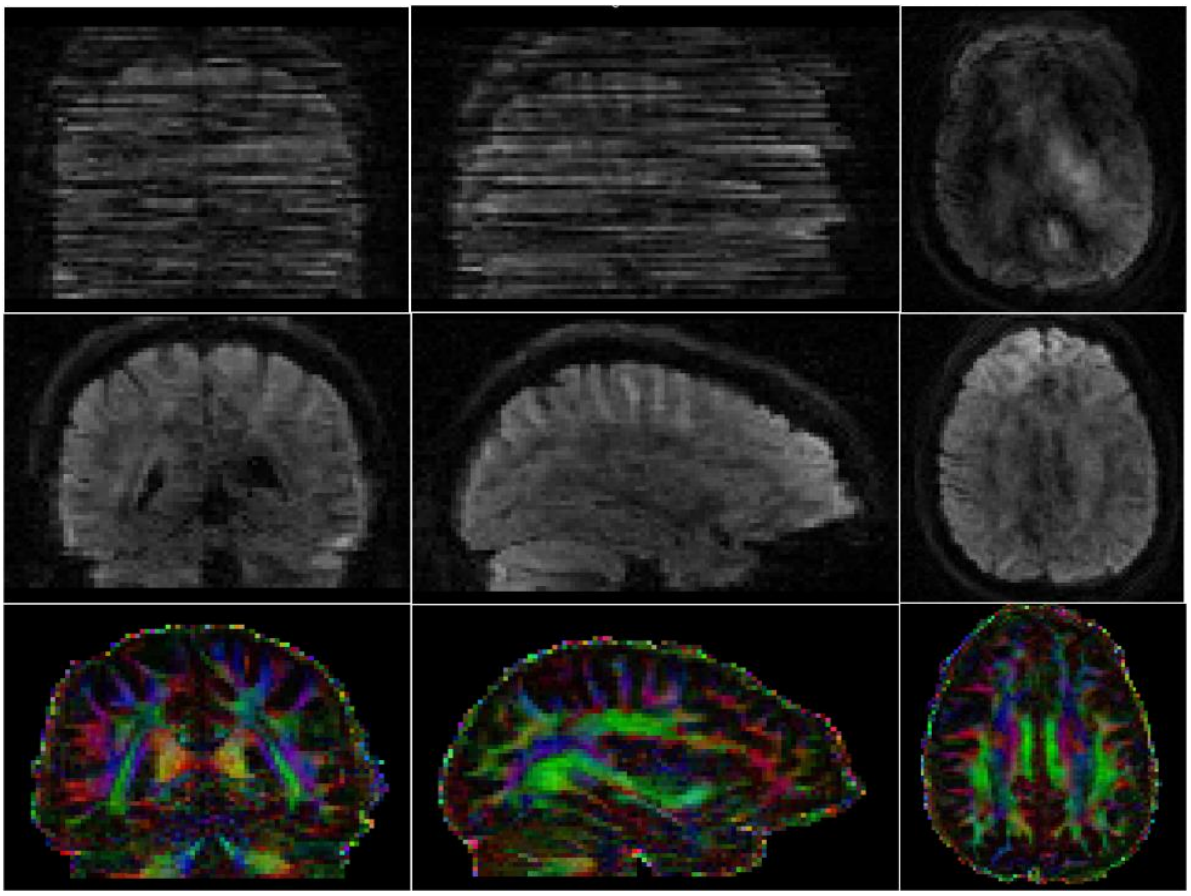

Figure 32: 2mm Diffusion weighted images form a multi-band acquisition. The top row shows a case where no motion correction is used. The middle row gives an example of a diffusion weighted image with MPE correction. The bottom row displays a color-coded FA map

The 2 mm results demonstrate that quality images with adequate SNR can be acquired in 4.5 minutes. The images do not contain a slab profile artifact that is present in the multi-slab images.

To further test the multi-band approach a data set with a 1.25 mm resolution was acquired. To achieve 1.25 resolution with a FOV of 240 mm a 24-shot stack-of-spirals trajectory with 90 slices and 6-band excitation was used. The resulting sequence used a TR of 2.2 seconds and a TE of 92 ms and acquired 30 diffusion weighted images with a b-value of 1000 s/mm^2 and 2 images without diffusion weighting in 28.2 minutes. A resulting diffusion weighted image and an FA

image can be seen in Figure 33. The images once again appear to have adequate SNR, even at this higher resolution.

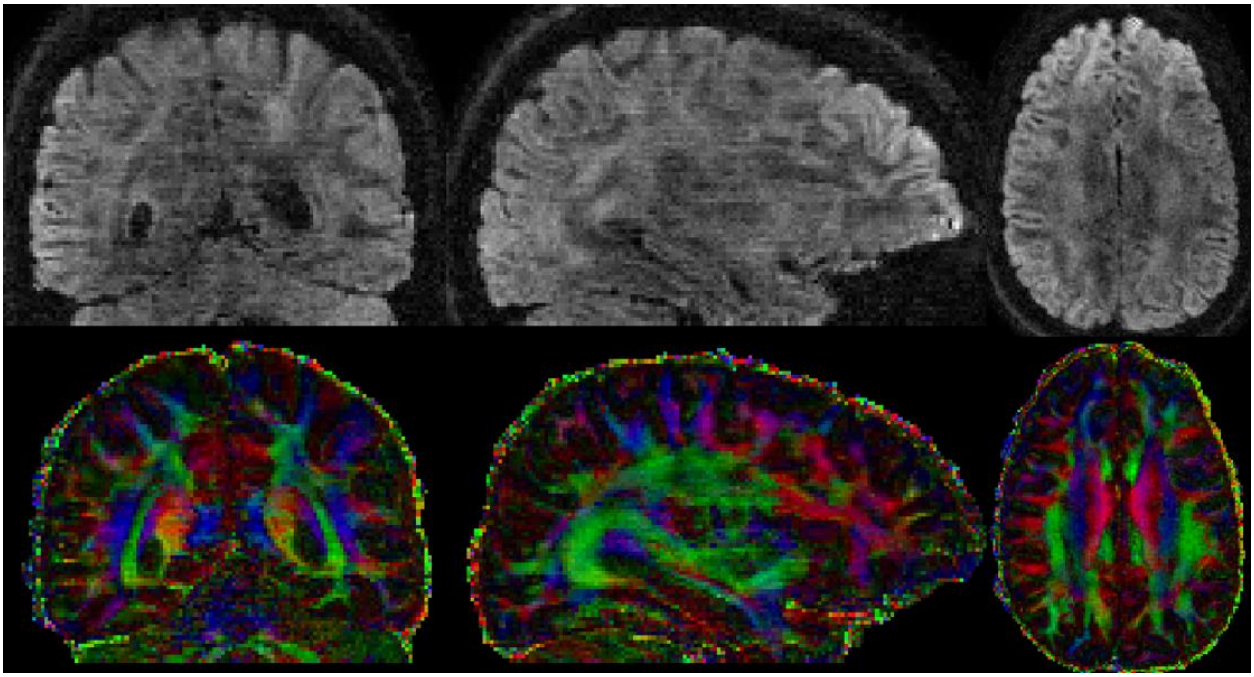

Figure 33: 1.25 mm multi-band diffusion imaging

Practical Considerations

The multi-band sequence provided excellent imaging results allowing for the potential for higher acceleration factors and decreased slice profile effects. In practice several considerations need to be made when implementing a multi-band multi-shot diffusion imaging acquisition.

Correcting MIP in multi-band

Due to the 3D MPE correction that is needed in multi-band acquisitions, the navigator now needs to be sampled in 3D as previously explained. With the blipped spiral-in navigator this works well for low resolutions and a low number of bands. However, when many bands or higher in-plane resolution is needed the navigator readout becomes much longer, which can negatively impact the echo time. This navigator sampling issue can begin to be seen in Figure 33 as there is more noise that starts to appear in the center of the image. Due to this limitation the sequence becomes less practical when a long navigator readout is required. In cases where a long navigator

readout is needed a modified version of Figure 31 may be needed where the navigator is placed after a second refocusing pulse. In chapter 5 the navigator readout will be discussed in more detail to help determine what sampling can be used.

SNR and acceleration factor

The multi-band pulse sequence allows for much higher acceleration factors to be used in the slice direction, allowing for overall higher acceleration factors to be used and still get images without aliasing artifacts. However, in diffusion imaging one of the major challenges is SNR. Just because it is possible to reconstruct images using higher acceleration factors, it is frequently not practical to do that at higher resolutions as the leading factor in image quality is the SNR. In these cases the improvement in slice profile can still be observed, but the acceleration factor may not be large due to the need to scan longer just to get adequate SNR.

This is evident in the 1.25 mm dataset in Figure 33 as the voxel volume is ¼ the volume as the 2 mm dataset in Figure 32. The 2 mm dataset took 4.5 minutes to acquire while the 1.25 mm dataset took 28.2 minutes to acquire. The change in voxel size did not allow for high acceleration factors to be used to shorten the acquisition. Additionally, the higher number of bands used a slightly longer navigator, this caused an increase in TE, further reducing the SNR of the higher resolution acquisition. The issue of the navigator duration will be discussed in more detail in the following chapter.

Conclusions

The multi-band image acquisition with nonlinear phase correction provides an approach to acquire high resolution diffusion weighted images without the slab boundary artifacts associated with multi-slab imaging. Additionally the multi-band approach allows the potential for use of higher acceleration factors to be used. While using higher acceleration factors was not practical on the system used in this study due to SNR limitations, higher acceleration factors could be used

in applications where the base SNR is higher such as in lower b-values and magnetic resonance elastography. Systems with improved hardware that allow for a shorter TE may also be able to acceleration factors, as they will have more SNR from the shorter TE, making using higher acceleration factors more practical.

Chapter 5: Correcting Motion Artifacts in Diffusion Weighted imaging

We have discussed the issue of multiple shots having different phase due to coherent motion, leading to artifacts in estimated images. In this chapter, we discuss the appearance of the phase errors as well as the requirements to correct for the phase errors. The goal of this section is to lay out criteria that will be useful when designing a diffusion weighted imaging acquisition such as those presented in chapters 3 and 4. This is important as the spiral-based PGSE acquisitions has a small amount of available time that can be used for motion navigation without causing any increase in TE, as was shown in Figure 22. By making a navigator as compact as possible, it may be possible to not add any time to the acquisition or only to slightly increase TE. In this section, the sampling required for successful correction of MPE in image space will be investigated as it is the most commonly used approach to correcting for MPE in multi-shot diffusion imaging.

How to estimate motion induced phase

The most common way to estimate the motion induced phase errors (MPE or P in Equation 6) is generally to acquire a separate echo that fully samples a part of k-space. Typically this navigator data samples low resolution information as the phase information is assumed to be low resolution, this assumption will be discussed in more detail.

The other most common way to estimate the MPE is to use a self-navigated sequence. This self-navigated approach is commonly employed by variable density spiral acquisitions and PROPELLER trajectories [48, 60, 94]. The self-navigated trajectories eliminate the need to sample a second set of k-space or another echo, which often requires a second refocusing pulse in the sequence, which costs time in the sequence. Another benefit of the self-navigated trajectory is that the MPE is assured to be matched with the imagining data. The drawback of self-navigation is that the trajectories are less efficient and more excitations are typically needed to sample the full k-space for the diffusion weighted image.

Another approach that has recently been proposed is a navigator free method [43, 44]. In this formulation the phase map for each shot is not explicitly estimated. Instead the phase is estimated directly from the imaging data, similar to self-navigation but without the higher sampling requirements of the self-navigated navigator phase images. By using a combination of coil sensitivities and additional constraints on the reconstruction process. This approach has been found to be practical when images with a small number of shots are used and, hence, the parallel imaging and constrained reconstruction can recover full images from the individual shots.

Despite the differences in the way that the phase information is collected, all the methods share certain assumptions about the underlying properties of the phase. In the following sections, the appearance of the phase errors will be demonstrated in order to guide the design of multi-shot diffusion weighted imaging acquisitions.

Appearance of phase errors

One key aspect of the motion correction techniques discussed above is that a low-resolution navigator is used, due to the common assumption that the motion induced phase errors have low spatial resolution features. While this is generally accepted to be true in the field of diffusion weighted imaging, what resolution is "low" resolution is unclear. Figure 34 gives an example of the impact of spatial resolution of on the appearance of the MPE, showing that if not properly sampled, the estimate of the MPE will not be correct. The resolution of navigator data needed for a sequence can have a major impact on sequence design. Larger navigators take more time to acquire. Additionally if the navigator is small enough it may be possible to make a more efficient pulse sequence such as the sequence proposed in the previous chapters, Figure 23.

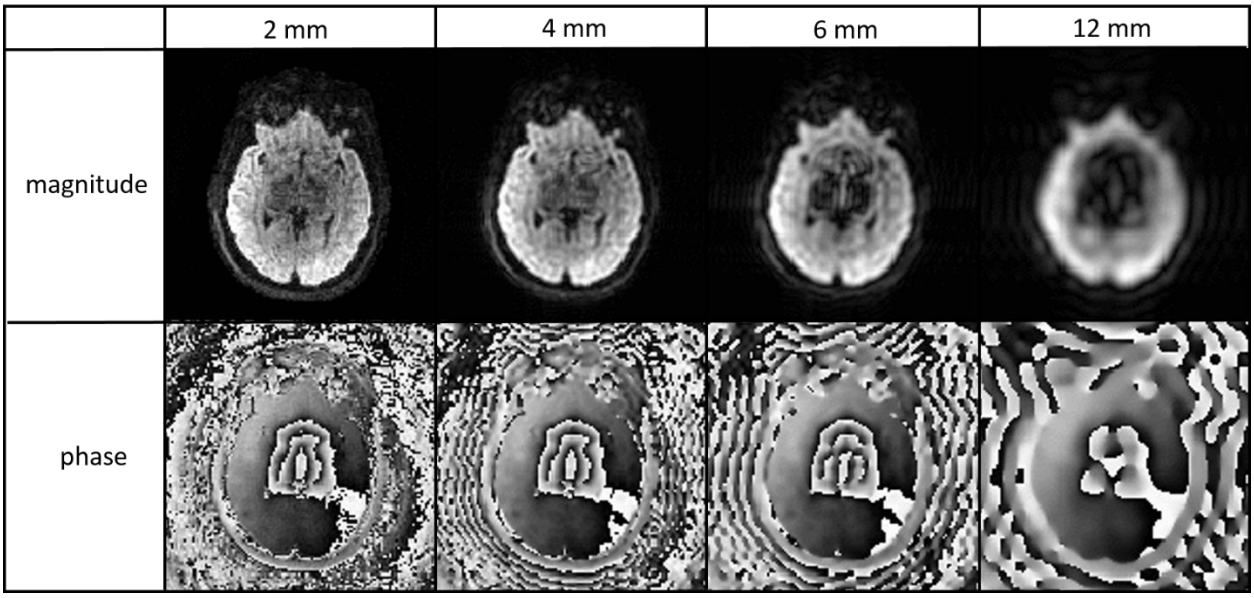

Figure 34: The magnitude and phase of a single shot image with MPE reconstructed to different spatial resolutions

Motion induced phase errors result from coherent motions during the motion encoding gradients that are different between different shots of an acquisition. There are two main classes of motion that are considered when correcting for motion induced phase error. The first class is rigid body motion. These phase errors are due to an object moving without deformation as a rigid body, such as a subject rotating their head. It has been shown that rigid body motions result in phase errors that are linear in image space or, equivalently, are phase offsets and shifts in k-space [64]. The other class of motions lead to nonlinear phase errors in image space which come from non-rigid motions of the object. When looking at the brain, the main cause of non-rigid motion is motion due to cardiac pulsation. These non-rigid motions lead to phase errors that have more complex spatial variations and potentially require sampling higher spatial frequencies in k-space.

Defining the requirements for a navigator is challenging as there are many factors that will impact how the phase error appears. Figure 35 gives an example of a 2 shot sequence that was reconstructed with navigators at different resolutions. Despite the two images being of the same

object, the MPE is different in the two cases, leading to different results when reconstructed with different navigators.

The amount of motion, the timing of the motion, the size of motion encoding gradients, and the direction that the gradients are applied in all play major roles in the MPE. In this section the result of several simulation and in vivo experiments will be shown that aim to provide guidelines on the requirements needed to accurately correct MPE in diffusion weighted imaging. First, we demonstrate the spatial resolution requirements resulting from the motion of the brain stem in simulation. Then weverify the simulation results by comparing to in vvio data on several subjects. Finally, we reconstruct images with navigators of different spatial resolutions to determine what point the MPE impacts image SNR.

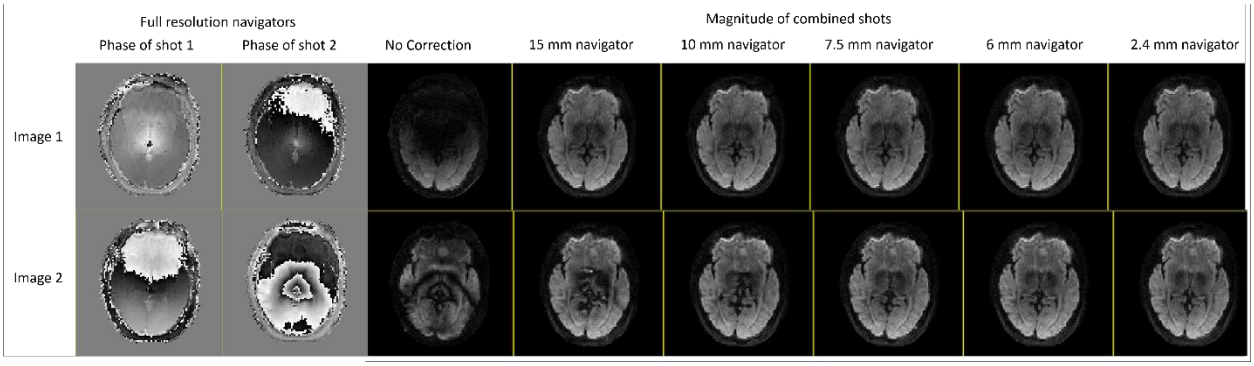

Figure 35: DWI reconstructed with navigators of different spatial resolutions.

Simulation

A mathematical model of the brainstem motion [95] has been proposed and used in other assessments of MPE [96]. This model describes the motion of the brainstem in the "z direction". Figure 36 describes the models spatial variation of velocity at the time of maximal movement. In Figure 37, the time dependence of the velocity of the brainstem movement is displayed. In this model the brainstem's motion is symmetric in the x-y plane and also with respect to its peak velocity in the time dimension.

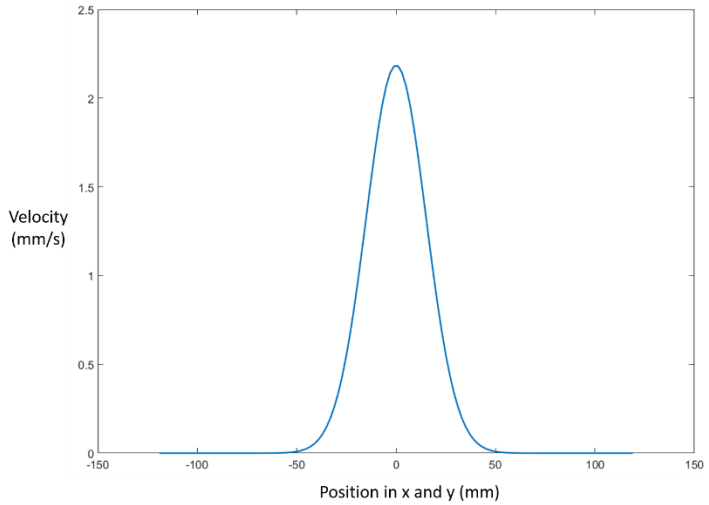

Figure 36: Model of peak brainstem velocity in the x and y direction

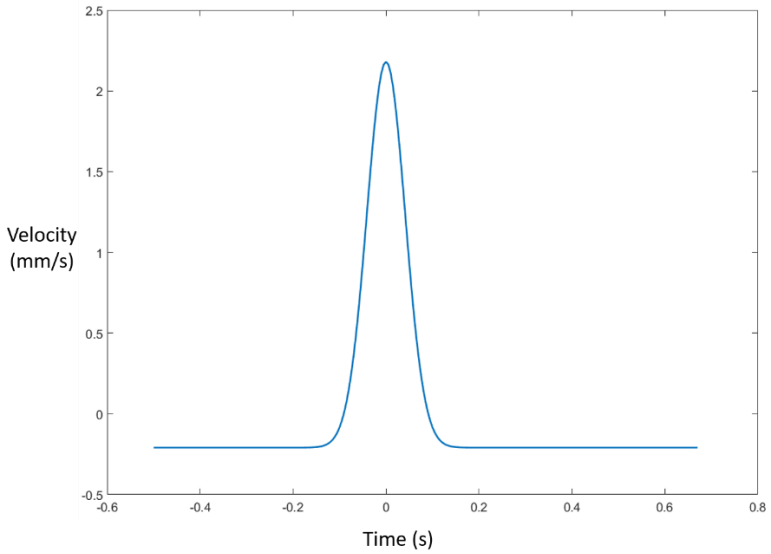

Figure 37: Model of peak brainstem velocity during cardiac cycle

Using a PGSE acquisition the types of phase errors that are expected using the model of brainstem motion can be estimated. For the simulations shown, the worst case situations are displayed. In these cases, the diffusion gradient is in the slice direction, which has the largest displacement in the model, and the slice of interest is the slice experiencing the maximum displacement.

Table 2 outlines the timings used for the diffusion encoding for the simulation. A 0 ms offset time means that the peak of velocity in time profile is aligned with the center of PGSE diffusion encoding. The other offsets are then based on the center reference point. The different gradient strengths represent the gradient strength that was used to encode diffusion. These simulations use a fix amount of time, 5 ms, between the diffusion encoding gradients, with all diffusion encoding designed with rectangular gradients for minimal diffusion time with a PGSE sequence. The gradient strengths were chosen as they represent the maximum gradient strength of several common systems currently in use on human systems.

Table 5: Diffusion parameters of simulation of phase profiles due to cardiac motion.

	200 s/mm^2		700 s/mm^2		1000 s/mm^2		2000 s/mm^2	
G (mT/m)	delta (ms)	DELTA (ms)	Delta (ms)	DELTA (ms)	Delta (ms)	DELTA (ms)	Delta (ms)	DELTA (ms)
26	16.2	21.2	25.6	30.6	29.2	34.2	37.2	42.2
34	13.2	18.2	21.1	26.1	24.0	29.0	30.8	35.8
80	6.8	11.8	11.1	16.1	12.7	17.7	16.5	21.5
300	2.2	7.2	3.8	8.8	4.4	9.4	5.9	10.9

The first case is to look at the type of phase variations that are expected at low b-values. The value of 200 s/mm^2 is useful as values below that are typically associated with a high amount of blood flow. Values over 200 s/mm^2 are typically used to examine the diffusion of water. Figure 38 shows the result of the motion induced phase in the 200 s/mm^2 b-value case. In this case there is very little high frequency phase patterns even at the lowest gradient strength and hence the largest diffusion encoding time.

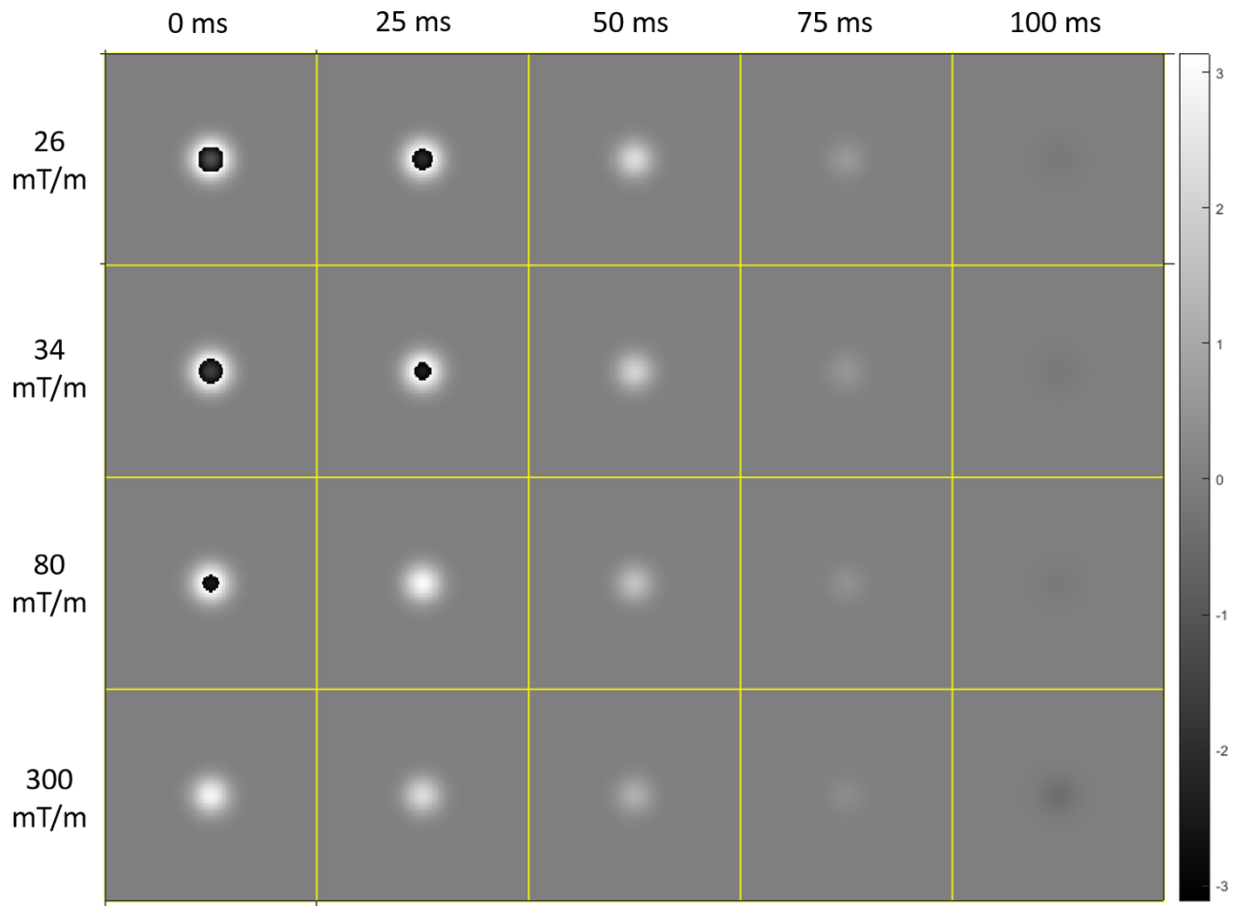

Figure 38: Phase variation maps at different points in the cardiac cycle using different gradient strengths to encode a b-value of 200 s/mm² in minimal time.

The lack of of high frequency phase patterns can be seen by taking the Fourier transform of the phase map, where the phase map is first converted to a complex value with unit amplitude. For the 200 s/mm^2 case the resulting frequency contents in the simulations can be seen in Figure 39. In the worst case scenario with gradient timings coinciding with cardiac motion and using low amplitude gradients, there is no spatial information below 8 mm. At the highest gradient strength of 300 mT/m a resolution of 10 mm is enough to fully capture all the spatial variations for the worst case movement. At the time points further from the peak, the matrix size that is needed to fully capture the spatial information in the phase is even lower.

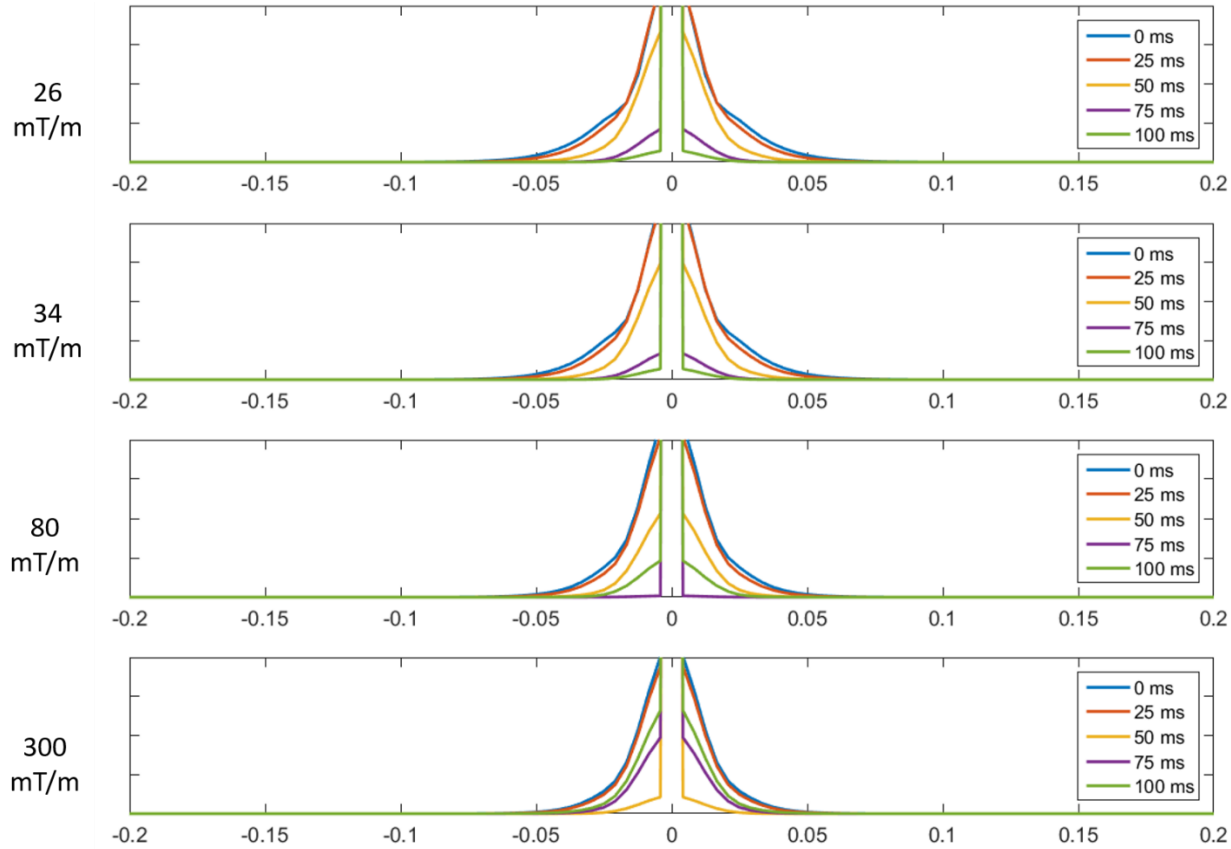

Figure 39: Spatial frequencies (mm^{-1}) in navigators at 200 s/mm^2

Going up to a b-value of 700 s/mm^2 begins to show more high frequency phase information indicative of increased amount of phase wrap in the images, Figure 40. The 700 s/mm^2 b-value was chosen at it is near the bottom of the range that is commonly reported for use in looking at white matter structure. The spatial frequency content of these navigators is much larger than the 200 s/mm^2 case, Figure 41, with a 5 mm resolution needed to capture all the information. However, with just a 50 ms offset all the spatial frequency information can be acquired with only a resolution of 8 mm at the lowest gradient strength.

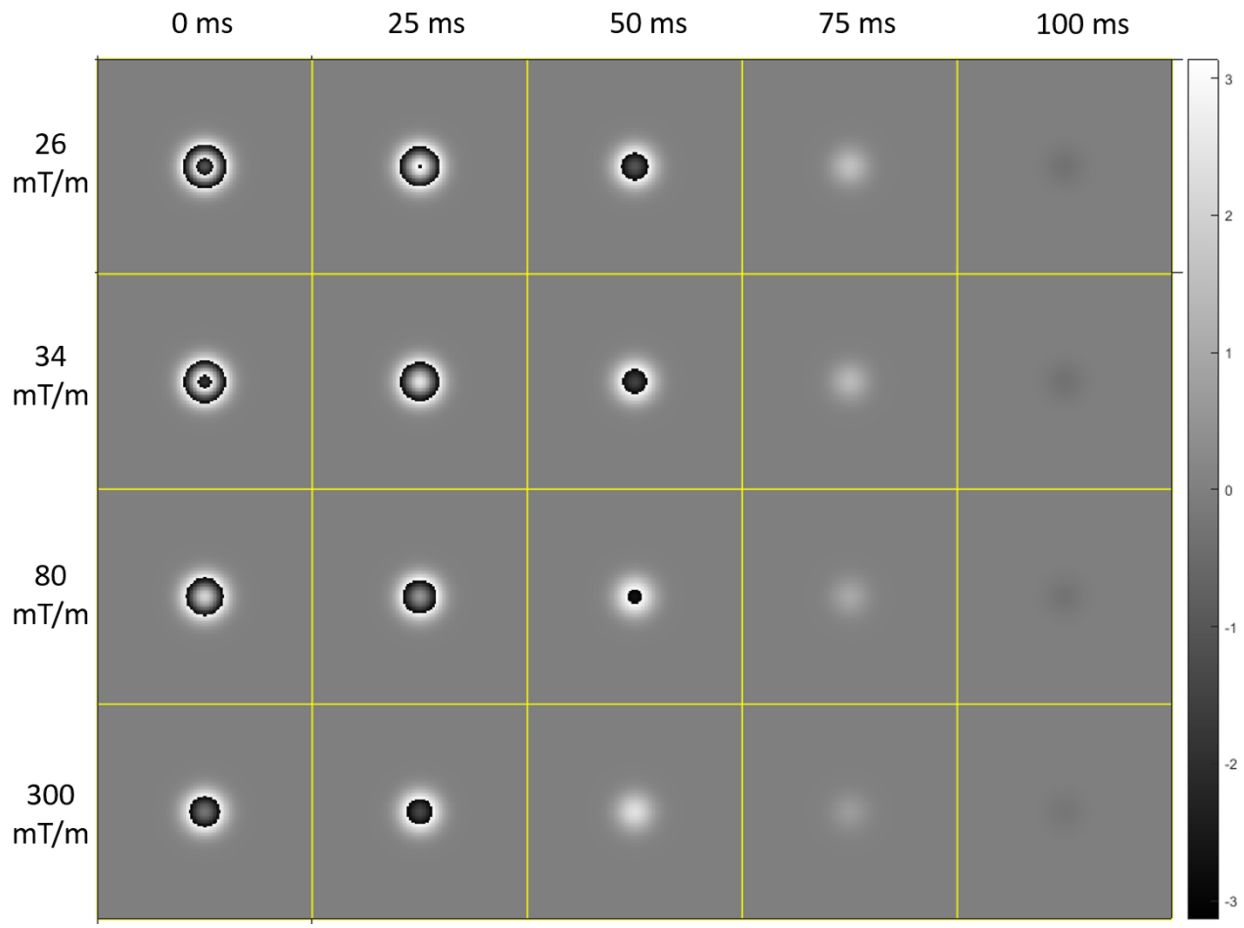

Figure 40: Phase variation maps at different points in the cardiac cycle using different gradient strengths to encode a b-value of 700 s/mm^2 in minimal time.

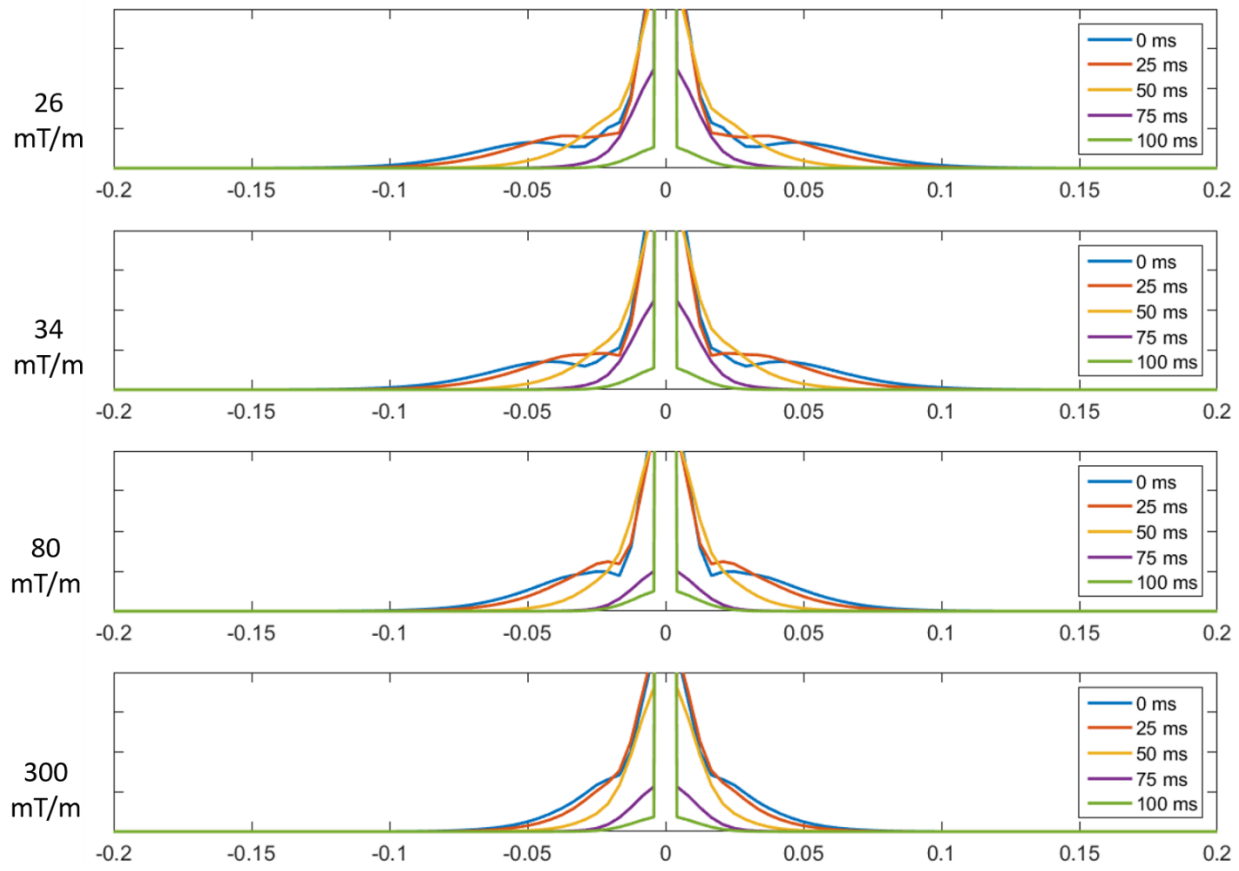

Figure 41: Spatial frequencies (mm^{-1}) in navigators at 700 s/mm^2

At a b-value of 1000 s/mm^2, large phase wraps are visible at the lower gradient strengths, Figure 42, indicating the presence of higher spatial frequency information in the phase. The 1000 s/mm^2 b-value is the most commonly used b-value for studying white matter making these results important to researchers studying the brain. Looking at the spatial frequencies in these plots, Figure 43, it is clear that a much larger navigator is required if all of the spatial variation information is needed. At the 26 mT/m gradient strength a resolution of 4 mm would be needed to sample the frequencies at the 0 ms and 25 ms time point. However, the decay in navigator size that is needed drastically decreases as the sequence moves further from the peak of the cardiac cycle, with a resolution of 12 mm needed at 75 ms away from the peak. Moving up to a gradient strength of 80

mT/m decreases the worst case scenario to a resolution of 5 mm and only 8 mm at a 50 ms offset from the peak.

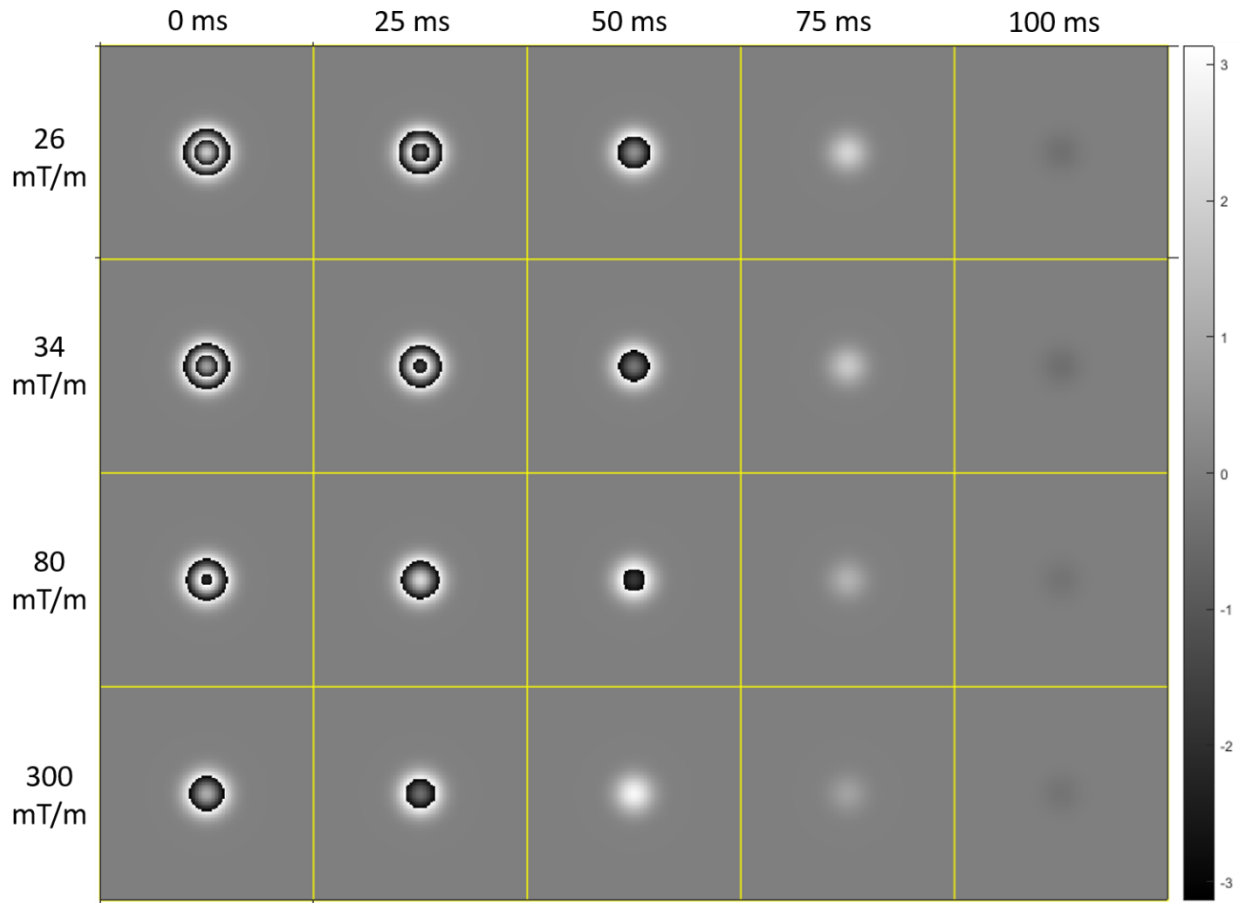

Figure 42: Phase variation maps at different points in the cardiac cycle using different gradient strengths to encode a b-value of 1000 s/mm² in minimal time.

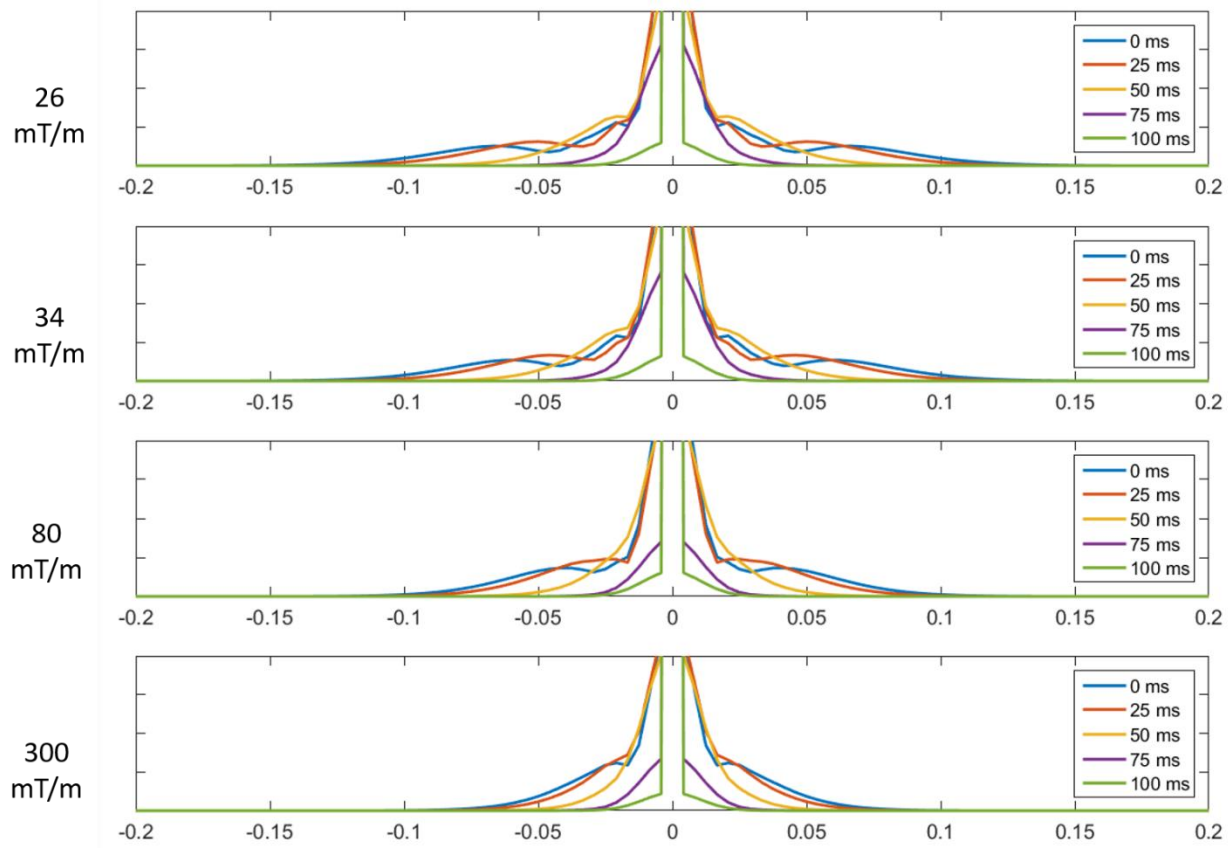

Figure 43: Spatial frequencies (mm^{-1}) in navigators at 1000 s/mm^2

The final b-value for this simulation study was at a b-value of 2000 s/mm^2. Images with this encoding have seen increasing use as multishell models such as NODDI [26] have gained popularity. At a 2000 s/mm^2 b-value much more phase wrap is observed, Figure 44, especially at the lower gradient strengths. The increased phase wraps are noticeable by the increased width of the spatial information in the images, Figure 45.

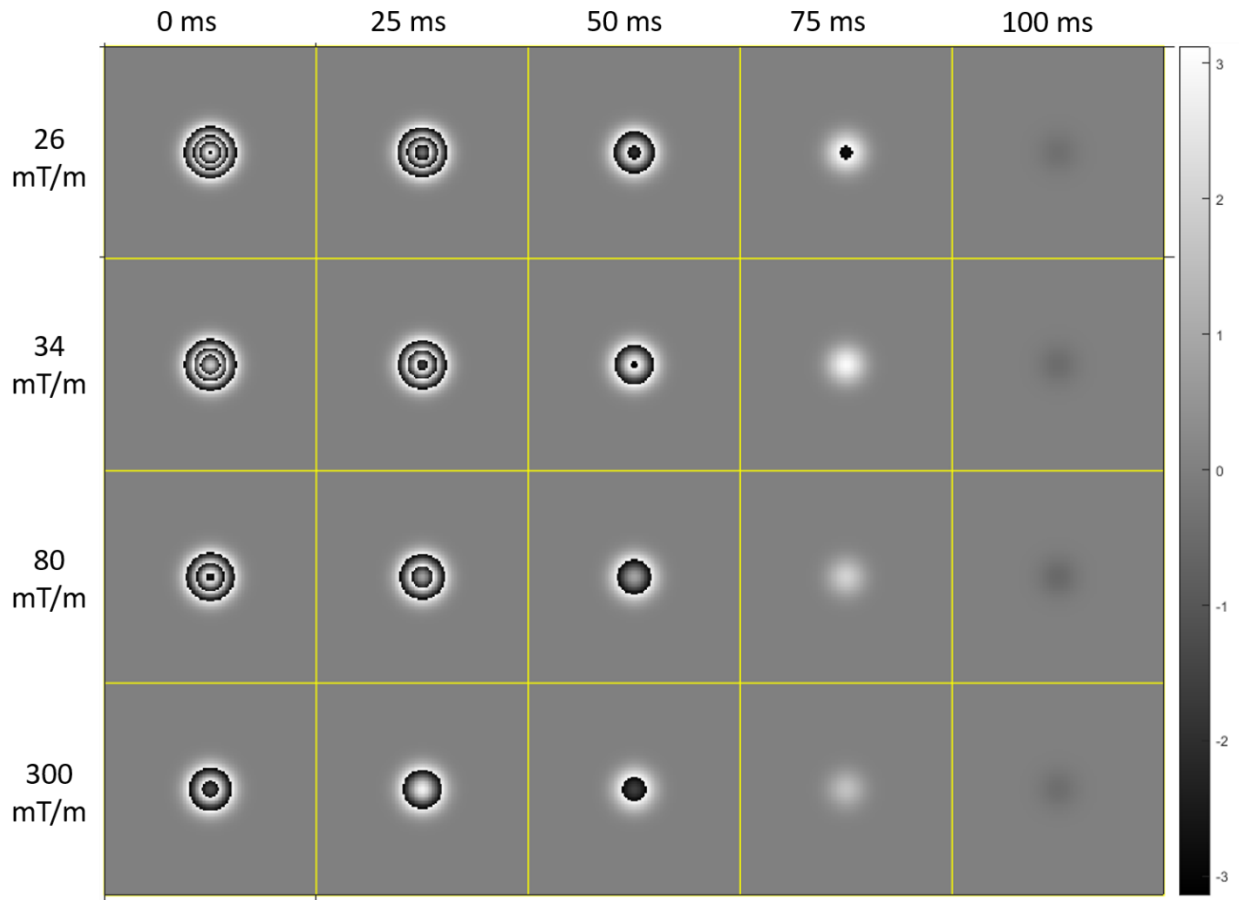

Figure 44: Phase variation maps at different points in the cardiac cycle using different gradient strengths to encode a b-value of 2000 s/mm² in minimal time.

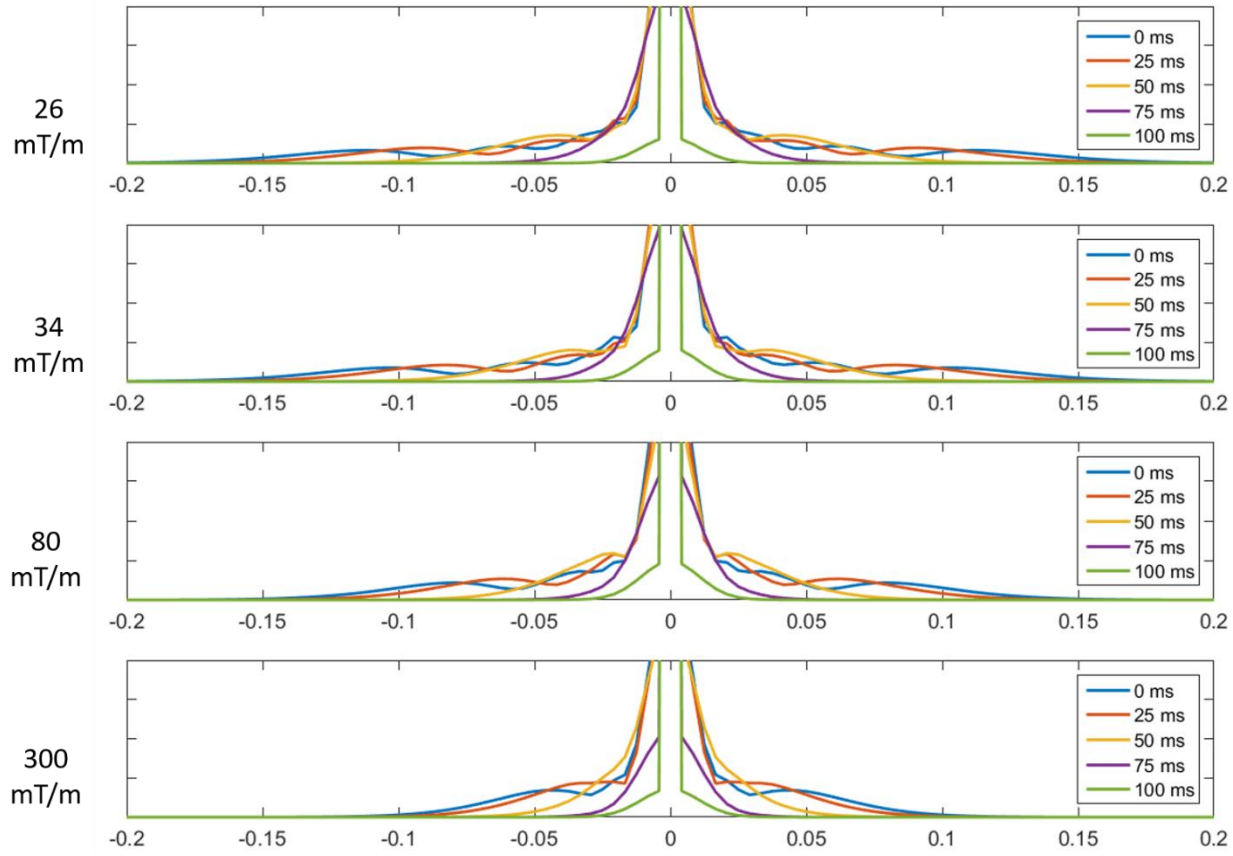

Figure 45: Spatial frequencies (mm^{-1}) in navigators at 2000 s/mm^2

In-vivo validation of simulation results

In order to determine if what was observed in simulation relates to what is observed in vivo, several experiments were run. In this first experiment, a single slice at the level of the brainstem was acquired. The acquisition used a PGSE encoding with a b-value of 1000 s/mm^2 on a 3 T scanner with a maximum gradient strength of 26 mT/m. A single shot imaging sequence was used in order to accurately create images that have magnitude and phase. A photoplethysmography trigger was used for cardiac gating with delays ranging from 0 ms to 900 ms used to sample different parts in the cardiac cycle on a young male volunteer with a heart rate of ~60 beats per minute. 10 repetitions at each trigger delay were acquired to assess variations in the phase. Additionally, the experiment was run for 3 different diffusion encoding directions.

The resulting phase images from the left/right diffusion encoding direction can be seen in Figure 46, from the anterior/posterior diffusion direction in Figure 47, and from the superior/inferior direction in Figure 48. One interesting thing that can be noted is that in all the images, the difference in phase variations across each row are minimal. This suggests that the phase variation due to cardiac pulsation is fairly consistent with location within the cardiac cycle.

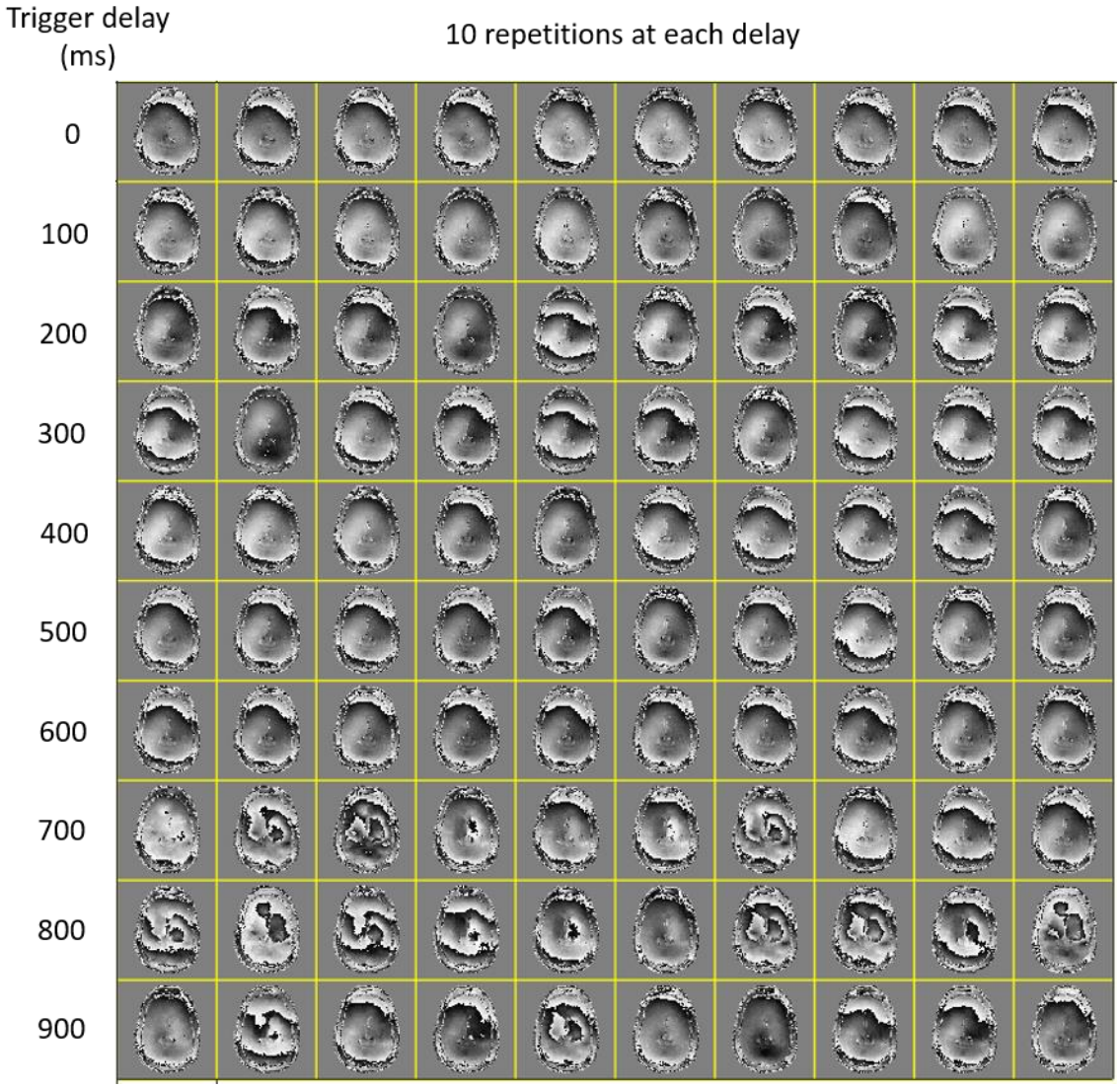

Figure 46: MPE with diffusion gradient in left/right direction at b=1000 at different PPG trigger delays

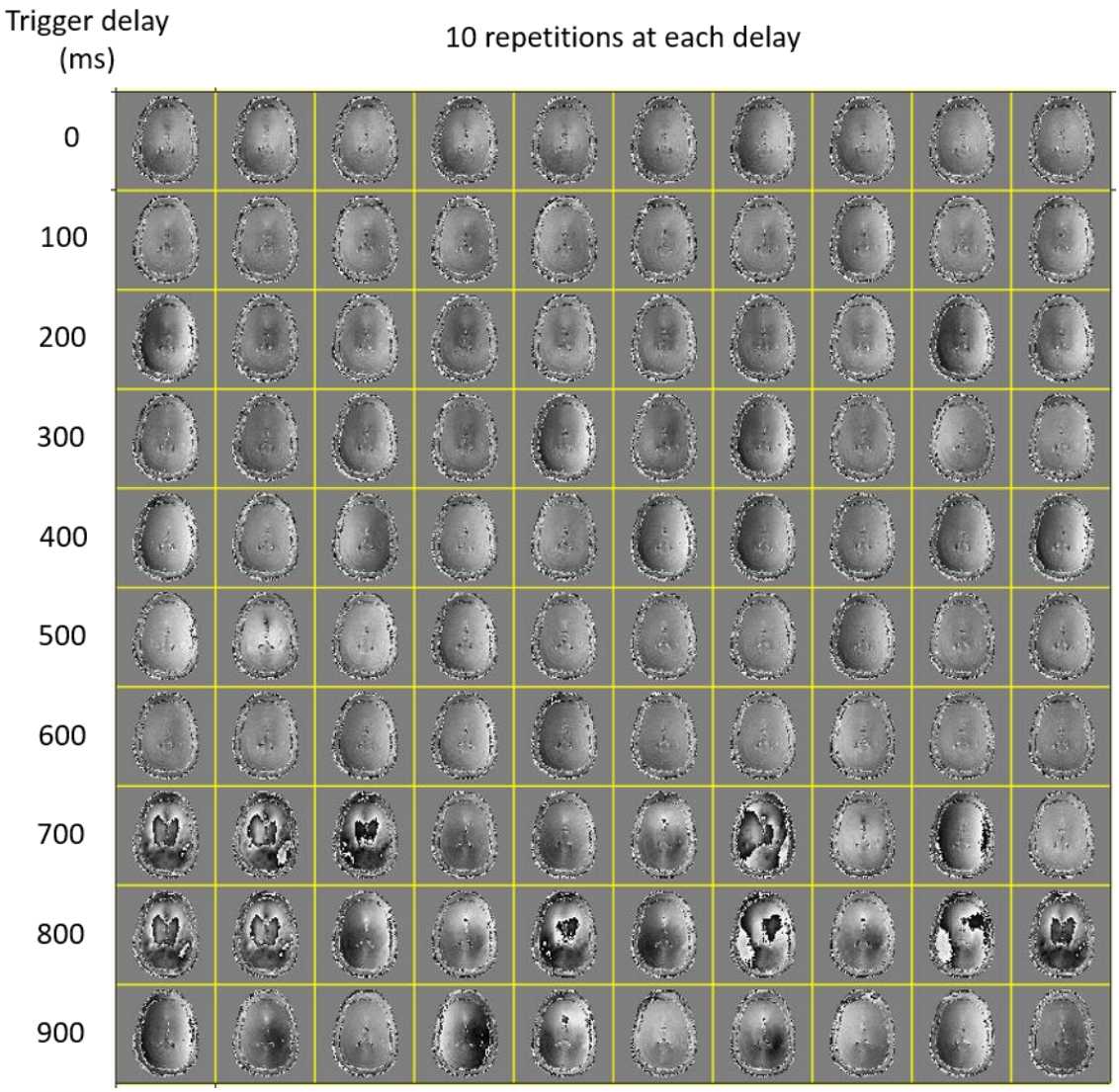

Figure 47: MPE with diffusion gradient in anterior/posterior direction at a b-value of 1000 at different PPG trigger delays

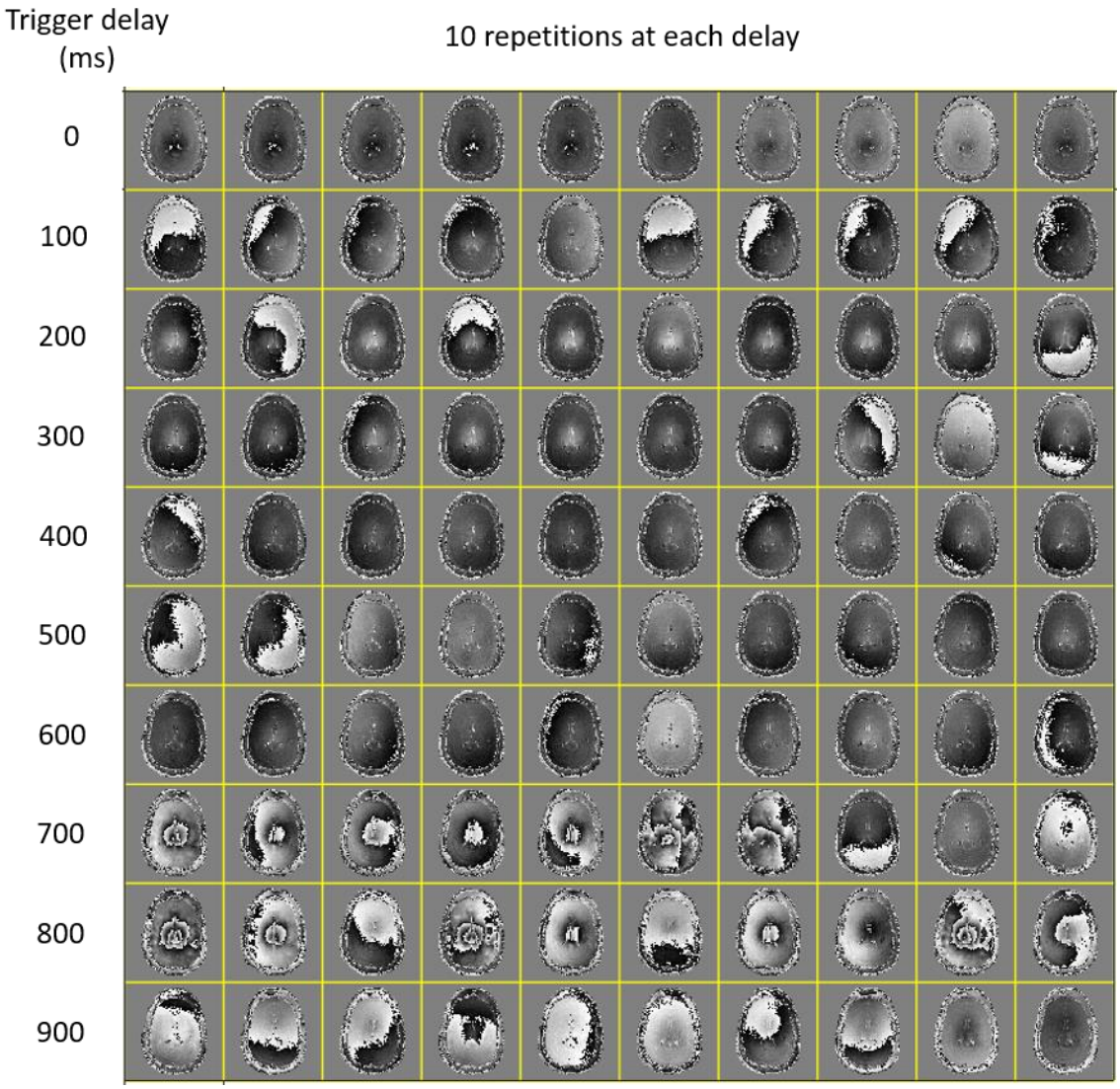

Figure 48: MPE with diffusion gradient in superior/inferior direction at different PPG trigger delays

Another observation that can be made from this data is that the maximal cardiac motion appears to occur at the 700 ms or 800 ms delay from the PPG trigger for this subject. At time points away from the cardiac pulsatile motion, there is very little difference between the time points, which suggests very little pulsatile cardiac motion.

Comparing the different directions of diffusion encodings it can be seen that different phase patterns are observable. During the cardiac pulsation time period the phase variations for the case of diffusion encoding in the superior/inferior direction contain much larger phase variations. This

suggests that diffusion in the superior/inferior direction is most susceptible to large errors due to MPE. This makes sense given that the cardiac-induced pulsation causes the most movement in this direction.

Because most of the time points away from peak cardiac pulsation contain little differences in phase variation within them, a second experiment was run with the same imaging parameters but with different triggering criteria, in order to more closely look at the time points impacted by cardiac pulsation. For the second experiment an ECG trigger was used in order to decrease the delay time between the triggering and the peak of the cardiac pulsation. The cardiac cycle was also tested with a finer temporal resolution with time points acquired at trigger delays of 0 ms to 200 ms at every 20 ms. The resulting phase images for the diffusion encoding gradient directed in left/right, anterior/posterior, and superior/inferior directions can be seen in Figure 49, Figure 50, and Figure 51 respectively.

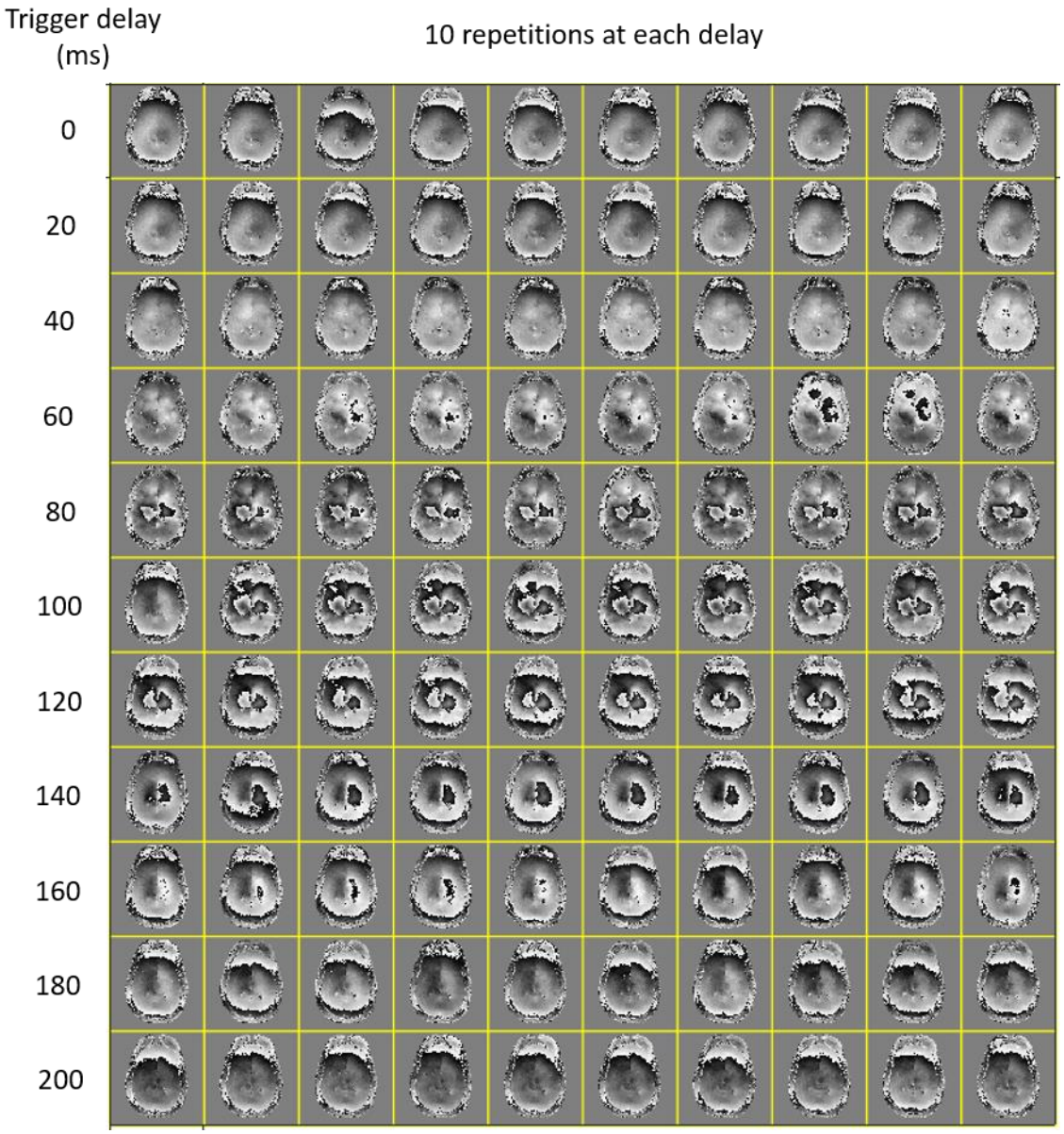

Figure 49: MPE with diffusion gradient in left/right direction at different ECG trigger delays

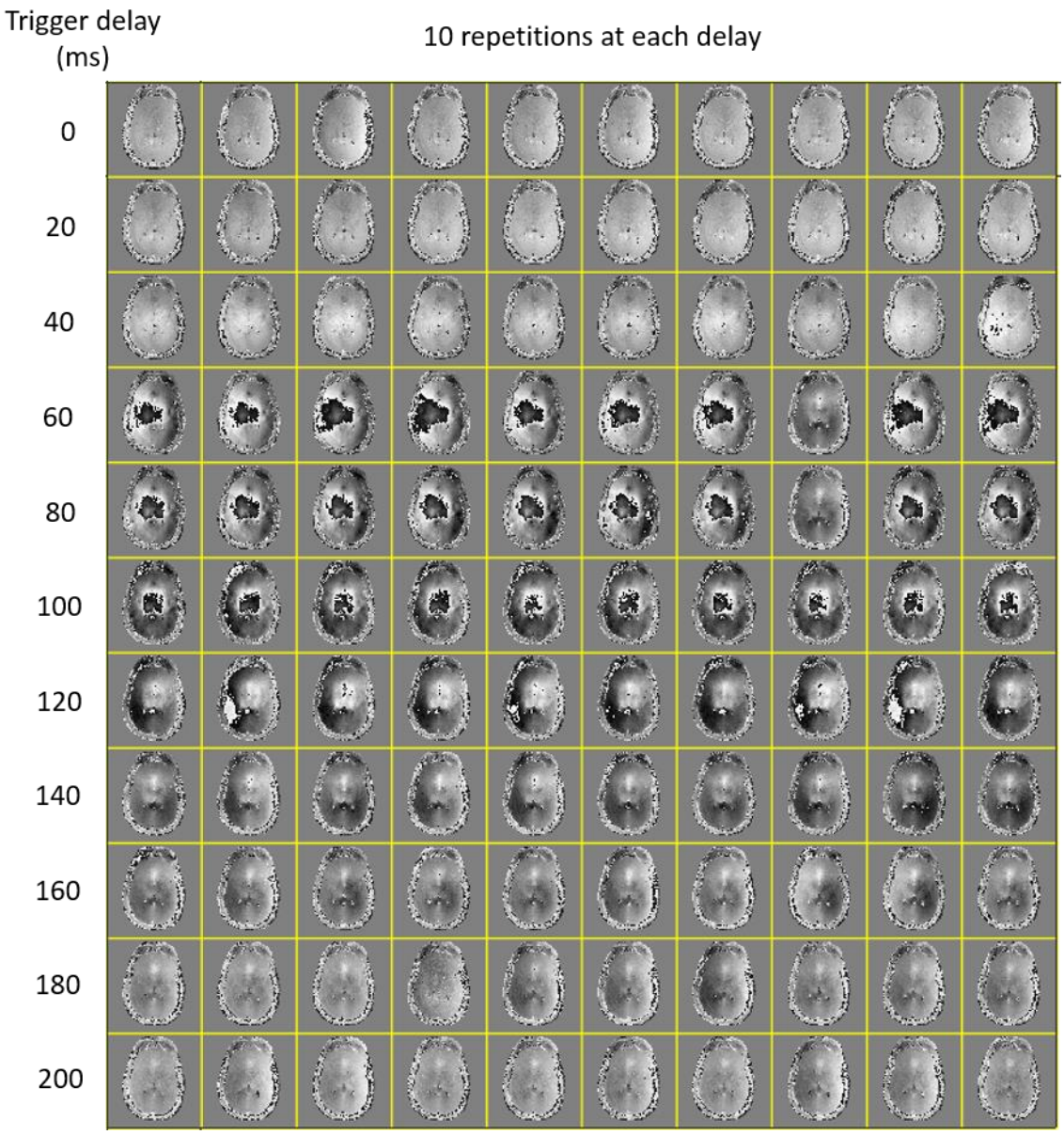

Figure 50: MPE with diffusion gradient in anterior/posterior direction at different ECG trigger delays

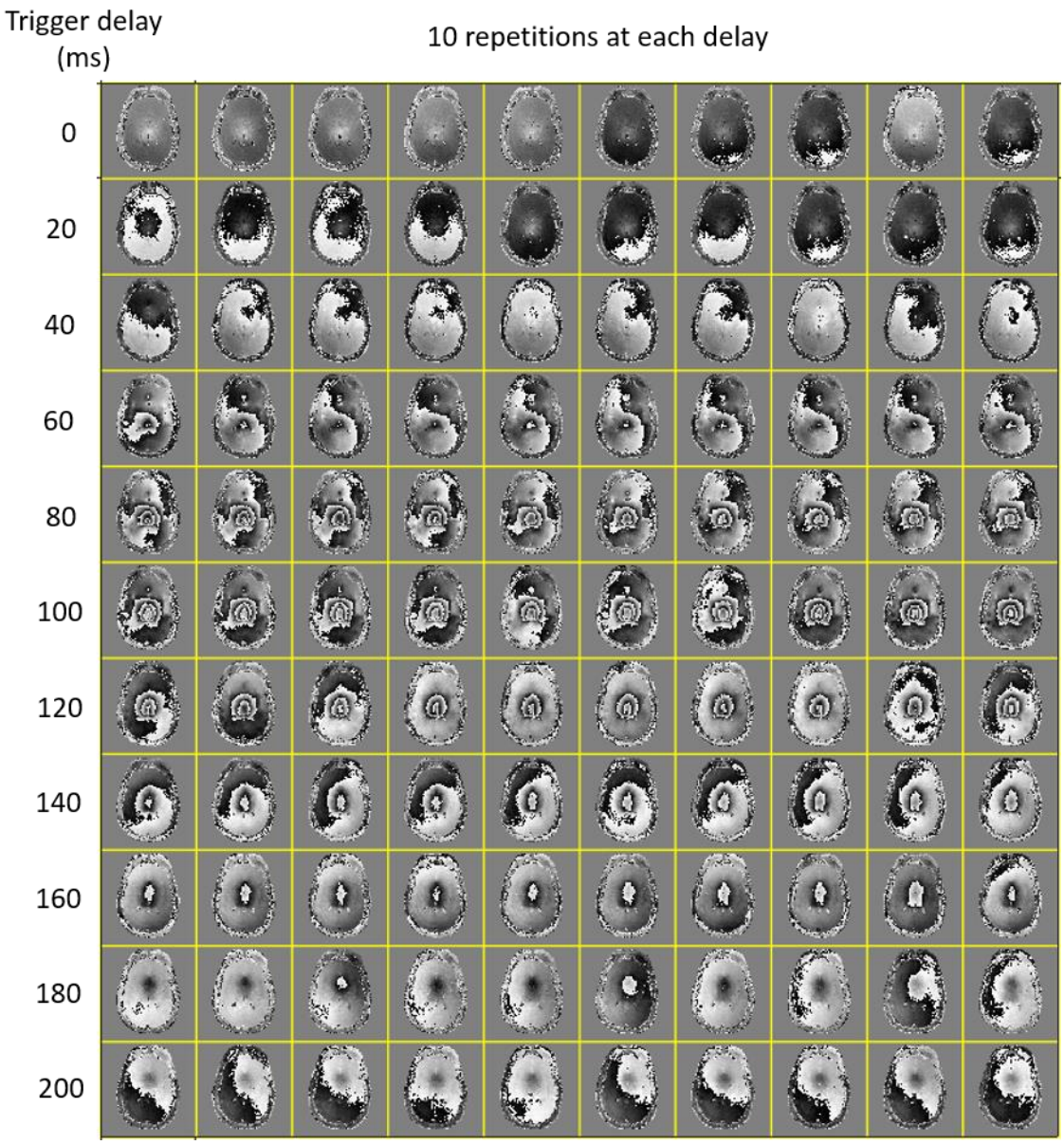

Figure 51: MPE with diffusion gradient in superior/inferior direction at different ECG trigger delays

These results better demonstrate the repeatability of the cardiac motion across a trigger delay. The larger variations in the phase profile are still shown in the superior/inferior direction. To look at the type of spatial information that are in these phase images, the Fourier transform on the phase image with unit magnitude are once again taken like in the simulation. In the simulation the model of brainstem motion was symmetric in the x and y direction, however in the real data there is no strong reason to expect symmetry, therefore the point spread will be given in both in-

plane directions. The resulting spatial features for the left/right, anterior/posterior, and superior/inferior directions can be seen in Figure 52, Figure 53, and Figure 54 respectively.

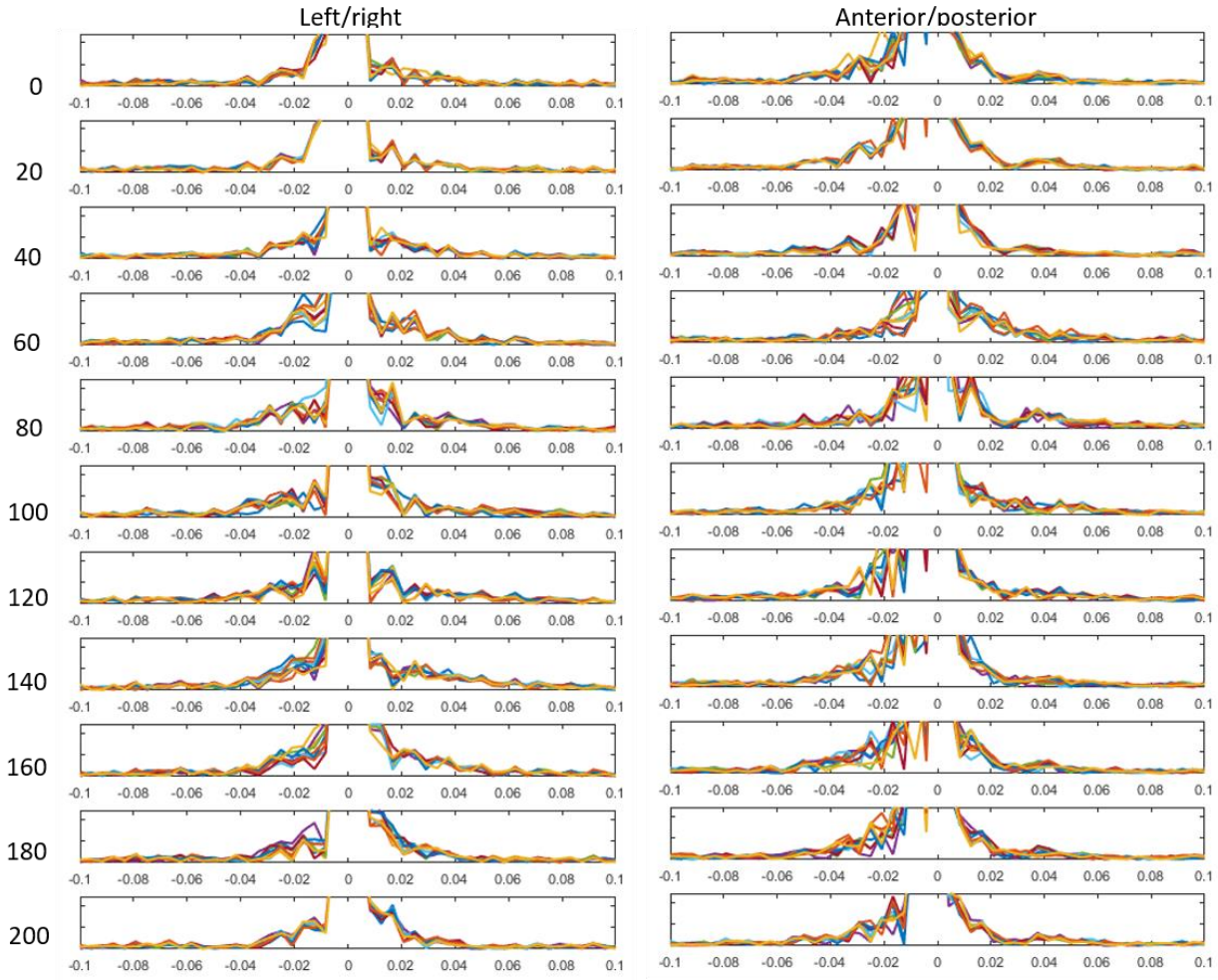

Figure 52: Spatial frequencies in left/right direction at different ECG trigger delays

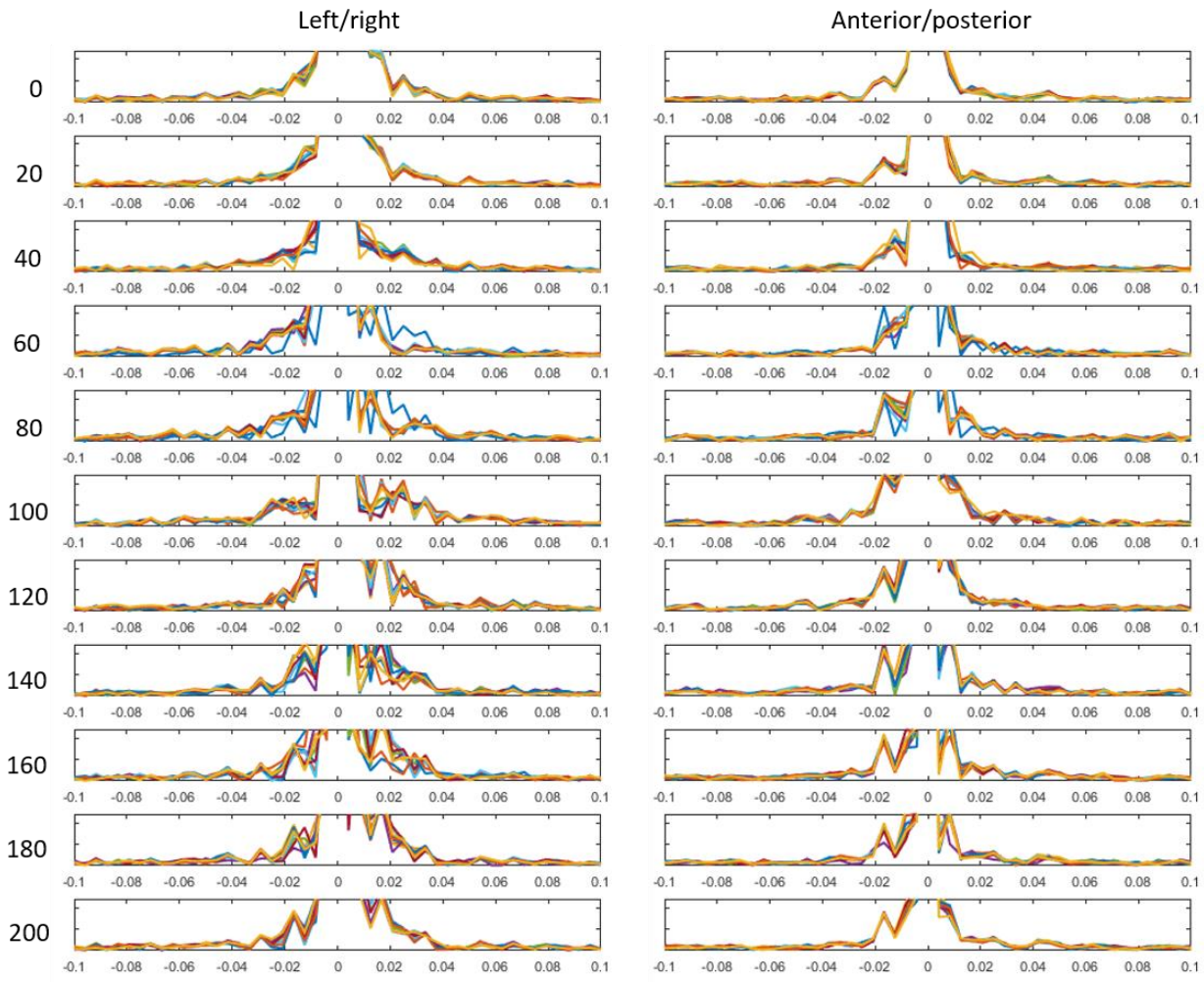

Figure 53:: spatial frequencies (mm^{-1}) in anterior/posterior direction at different ECG trigger delays

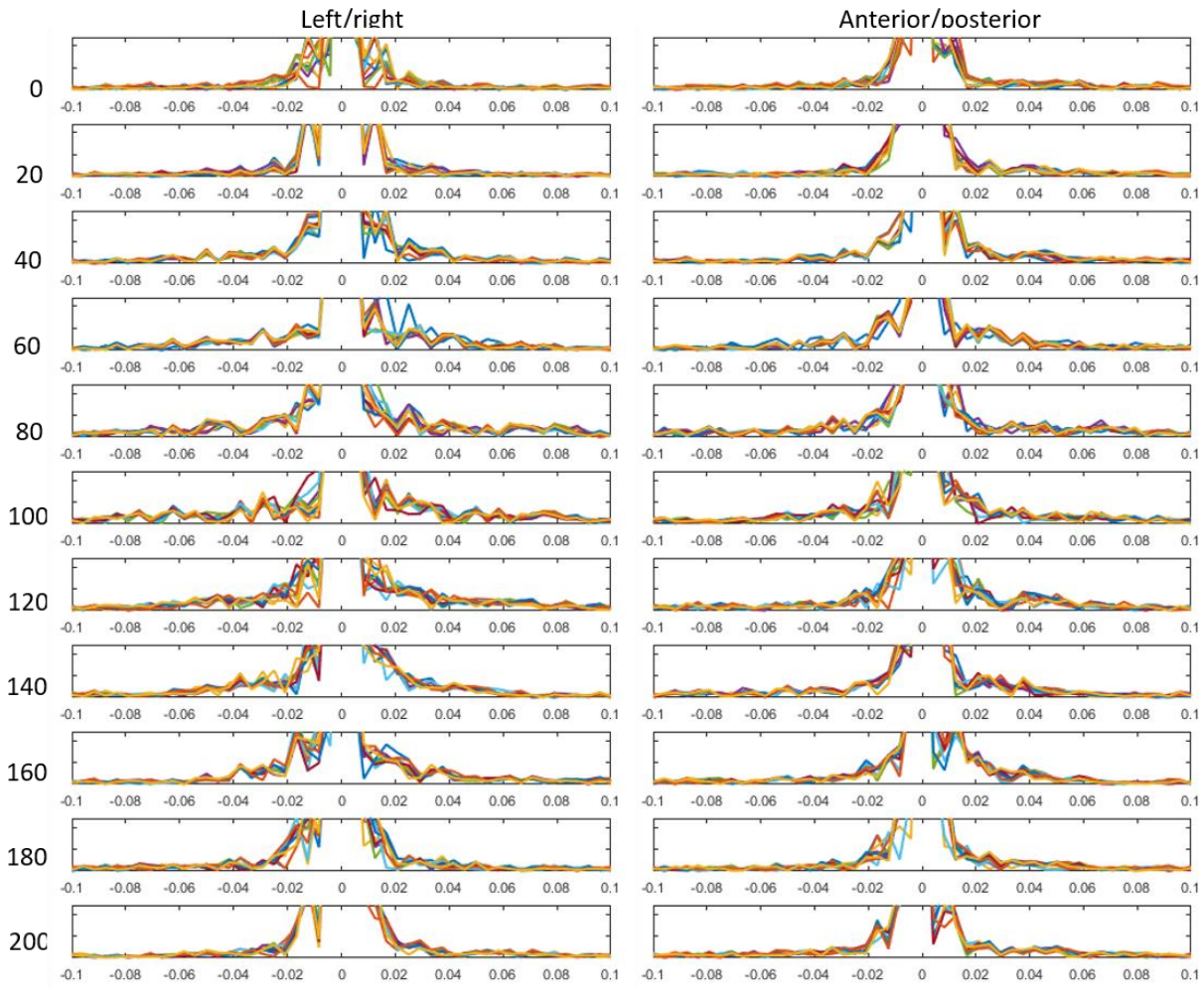

Figure 54: spatial frequencies (mm^{-1}) in superior/inferior direction at different ECG trigger delays

Looking at the spatial frequencies contained in the images several observations can be made. Compared to the simulated brainstem motion, the shape of the real data is much less smooth than the simulation case. The real data also does not go to zero as the simulation data set did, this makes choosing a cutoff threshold for what amount of information is needed in the navigator to be more complicated. The figures do show that the width of the PSF is wider in the superior/inferior direction, confirming what would be expected by looking at the phase profiles. Generally speaking, much of the information seems to be contained within a resolution of 8 mm for all these cases, although there is still signal outside these regions. The 8 mm resolution is slightly lower than the comparable simulation parameters that found that all the information could be captured with a 4

mm resolution. However, the difference between the in vivo data and simulation could be due to not having strict criteria for defining the amount of signal that needs to be captured to perform MPE correction in the in vivo data.

Impact of MPE on reconstructed image SNR

In order to further examine the impact of differing spatial resolutions in the navigator, a simulation study was designed to use the phase information from in vivo recordings to reconstruct simulated data where the ground truth image is known. Based on these phase maps at different points of the cardiac cycle, data was simulated using these different phase variations and an image reconstruction was performed. However, performing these simulations revealed the complexity of assessing the ability of a particular navigator design in correcting for MPE. The quality of the resulting images were heavily dependent on the number of shots used, the k-space trajectory, and where each shot occurred during the cardiac cycle. Instead of running an experiment with many results that would be hard to interpret, and potentially be specific to a single subject, a third experiment was performed.

In the third experiment, we resorted to acquiring a data set in vivo that would enable us to examine the impact of spatial resolution of the navigator on real reconstructions. A 2-shot diffusion weighted image sequence was used to acquire 40 slices in the brain without any cardiac gating. A b-value of 1000 s/mm^2 was used to acquire diffusion encoding in three separate directions with 25 repeats of each direction. The sequence used a spiral readout with each shot having a reduction factor of 2, such that we were able to reconstruct a full resolution image using parallel imaging from either the navigator or the imaging data. Because of this, a navigator image was able to be reconstructed for each desired spatial resolution, by discarding data from higher spatial resolutions in k-space.

With a range of navigator resolutions, fully sampled images were reconstructed by combining 2 shots and using CG-method for MPE correction [41]. At each navigator resolution and for each diffusion direction, the temporal SNR could then be estimated as a means to assess the completeness of the correction from that navigator resolution. By looking at the point where the SNR begins to decrease, an intuition of what size navigator is needed for the diffusion encoding used in this experiment can be gained. The navigator sizes given are based on having an FOV of 240 mm.

This work has focused primarily on the motion of the brainstem in the superior/inferior direction, if a plot of the normalized SNR vs the navigator size is examined, Figure 55, several interesting conclusions can be made. For two of the three subjects examined the SNR begins to decrease around a navigator with 7.5 mm resolution. For the other subject, the SNR does not decrease until a 12 mm resolution navigator is used and does not rapidly decrease until a 20 mm resolution. This demonstrates that there is significant subject variability in the amount of motion that could be expected. In order to determine what values are normal, a larger population of subjects would need to be run. For these specific subjects acquiring a navigator with a resolution over 6 mm would not be beneficial and would be a waste of time. For most cases, if a 10% loss of signal can be tolerated in the analysis procedure, a resolution of 12 mm is all that is needed. For these subjects and diffusion encoding used, a resolution of 8 mm give almost no loss in SNR, suggesting that an 8 mm resolution navigator is what is needed for complete correction of MPE, regardless of the k-space trajectory for the imaging data.

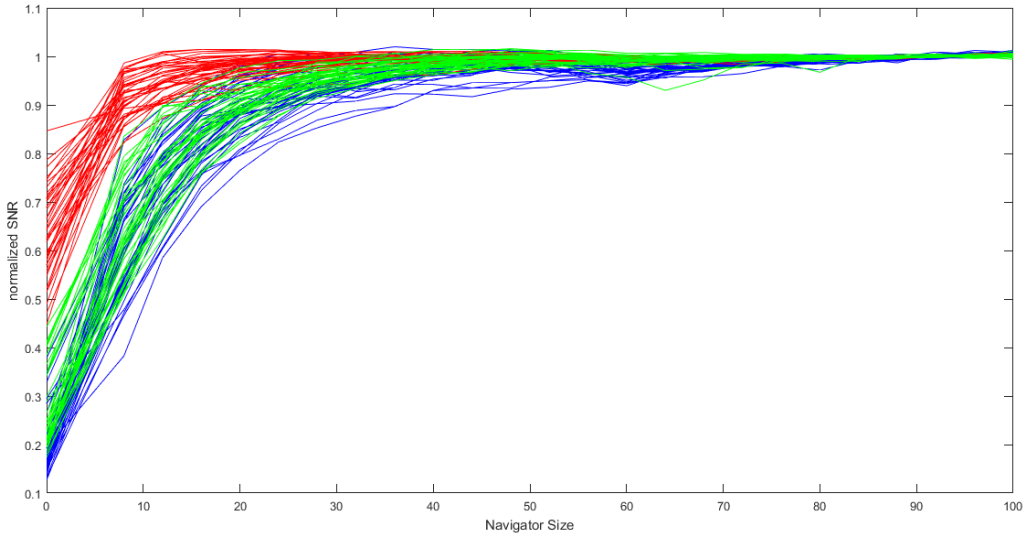

Figure 55: Normalized SNR for each slice in time series reconstructed using navigators of different sizes with diffusion encoding of 1000 s/mm² in the superior/inferior direction. The different colors represent data from different subjects.

To make sure that the motion in the slice direction is the most import for MPE correction, the same analysis was also run on diffusion gradients in the left/right direction, Figure 56, and the anterior/posterior direction, Figure 57. These results did not follow the expectations of the theory of brain motion being mainly in the superior/inferior direction. The left/right encoding provided much higher navigators for the reconstruction than the superior/inferior direction. Meanwhile the anterior/posterior encoding followed the expectation of having a smaller navigator necessary. This can be more clearly seen by looking the different subjects with their 3 diffusion encoding directions on the same graph, Figure 58, Figure 59, and Figure 60. For all of the subjects the left/right encoding required a higher resolution navigator.

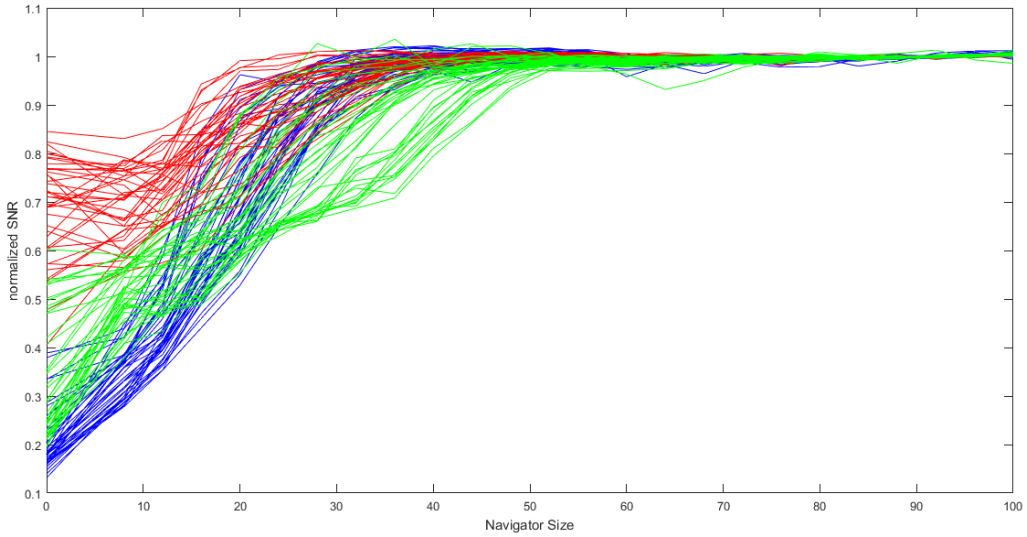

Figure 56: Normalized SNR for each slice in time series reconstructed using navigators of different sizes with diffusion encoding of 1000 s/mm2 in the left/right direction. The different colors represent data from different subjects.

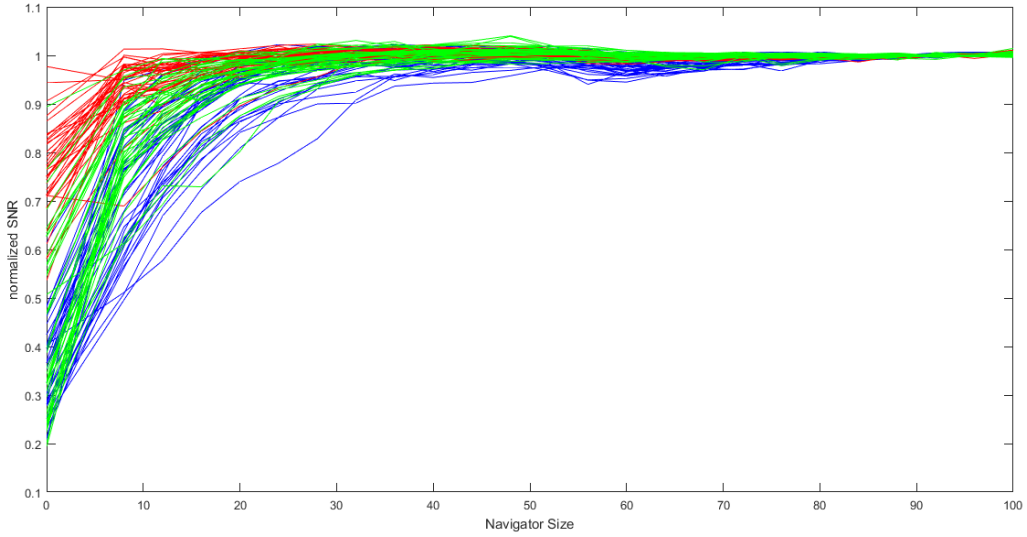

Figure 57: Normalized SNR for each slice in time series reconstructed using navigators of different sizes with diffusion encoding of 1000 s/mm2 in the anterior/posterior direction. The different colors represent data from different subjects.

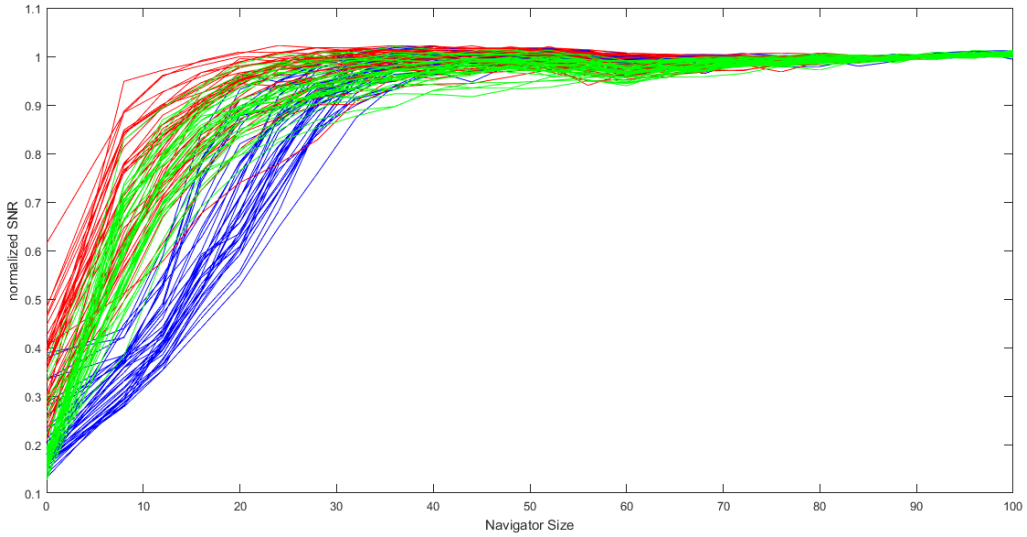

Figure 58: Normalized SNR for each slice in time series reconstructed using navigators of different size for subject 1. A b-value of 1000 s/mm² with diffusion encoding in the left/right (blue), anterior/posterior (red), and superior/inferior (green) direction.

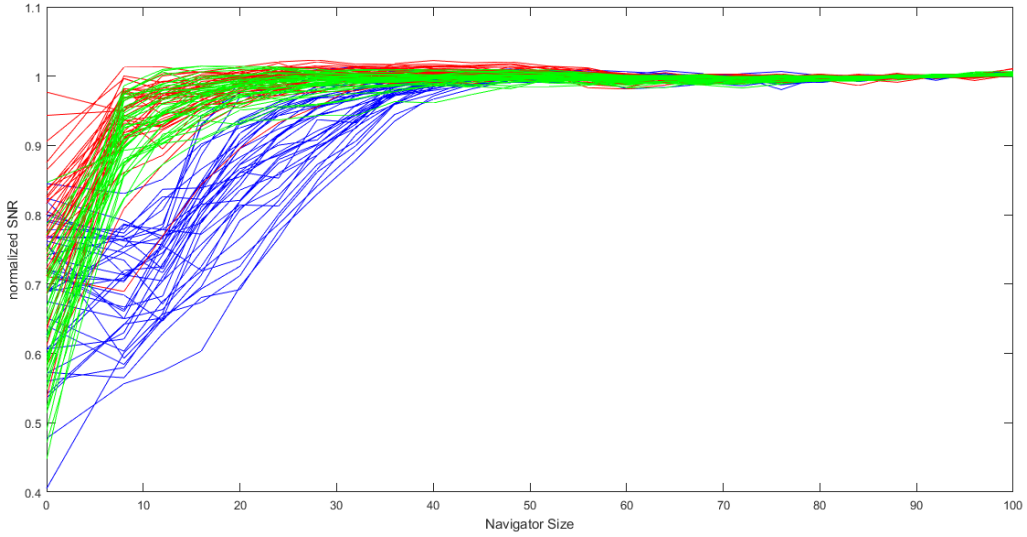

Figure 59: Normalized SNR for each slice in time series reconstructed using navigators of different size for subject 2. A b-value of 1000 s/mm2 with diffusion encoding in the left/right (blue), anterior/posterior (red), and superior/inferior (green) direction.

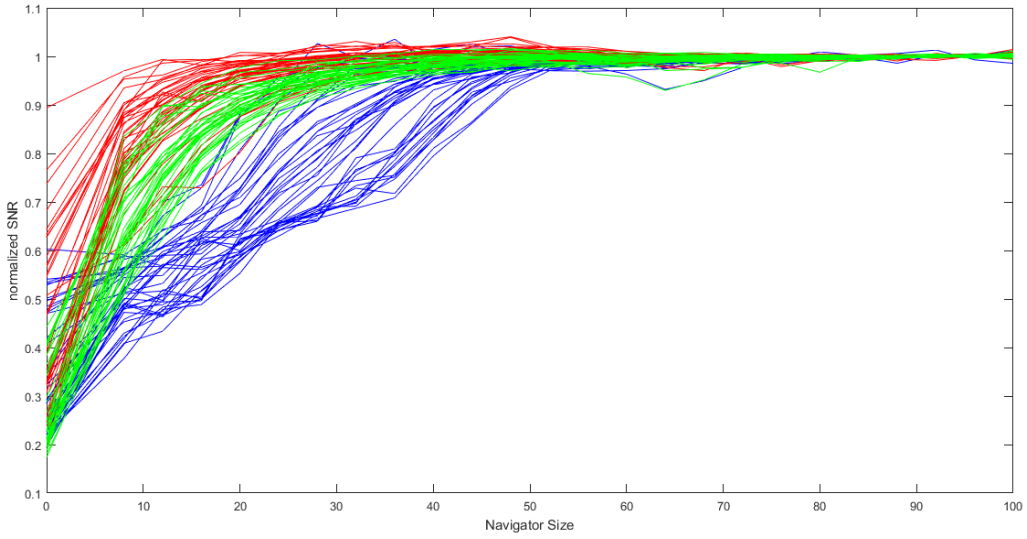

Figure 60: Normalized SNR for each slice in time series reconstructed using navigators of different size for subject 3. A b-value of 1000 s/mm2 with diffusion encoding in the left/right (blue), anterior/posterior (red), and superior/inferior (green) direction.

By looking at the estimated MPE for a slice that had encoding in the left/right direction, Figure 61 and Figure 62, an idea about where the increased resolution needed for navigation comes from can be made. The image shows a phase pattern similar to a ramp, which is caused by rigid body motion, this suggests that the movement in during the left/right encoding is not localized, but most likely the entire head moving. A likely cause of this is the scanner table shaking. In the most of the previous experiments only a single slice was acquired using cardiac gating, making for a sparse acquisition in time with lots of dead time between acquisitions. However, in this specific experiment, unlike the previous cardiac gated experiments, many slices were acquired, without any cardiac gating, resulting in a much shorter amount of time between adjacent acquisitions. The large gradients used in diffusion encoding have been known to have issues on some systems, such as shaking the table of the MRI scanner [97, 98]. The issue of table shaking is the likely reason why the navigators needed for the left/right correction were so large. In practice, controlling for this is challenging as the amount of shaking will depending on the specific timings of the sequence,

however this hardware issue is a feature that has been improved upon in newer versions of hardware.

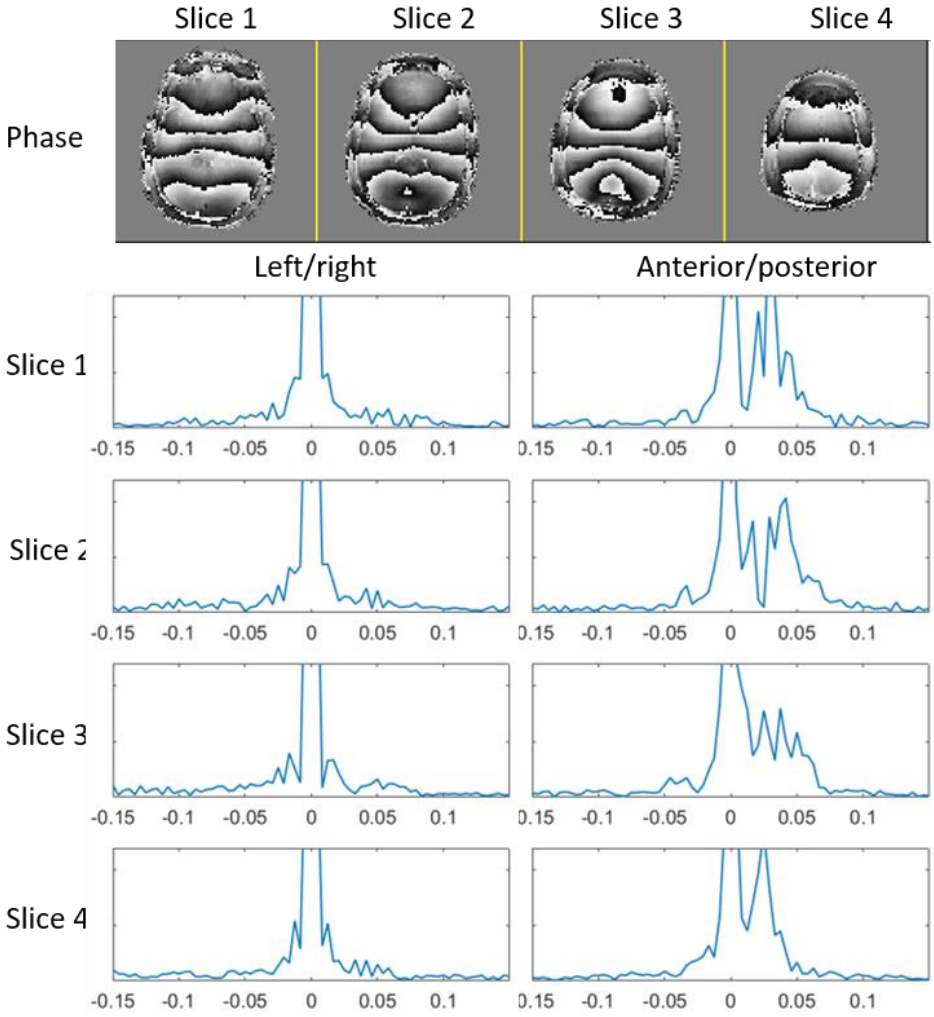

Figure 61: Estimate MPE from a left/right diffusion weighting direction in subject 1.

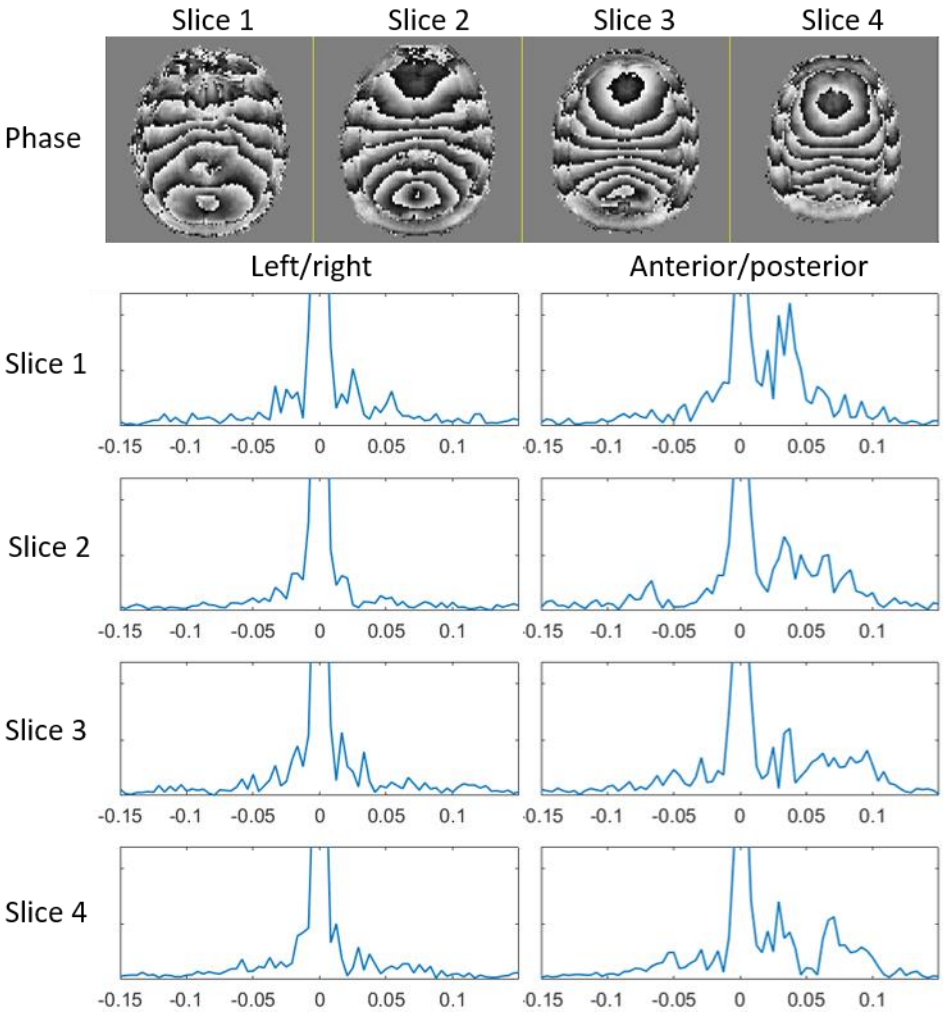

Figure 62: Estimate MPE from a left/right diffusion weighting direction in subject 3.

Looking at the frequency content in the navigators in left/right direction for subject 1, Figure 61, and subject 3, Figure 62, it can be seen that a much higher resolution navigator is needed in order to sample the spatial variations seen in the phase. For subject 1, a resolution around 6.5 mm appears to be necessary and for subject 3 a spatial resolution of 4.3 mm would be needed to capture most of the information in the phase. This is in good agreement with the decay in SNR that is observed in Figure 58 and Figure 60 respectively.

The issue of a vibration causing MPE is that it will affect all shots that involve gradients that induce vibrations. The cardiac motion is only noticeable in around 20% of the images due to

minimal motion during most of the cardiac cycle, while the vibrational artifacts impact every encoding in the left/right direction.

Alternative approach to model coherent motion and navigator phase

A possible novel form of motion correction that was explored as part of this work was to create a subject specific model of MPE during the cardiac cycle and use that to create a high resolution navigator for motion correction. The basic idea of the method was that some calibration data could be acquired that enables the movement of the brainstem at different points in the cardiac to be modeled with a high amount of accuracy. Then during the actual imaging session, based on a small amount of navigator data, the correct phase information from the high resolution model could be used.

One way to formulate this problem is shown in Equation 12. In this framework, a set of basis functions that describe the shape of the brainstem motion, u, is used as one of the inputs from calibration or potentially from other a prior models. The goal is to then solve for a basis vector, v, which describes the weights of the different basis functions. uv can then be compared to navigator data, n, and the best v can be found that minimizes the error. The uv can then be used as a higher resolution version of the navigator for use in motion correction reconstruction of multi-shot diffusion weighted images.

$$\hat{v} = \min_{v} \|uv - n\|_2^2$$

Equation 12

A key part of the method is the ability to have a basis set that describes the motion of the navigators. In Figure 63 a small test data set of basis phase images is shown. The basis set comes from the phase images of a single shot PGSE diffusion scan with a 2 mm resolution. This basis set contains 7 images, one image without diffusion weighting, the other six with diffusion weightings and are a combination of 3 different diffusion directions taken at 2 different time points 80 ms apart in the

cardiac cycle. It can be seen that the different diffusion encoding directions have encoded motion in different directions as can be seen from the differences between columns 2, 3, and 4. Looking at the same direction of motion the time points share a lot of similarities, for example columns 4 and 7 have different phase patterns, however after unwrapping the phase the shape appears similar between the 2 cases.

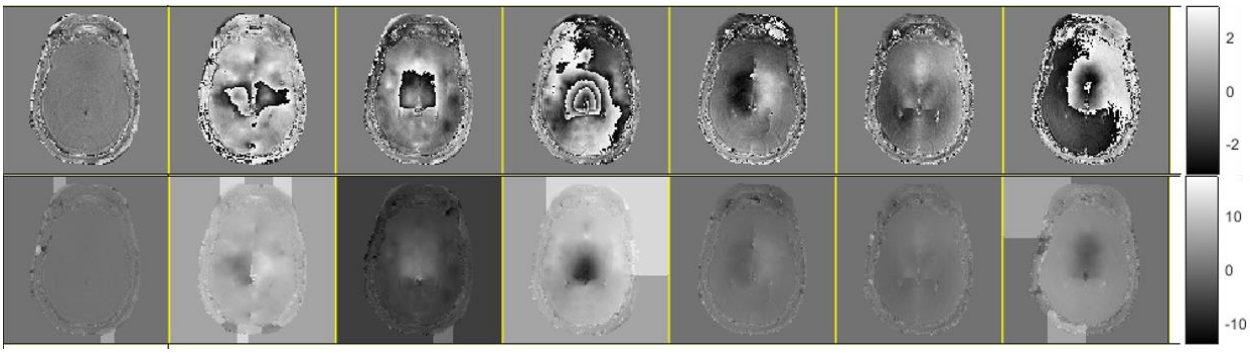

Figure 63: Potential sets of basis phase images before phase unwrapping (top), and after phase unwrapping (bottom).

This method showed a lot of initial promise as there was little variation across points acquired at the same time in the cardiac cycle, making the concept of a repeatable model promising. However, as more time points were added the performance decreased. In Figure 64 an example of the resulting phase maps derived using the proposed method is shown and compared to the phase that is achieved by just using a low resolution navigator. In this data set the basis images from Figure 63, shots 1 and 3 are from the time points used in that basis set, while shot 2 is from a time point in the cardiac cycle between the two time points. From these results it can be seen that the two methods of determining MPE produce similar results, with the basis approach having higher errors around the edges of the brain. One interesting observation is that at high resolutions there is more error in the estimated MPE in shot 2 that was not well represented in the basis set.

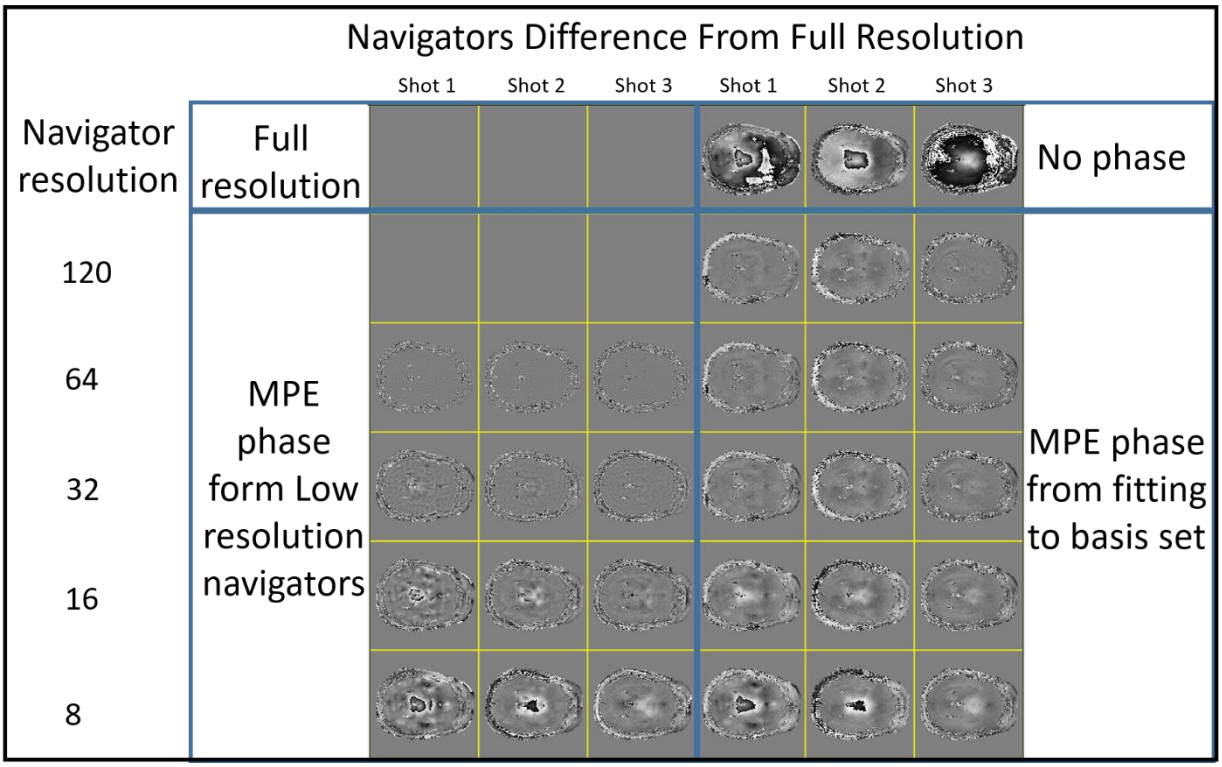

Figure 64: MPE estimation based on low resolution navigators and fitting to a basis set

To test how the estimated MPE actually impacted image reconstruction, 3 shot spiral data was simulated based on the full resolution phase image, images were then reconstructed using MPE correction based on estimates of the MPE from the basis method and the low resolution method for navigators of different resolutions. Figure 65 gives an example of one reconstruction result. Results using different phase errors showed similar results. The Low resolution navigator performed better in all cases, with much better performance at higher resolutions. The hypothesis was that at lower resolution the basis method would be able to outperform taking just the low resolution information as it is able to incorporate some higher resolution information into the MPE estimation from the basis functions themselves. This hypothesis did not turn out to be true which could be due to several reasons.

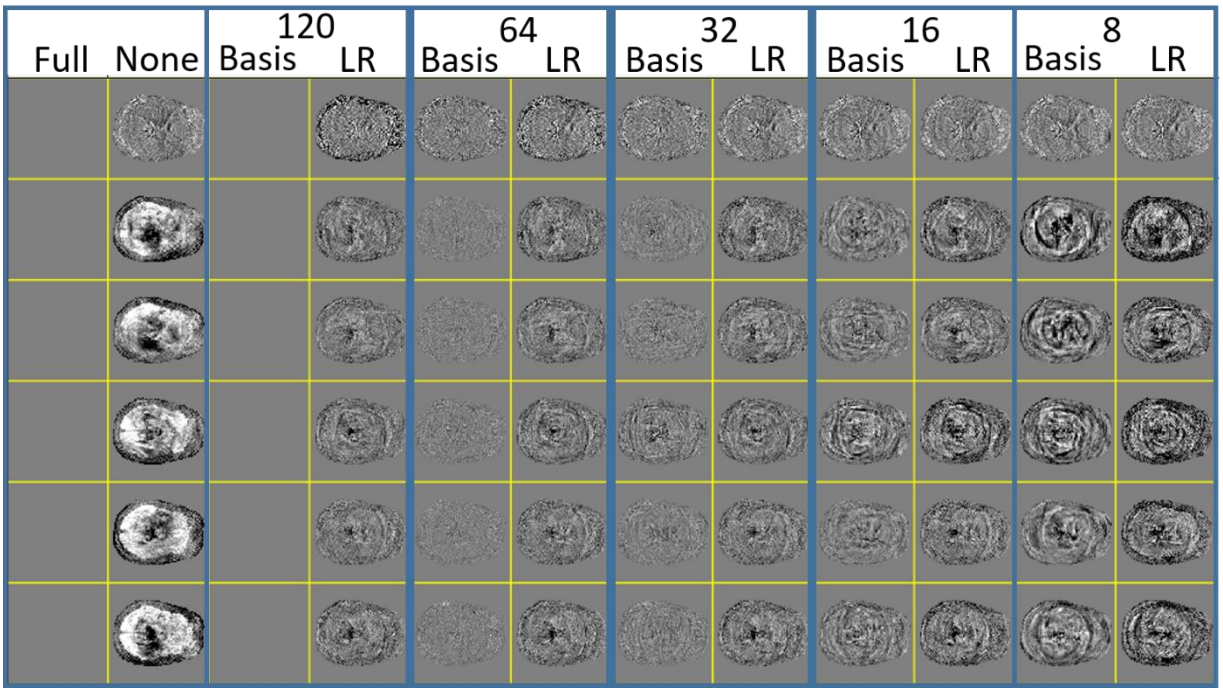

Figure 65: Difference in reconstruction of diffusion weighted images with MPE phase estimated from low resolution (LR) phase and from the proposed basis method.

One possible reason is that in the framework proposed it is hard to recover information as the basis fit is compared to the low resolution navigator. A potential improvement to this would be to use a joint basis fitting and navigator estimating operation. This may allow for a more freedom in selecting the basis vector. Using a joint approach also opens up possibilities with designing different navigator trajectories. One possible navigator approach that could be used is a variable density trajectory that allows for more sampling at the center of k-space while allowing for some higher resolution information to be incorporated into the fitting procedure.

A second area that could be causing issues is the estimation of the basis set. The example shown was contrived with sampling a small number of diffusion directions and a small part of the cardiac cycle. When attempting to fit to more different diffusion directions and more time points in the cardiac cycle, the phase error in the estimation of the MPE gets worse. This can be improved

upon by adding more basis images, however that would require more time for collection of calibration data.

Because the amount of information that ended up being needed to perform a full calibration data set got large, the method became impractical due to taking significantly more scan time than what would be acquired than simply reacquiring data. Additionally, with large amounts of calibration data the determination of the brainstem motion becomes a computationally intensive operation, making the image estimations take much longer. Overall, from our experiences, it is possible to use a brainstem model to correct for motion induced phase errors. However, in practice it is not practical, and using low resolution navigators and/or reacquiring data is more time efficient.

Conclusions

This section explored several aspects of MPE correction in diffusion weighted imaging. Through simulation the importance of b-value and gradient strength used for diffusion encoding were demonstrated. When looking at real MPE functions, the simulation and experimental results for navigator sampling had good agreement with a navigator resolution of 6-8 mm being needed in both cases. However, the experimental data also showed that there are more considerations than just the brainstem motion that need to be considered when designing a navigator for MPE correction. The good news for future work in multi-shot diffusion weighted imaging is that as hardware is improving, additional sampling requirements on navigators may be relaxed.

Chapter 6: Applying Advances in Diffusion Weighted Imaging to Magnetic Resonance Elastography[2]

Magnetic resonance elastography (MRE) is an MR imaging technique that uses motion encoding gradients to measure the propagation of shear waves [99]. With measures of the displacement caused by shear waves, MRE enables a measurement of mechanical properties such as the shear modulus and loss modulus in vivo. Changes in mechanical properties have been observed with MRE in several conditions including Alzheimer's disease [100], multiple scherosis [101], and normal pressure hydrocephalus [102].

The method to encode displacement in MRE has many similarities to the way motion is encoded in DWI. The key addition to the MRE encoding is that an external actuation is applied during the data acquisition, synchronizing motion encoding and the oscillations of the sample, making the image sensitive to the shear wave motion. The MRE acquisition uses a spin echo sequence just like the commonly used PGSE scheme in diffusion imaging, making the SNR relationships discussed in chapter 3 directly applicable to MRE as well.

In this section, the ability to use the developed acquisition approaches for diffusion weighted imaging and apply them to the area of MRE will be demonstrated. The use of both the multi-slab [103] and multi-band [104] acquisitions for use in MRE will be shown. Additionally, several considerations for correcting for coherent motion in MRE will be discussed.

Multi-slab Magnetic Resonance Imaging

In the brain, elastography, similar to diffusion imaging, traditionally used a 2D imaging sequence [105]. In practice the 2D imaging allowed for minimal spatial coverage in the slice direction due to timing constraints. The 3D multi-slab approach allows for increased spatial

[2] Several images form this section are from Johnson, C.L., et al., *3D multislab, multishot acquisition for fast, whole-brain MR elastography with high signal-to-noise efficiency.* Magn Reson Med, 2014. **71**(2): p. 477-85.

coverage to be acquired in the same amount of time if a k-space under sampling factor can be used [103].

The basics of the sequence used for 3D multi-slab imaging for MRE is very similar to the proposed sequence for diffusion imaging. The key differences used in that a navigator was placed after a second refocusing pulse in order to capture a 3D navigator. The 3D navigator allows MPE correction to be performed in all 3 dimensions. The other differences is that instead of the PGSE diffusion encoding, a motion encoding waveform with the same period as the mechanical actuation frequency was used. The pulse sequence used for 3D multi-slab MRE is shown in Figure 66.

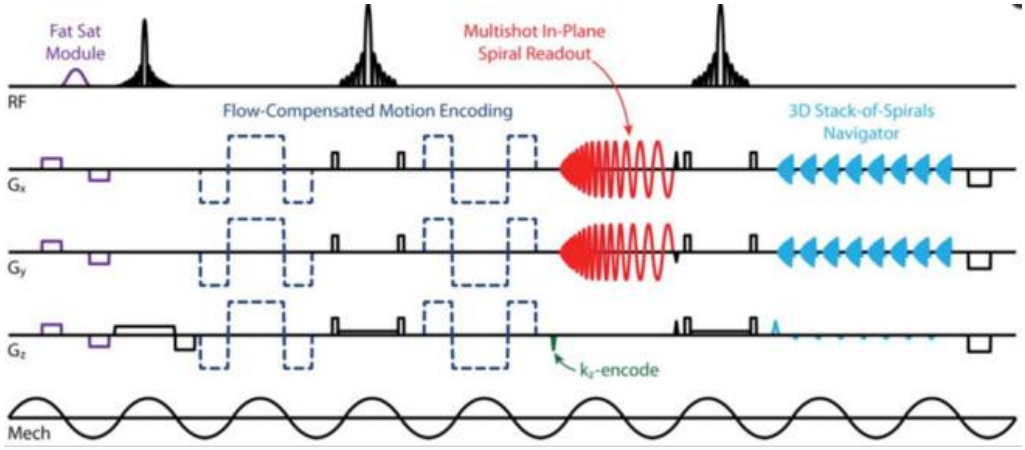

Figure 66: 3D multi-slab pulse sequence for MRE

To demonstrate the usefulness of the 3D multi-slab MRE sequence, a repeatability experiment was run. In this experiment a single subject was scanned in 6 different sessions using the developed pulse sequence. Resulting images and estimated mechanical property maps of the storage modulus, G', and loss modules, G'', from the images show high levels of repeatability, Figure 67. Looking at localized structures such as the corpus colosseum and corona radiate, which were not possible with traditional resolutions, show high levels of repeatability with a coefficient of variation of less than 10% in these localized structures [103].

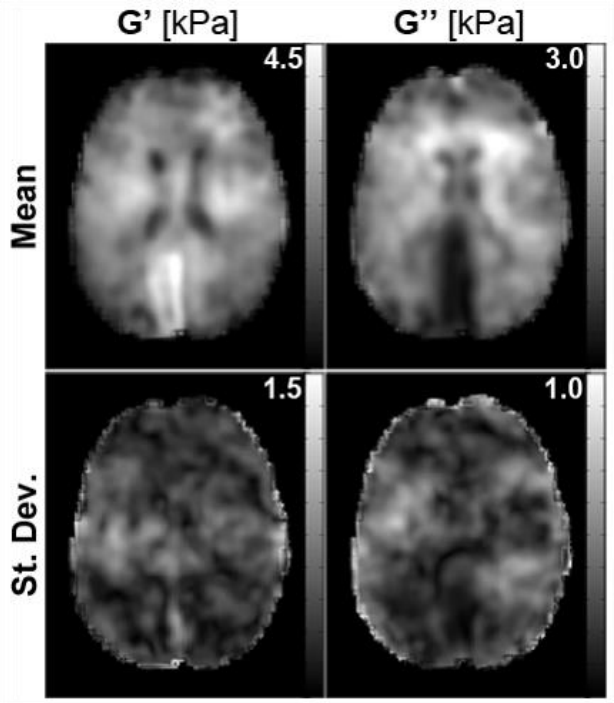

Figure 67: Mechanical property maps for a single slice from the 3D multi-slab MRE acquisition.

Multi-band Magnetic Resonance imaging

Similar to the diffusion imaging case, in multi-slab MRE there was a desire to reduce slab boundary artifacts and move toward higher acceleration factors to enable shorter scan times or higher resolutions. In order to create the MRE sequence, the diffusion gradients were replaced by the MRE encoding gradients and the timing parameters were adjusted to synchronize with the mechanical actuation. Compared to the multi-slab MRE sequence, the new sequence now uses the blipped spiral-in readout for the navigator acquisition. This eliminates the use of a second refocusing and allows the navigator to have a much lower TE, increasing the signal-to-noise ratio for navigation and improving the ability to correct for MPE. The pulse sequence used for multi-band MRE is shown in Figure 68.

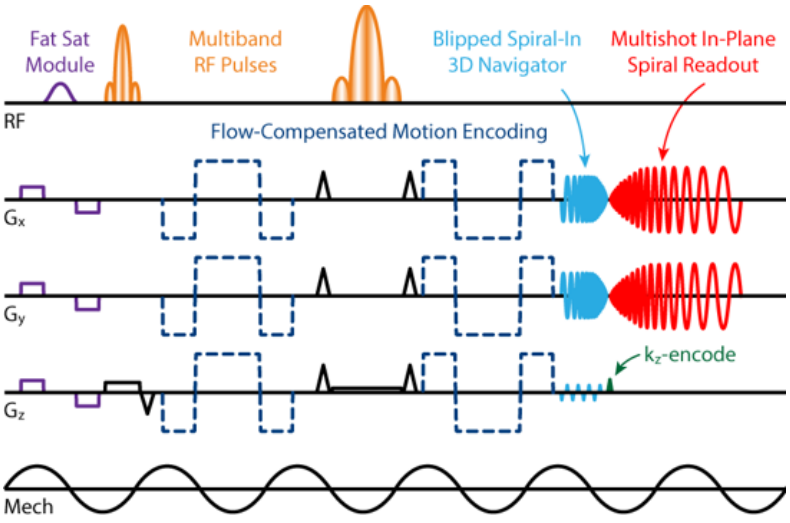

Figure 68: Multi-band MRE pulse sequence

While going to higher resolution in diffusion imaging poses a large challenge due to the loss of signal, in MRE there is a higher amount signal due to a very low amount of diffusion encoding coming from the MRE gradients. A typical MRE acquisition at 50 Hz and a gradient strength of 26 mT/m would have a b-value of less than 100 s/mm^2. Because of this, the MRE sequence has higher SNR than the diffusion sequence, allowing for more options for accelerating the acquisition by using data undersampling. Examples from different undersampling patterns can be seen in Figure 69. In Figure 69 a fully sampled MRE data set was acquired and then retrospectively undersampling by delimited certain shots to create different undersampling patterns. The fully sampled data set contained a 4 shot spiral in plane with 4 planes of k-space acquired, giving a total of 16 shots used. The sampling patterns used in this case were a reduction factor of 4 in the in-plane direction, a reduction factor of 4 in the slice direction, and an undersampling factor of 2 in both the in-plane and slice direction, resulting in 3 trajectories with a total reduction factor of 4.

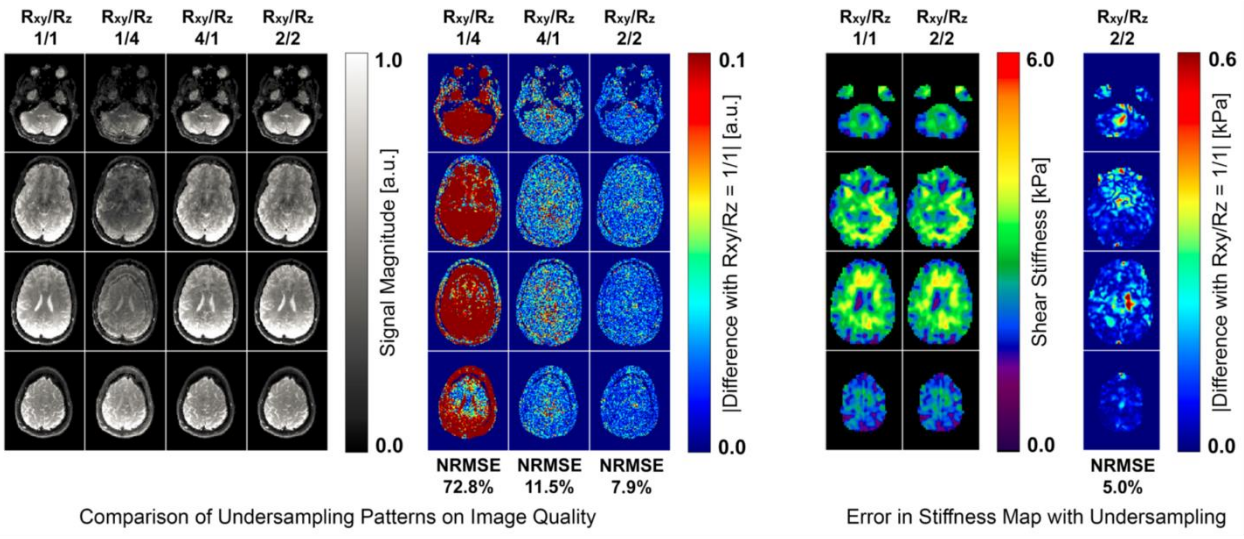

Figure 69: Multi-band MRE using differnet k-sapce undersampling schemes.

The resulting undersampled images varied in the resulting image quality despite having the same amount of total data used to reconstruct them. This emphasizes the importance that k-space sampling plays in being able to reconstruct accurate images from underdamped data. The image with a reduction factor of 2 in both the slice and in-plane direction produced the best result that gave very little error compared to the fully sampled case. Achieve a reduction factor of 2 in the slice direction was not possible with the multi-slab approach.

Motion Correction in MRE

MRE is susceptible to the same sort of motion induced phase errors that are found in diffusion weighted imaging. However, in human brain MRE the b-value is less than 100 s/mm^2, which based on the analysis in chapter 5 makes the sequence much less susceptible to motion induced phase errors than standard diffusion weighted imaging, making the requirements for navigator sampling on MRE potentially much lower.

Different than the magnitude image from DWI, in MRE the signal of interest is encoded in the phase of the image. The phase of the image is also the location of the MPE error signal. In order to correct for MPE in MRE, the MRE signal needs to be separated from the MPE signal.

This is challenging as the two phase signals have similar spatial resolution and cannot be separated in k-space. Because the true desired phase from the shear waves is unknown, one way of performing the phase correction is to take the average of all the navigators and use that as the reference phase to correct the image phase of all the navigators. This makes sense due to the distribution of phase errors across the multiple navigator data sets. This has been shown to work well with our acquisitions. Further investigation is required to determine the minimum number of shots that are needed in order to perform this type of motion correction.

Conclusions

The modification of the MRE sequence to use the multi-band and multi-slab approaches represent several key points about the methodological improvements that have been developed in this thesis for motion encoded imaging. The developed methods are extensible to other areas of MR research, providing tradeoffs with increased SNR efficiency, spatial coverage, and spatial resolution. While methods were created were designed specifically for use in measuring diffusion, the lessons learned were practical and able to provide a great impact to MRE. In the area of MRE the methods provide a large step forward in data quality, allowing higher resolutions and higher SNR than were previously capable with standard approaches.

Chapter 7: Conclusion and Future Directions

Summary of contributions

High-resolution diffusion weighted images are increasingly needed as applications that are capable of taking advantage of the increased resolution have been developed. The high resolution aids in the delineation of fine neural structures, reduces partial volume effects, simplifies models of diffusion within a voxel, and can be applied to other motion-encoded applications. This thesis focused on developing acquisitions that are able to achieve high resolution diffusion weighted images with high SNR efficiency on standard clinical MRI hardware [80, 106].

Several of the main contributions include:

Development of an efficient pulse sequence for acquisition of high spatial resolution diffusion weighted imaging on a clinical MRI scanner: This work has compared SNR gains from center-out k-space trajectories compared to standard EPI trajectories, especially focusing on the impact of moving to higher resolutions. In addition, we have examined the SNR tradeoffs of 3D vs 2D imaging. Finally, we have addressed the negative impact of slice profiles on 3D slabs, transitioning to a multi-band excitation that evenly distributes slice profile imperfections across the entire volume. Through these developments, we have enabled higher spatial resolution DTI scans than have ever been possible before, achieving 0.8 mm isotropic resolution for whole brain coverage in a human brain on a clinical 3 T scanner. A recent abstract has pushed data on the specialized human connectome scanner to acquire data at 0.66 mm isotropic resolution, but that is with a system with 300 mT/m gradients [107]. Further, we have addressed tradeoffs between SNR efficiency and susceptibility-induced distortions using long data readouts and magnetic field inhomogeneity corrected image reconstruction.

Development of navigators that do not impact scan time. In multi-shot navigated diffusion weighted imaging, navigator data were typically acquired after a second refocusing pulse. This

cost time and resulted in a lower SNR in the navigator data. In this work I created a navigator that could be placed before the data readout without impact to the imaging acquisition. Resulting in a more efficient sequence with a higher SNR navigator.

Development of guidelines for navigator sampling. Previously there were very few guidelines for the requirements on what type of motion-induced phase errors could be corrected for in diffusion weighted imaging. In this work, we examined in detail the spatial resolution properties of MPE and examined the necessary spatial resolution of navigators for successful correction. In addition to real data, we also examined simulations that allow the results to be extended to other b-values and gradient strengths.

Application of 3D imaging techniques to MRE. MRE had traditionally been limited in the coverage it could achieve due to requirements on synchronization between motion encoding gradients and mechanical actuation. By applying 3D acquisitions approaches to MRE the coverage of MRE exams were increased allowing for the technique to be used to acquire full brain coverage [103]. Additionally, through the adoption of multi-band approaches for MRE, the scan time was able to be cut in half [104].

Future work

This work takes advantage of many different concepts in MR in order to create an imaging approach that is able to achieve high resolutions with high SNR efficiency. Concurrently during these sequence developments, there have been many advances in MR scanner hardware. While the proposed approach reaches SNR efficiency regardless of hardware, there are even more opportunities that are made available by advances in hardware, such as the connectome scanner and the new class of clinical scanners in the Prisma platform.

The two biggest advances in hardware are an increase in the maximum gradient strength and an increase in the number of receiver coils. The in vivo data collected in this work was all

collected on a MR scanner (3 T Siemens Trio) with a maximum gradient strength of 26 mT/m. While this is a fairly standard value over the past 10 years, there has been a recent push to increase the gradient strength. Because of this, newer clinical systems are now often capable of achieving 80 mT/m gradients with some research systems able to go even higher [69]. The availability of the newer systems will allow the tests that were only done in simulation for the higher gradient strengths to be performed in vivo.

The other major hardware improvement of more RF receiver elements presents many new opportunities for parallel imaging. In conjunction with developing methods for k-space sampling [93], new methods are being made possible for achieving high acceleration factors in parallel imaging. One possibility that this has is to switch from multi-band or multi-slab approach to a purely 3D imaging approach. In this approach the entire imaging volume would all be excited simultaneously. Doing this would eliminate any artifacts that could be associated with having multiple excitations of different volumes. This would also greatly reduce the RF power needed to perform excitation as a shaped RF pulse will no longer be needed to excite a specific frequency range. This also opens opportunities to more easily incorporate 3D models, such as regularization penalties, across the entire object at once. On current systems this is currently not practical as even at low spatial resolutions, this would require images to be acquired with a reduction factor of at least 16 to be practical from scan time perspective, which is not possible on many systems.

This work all took advantage of the SENSE formulation for parallel imaging. However there has recently been more work published that uses forms of non-Cartesian GRAPPA for parallel imaging reconstruction [66, 67]. The use of GRAPPA for reconstruction could have the possibility of making reconstruction times faster and is an area that should be investigated more

closely. In conjunction with that several GRAPPA based methods are being developed for performing image MPE correction.

A final area that would be interesting for future work is the simultaneous acquisition of diffusion data with MRE. This has been done on an animal imaging system [108], but was formerly not practical for achieving high b-values on clinical human systems. With higher gradient strengths becoming available, the simultaneous acquisition of MRE and diffusion contrasts may now be possible. This advancement would have great clinical impact as both types of data sets could now be acquired in a single scan.

References

1. Cooley, J.W. and J.W. Tukey, *An Algorithm for Machine Calculation of Complex Fourier Series.* Mathematics of Computation, 1965. **19**(90): p. 297-&.
2. Jackson, J.I., et al., *Selection of a convolution function for Fourier inversion using gridding [computerised tomography application].* IEEE Trans Med Imaging, 1991. **10**(3): p. 473-8.
3. Matej, S. and I. Bajla, *A high-speed reconstruction from projections using direct Fourier method with optimized parameters-an experimental analysis.* IEEE Trans Med Imaging, 1990. **9**(4): p. 421-9.
4. Pruessmann, K.P., et al., *SENSE: sensitivity encoding for fast MRI.* Magn Reson Med, 1999. **42**(5): p. 952-62.
5. Sutton, B.P., D.C. Noll, and J.A. Fessler, *Fast, iterative image reconstruction for MRI in the presence of field inhomogeneities.* IEEE Trans Med Imaging, 2003. **22**(2): p. 178-88.
6. Lange, K., *Convergence of Em Image-Reconstruction Algorithms with Gibbs Smoothing.* Ieee Transactions on Medical Imaging, 1990. **9**(4): p. 439-446.
7. Stejskal, E.O. and J.E. Tanner, *Spin Diffusion Measurements: Spin Echoes in the Presence of a Time-Dependent Field Gradient.* Journal of Chemical Physics, 1965. **42**(1): p. 288-+.
8. Merboldt, K.D., W. Hanicke, and J. Frahm, *Self-Diffusion Nmr Imaging Using Stimulated Echoes.* Journal of Magnetic Resonance, 1985. **64**(3): p. 479-486.
9. Taylor, D.G. and M.C. Bushell, *The Spatial-Mapping of Translational Diffusion-Coefficients by the Nmr Imaging Technique.* Physics in Medicine and Biology, 1985. **30**(4): p. 345-349.
10. Warach, S., J.F. Dashe, and R.R. Edelman, *Clinical outcome in ischemic stroke predicted by early diffusion-weighted and perfusion magnetic resonance imaging: a preliminary analysis.* J Cereb Blood Flow Metab, 1996. **16**(1): p. 53-9.

11. Barber, P.A., et al., *Prediction of stroke outcome with echoplanar perfusion- and diffusion-weighted MRI.* Neurology, 1998. **51**(2): p. 418-26.
12. Mori, S. and P.C.M. van Zijl, *Fiber tracking: principles and strategies - a technical review.* Nmr in Biomedicine, 2002. **15**(7-8): p. 468-480.
13. Lori, N.F., et al., *Diffusion tensor fiber tracking of human brain connectivity: aquisition methods, reliability analysis and biological results.* Nmr in Biomedicine, 2002. **15**(7-8): p. 493-515.
14. Tanner, J.E. and E.O. Stejskal, *Restricted Self-Diffusion of Protons in Colloidal Systems by Pulsed-Gradient Spin-Echo Method.* Journal of Chemical Physics, 1968. **49**(4): p. 1768-+.
15. Reese, T.G., et al., *Reduction of eddy-current-induced distortion in diffusion MRI using a twice-refocused spin echo.* Magn Reson Med, 2003. **49**(1): p. 177-82.
16. Finsterbusch, J., *Eddy-current compensated diffusion weighting with a single refocusing RF pulse.* Magn Reson Med, 2009. **61**(3): p. 748-54.
17. Schachter, M., et al., *Measurements of restricted diffusion using an oscillating gradient spin-echo sequence.* Journal of Magnetic Resonance, 2000. **147**(2): p. 232-237.
18. Merboldt, K.D., W. Hanicke, and J. Frahm, *Diffusion Imaging Using Stimulated Echoes.* Magnetic Resonance in Medicine, 1991. **19**(2): p. 233-239.
19. Kidwell, C.S., et al., *Diffusion MRI in patients with transient ischemic attacks.* Stroke, 1999. **30**(6): p. 1174-80.
20. Neumann-Haefelin, T., et al., *Diffusion- and perfusion-weighted MRI. The DWI/PWI mismatch region in acute stroke.* Stroke, 1999. **30**(8): p. 1591-7.
21. Song, S.K., et al., *Diffusion tensor imaging detects and differentiates axon and myelin degeneration in mouse optic nerve after retinal ischemia.* Neuroimage, 2003. **20**(3): p. 1714-22.

22. Song, S.K., et al., *Dysmyelination revealed through MRI as increased radial (but unchanged axial) diffusion of water.* Neuroimage, 2002. **17**(3): p. 1429-1436.
23. Wang, Y., et al., *Quantification of increased cellularity during inflammatory demyelination.* Brain, 2011. **134**(Pt 12): p. 3590-601.
24. Basser, P.J., J. Mattiello, and D. LeBihan, *MR diffusion tensor spectroscopy and imaging.* Biophys J, 1994. **66**(1): p. 259-67.
25. Holtrop, J.L., et al., *Investigating Age-related changes in fine motor control across different effectors and the impact of white matter integrity.* Neuroimage, 2014. **96**: p. 81-87.
26. Zhang, H., et al., *NODDI: practical in vivo neurite orientation dispersion and density imaging of the human brain.* Neuroimage, 2012. **61**(4): p. 1000-16.
27. Assaf, Y. and P.J. Basser, *Composite hindered and restricted model of diffusion (CHARMED) MR imaging of the human brain.* Neuroimage, 2005. **27**(1): p. 48-58.
28. Le Bihan, D., et al., *MR imaging of intravoxel incoherent motions: application to diffusion and perfusion in neurologic disorders.* Radiology, 1986. **161**(2): p. 401-7.
29. Echaniz-Laguna, A., et al., *Diffusion weighted MR imaging of denervated skeletal muscle: An experimental and clinical study.* Neurology, 2008. **70**(11): p. A218-A218.
30. Yanagisawa, O., et al., *Diffusion-weighted magnetic resonance imaging of human skeletal muscles: gender-, age- and muscle-related differences in apparent diffusion coefficient.* Magnetic Resonance Imaging, 2009. **27**(1): p. 69-78.
31. Yao, L. and U. Sinha, *Imaging the microcirculatory proton fraction of muscle with diffusion-weighted echo-planar imaging.* Academic Radiology, 2000. **7**(1): p. 27-32.
32. Kim, J.Y., et al., *Apparent diffusion coefficient of breast cancer and normal fibroglandular tissue in diffusion-weighted imaging: the*

effects of menstrual cycle and menopausal status. Breast Cancer Research and Treatment, 2016. **157**(1): p. 31-40.
33. Razek, A.A.K.A., et al., *Assessment of axillary lymph nodes in patients with breast cancer with diffusion-weighted MR imaging in combination with routine and dynamic contrast MR imaging.* Breast Cancer, 2016. **23**(3): p. 525-532.
34. Zhao, M., et al., *Early detection of treatment response by diffusion-weighted 1H-NMR spectroscopy in a murine tumour in vivo.* Br J Cancer, 1996. **73**(1): p. 61-4.
35. Qayyum, A., et al., *Evaluation of Liver Fibrosis With Diffusion-Weighted Imaging in Nonalcoholic Fatty Liver Disease: The affect of analysis location on histopathologic correlation.* American Journal of Roentgenology, 2009. **192**(5).
36. Vilgrain, V., et al., *Diffusion-weighted MR imaging of the liver.* Journal De Radiologie, 2010. **91**(3): p. 381-393.
37. Laissy, J.P., et al., *Cardiac Diffusion-weighted MR Imaging in Recent, Subacute, and Chronic Myocardial Infarction: A Pilot Study.* Journal of Magnetic Resonance Imaging, 2013. **38**(6): p. 1377-1387.
38. Ryoo, S.M., et al., *Predicting Outcome With Diffusion-Weighted Imaging in Cardiac Arrest Patients Receiving Hypothermia Therapy: Multicenter Retrospective Cohort Study.* Critical Care Medicine, 2015. **43**(11): p. 2370-2377.
39. Andersson, J.L. and S.N. Sotiropoulos, *An integrated approach to correction for off-resonance effects and subject movement in diffusion MR imaging.* Neuroimage, 2016. **125**: p. 1063-78.
40. Liu, C., et al., *Self-navigated interleaved spiral (SNAILS): application to high-resolution diffusion tensor imaging.* Magn Reson Med, 2004. **52**(6): p. 1388-96.
41. Liu, C., M.E. Moseley, and R. Bammer, *Simultaneous phase correction and SENSE reconstruction for navigated multi-shot DWI*

with non-cartesian k-space sampling. Magn Reson Med, 2005. **54**(6): p. 1412-22.
42. Ordidge, R.J., et al., *Correction of motional artifacts in diffusion-weighted MR images using navigator echoes.* Magnetic resonance imaging, 1994. **12**(3): p. 455-460.
43. Truong, T.K., N.K. Chen, and A.W. Song, *Inherent correction of motion-induced phase errors in multishot spiral diffusion-weighted imaging.* Magn Reson Med, 2012. **68**(4): p. 1255-61.
44. Truong, T.K. and A. Guidon, *High-resolution multishot spiral diffusion tensor imaging with inherent correction of motion-induced phase errors.* Magn Reson Med, 2014. **71**(2): p. 790-6.
45. Ulug, A.M., P.B. Barker, and P.C. van Zijl, *Correction of motional artifacts in diffusion-weighted images using a reference phase map.* Magn Reson Med, 1995. **34**(3): p. 476-80.
46. Van, A.T., D. Hernando, and B.P. Sutton, *Motion-induced phase error estimation and correction in 3D diffusion tensor imaging.* IEEE Trans Med Imaging, 2011. **30**(11): p. 1933-40.
47. Van, A.T., et al., *K-space and image space combination for motion artifact correction in multicoil multishot diffusion weighted imaging.* Conf Proc IEEE Eng Med Biol Soc, 2008. **2008**: p. 1675-8.
48. Wang, F.N., et al., *PROPELLER EPI: an MRI technique suitable for diffusion tensor imaging at high field strength with reduced geometric distortions.* Magn Reson Med, 2005. **54**(5): p. 1232-40.
49. Zhang, Z., et al., *Self-feeding MUSE: a robust method for high resolution diffusion imaging using interleaved EPI.* Neuroimage, 2015. **105**: p. 552-60.
50. Benner, T., A.J.W. van der Kouwe, and A.G. Sorensen, *Diffusion Imaging With Prospective Motion Correction and Reacquisition.* Magnetic Resonance in Medicine, 2011. **66**(1): p. 154-167.
51. Bosak, E. and P.R. Harvey, *Navigator motion correction of diffusion weighted 3D SSFP imaging.* Magnetic Resonance Materials in Physics Biology and Medicine, 2001. **12**(2-3): p. 167-176.

52. Dietrich, O., et al., *Reducing motion artefacts in diffusion-weighted MRI of the brain: efficacy of navigator echo correction and pulse triggering.* Neuroradiology, 2000. **42**(2): p. 85-91.
53. Gmitro, A., T. Trouard, and Y. Sabharwal, *Strategies for motion correction in diffusion-weighted MRI.* Information Processing in Medical Imaging, 1995. **3**: p. 13-26.
54. Guo, H., et al., *POCS-Enhanced Inherent Correction of Motion-Induced Phase Errors (POCS-ICE) for High-Resolution Multishot Diffusion MRI.* Magnetic Resonance in Medicine, 2016. **75**(1): p. 169-180.
55. Herbst, M., et al., *Prospective motion correction with continuous gradient updates in diffusion weighted imaging.* Magnetic Resonance in Medicine, 2012. **67**(2): p. 326-338.
56. O'Halloran, R.L., et al., *Model for the correction of motion-induced phase errors in multishot diffusion-weighted-MRI of the head: Are cardiac-motion-induced phase errors reproducible from beat-to-beat?* Magnetic Resonance in Medicine, 2012. **68**(2): p. 430-440.
57. Trouard, T.P., et al., *Analysis and comparison of motion-correction techniques in diffusion-weighted imaging.* Jmri-Journal of Magnetic Resonance Imaging, 1996. **6**(6): p. 925-935.
58. Wu, W., S. Fang, and H. Guo, *[Joint correction for motion artifacts and off-resonance artifacts in multi-shot diffusion magnetic resonance imaging].* Sheng Wu Yi Xue Gong Cheng Xue Za Zhi, 2014. **31**(3): p. 657-61, 670.
59. Porter, D.A. and R.M. Heidemann, *High resolution diffusion-weighted imaging using readout-segmented echo-planar imaging, parallel imaging and a two-dimensional navigator-based reacquisition.* Magn Reson Med, 2009. **62**(2): p. 468-75.
60. Pipe, J.G., V.G. Farthing, and K.P. Forbes, *Multishot diffusion-weighted FSE using PROPELLER MRI.* Magn Reson Med, 2002. **47**(1): p. 42-52.

61. Butts, K., et al., *Diffusion-weighted interleaved echo-planar imaging with a pair of orthogonal navigator echoes.* Magn Reson Med, 1996. **35**(5): p. 763-70.
62. de Crespigny, A.J., et al., *Navigated diffusion imaging of normal and ischemic human brain.* Magn Reson Med, 1995. **33**(5): p. 720-8.
63. Atkinson, D., et al., *Sampling and reconstruction effects due to motion in diffusion-weighted interleaved echo planar imaging.* Magn Reson Med, 2000. **44**(1): p. 101-9.
64. Anderson, A.W. and J.C. Gore, *Analysis and correction of motion artifacts in diffusion weighted imaging.* Magn Reson Med, 1994. **32**(3): p. 379-87.
65. Nunes, R.G., P. Jezzard, and S. Clare, *Investigations on the efficiency of cardiac-gated methods for the acquisition of diffusion-weighted images.* Journal of Magnetic Resonance, 2005. **177**(1): p. 102-110.
66. Liu, W., et al., *DWI using navigated interleaved multishot EPI with realigned GRAPPA reconstruction.* Magnetic resonance in medicine, 2016. **75**(1): p. 280-286.
67. Ma, X., et al., *Improved multi-shot diffusion imaging using GRAPPA with a compact kernel.* NeuroImage, 2016.
68. !!! INVALID CITATION !!! {Frost, 2014 #5;Engstrom, 2013 #6;Johnson, 2014 #7;Setsompop, 2013 #8;Cerjanic, 2016 #225 }.
69. Setsompop, K., et al., *Pushing the limits of in vivo diffusion MRI for the Human Connectome Project.* Neuroimage, 2013. **80**: p. 220-33.
70. Buonocore, M.H. and L.S. Gao, *Ghost artifact reduction for echo planar imaging using image phase correction.* Magnetic Resonance in Medicine, 1997. **38**(1): p. 89-100.
71. King, K.F., T.K. Foo, and C.R. Crawford, *Optimized gradient waveforms for spiral scanning.* Magn Reson Med, 1995. **34**(2): p. 156-60.

72. Stanisz, G.J., et al., *T1, T2 relaxation and magnetization transfer in tissue at 3T.* Magn Reson Med, 2005. **54**(3): p. 507-12.
73. Engstrom, M. and S. Skare, *Diffusion-weighted 3D multislab echo planar imaging for high signal-to-noise ratio efficiency and isotropic image resolution.* Magn Reson Med, 2013. **70**(6): p. 1507-14.
74. Engstrom, M., et al., *On the signal-to-noise ratio efficiency and slab-banding artifacts in three-dimensional multislab diffusion-weighted echo-planar imaging.* Magn Reson Med, 2015. **73**(2): p. 718-25.
75. Pipe, J., *Pulse Sequences for Diffusion-weighted MRI.* Diffusion Mri: From Quantitative Measurement to in Vivo Neuroanatomy, 2009: p. 11-35.
76. Frost, R., et al., *Scan time reduction for readout-segmented EPI using simultaneous multislice acceleration: Diffusion-weighted imaging at 3 and 7 Tesla.* Magnetic Resonance in Medicine, 2015. **74**(1): p. 136-149.
77. Ordidge, R.J., et al., *Snapshot head imaging at 0.5 T using the echo planar technique.* Magn Reson Med, 1988. **8**(1): p. 110-5.
78. Papadakis, N.G., et al., *Gradient preemphasis calibration in diffusion-weighted echo-planar imaging.* Magn Reson Med, 2000. **44**(4): p. 616-24.
79. Ordidge, R.J., et al., *Correction of motional artifacts in diffusion-weighted MR images using navigator echoes.* Magn Reson Imaging, 1994. **12**(3): p. 455-60.
80. Holtrop, J.L. and B.P. Sutton, *High spatial resolution diffusion weighted imaging on clinical 3 T MRI scanners using multislab spiral acquisitions.* Journal of Medical Imaging, 2016. **3**(2): p. 023501-023501.
81. Pauly, J., et al., *Parameter relations for the Shinnar-Le Roux selective excitation pulse design algorithm [NMR imaging].* IEEE Trans Med Imaging, 1991. **10**(1): p. 53-65.

82. Sutton, B.P., et al., *Faster dynamic imaging of speech with field inhomogeneity corrected spiral fast low angle shot (FLASH) at 3 T.* J Magn Reson Imaging, 2010. **32**(5): p. 1228-37.
83. Fessler, J.A., D. Yeo, and D.C. Noll, *Regularized fieldmap estimation in MRI.* 2006 3rd Ieee International Symposium on Biomedical Imaging: Macro to Nano, Vols 1-3, 2006: p. 706-709.
84. Zhang, Y., M. Brady, and S. Smith, *Segmentation of brain MR images through a hidden Markov random field model and the expectation-maximization algorithm.* IEEE Trans Med Imaging, 2001. **20**(1): p. 45-57.
85. Jenkinson, M., et al., *Improved optimization for the robust and accurate linear registration and motion correction of brain images.* Neuroimage, 2002. **17**(2): p. 825-41.
86. Jenkinson, M. and S. Smith, *A global optimisation method for robust affine registration of brain images.* Med Image Anal, 2001. **5**(2): p. 143-56.
87. Behrens, T.E., et al., *Characterization and propagation of uncertainty in diffusion-weighted MR imaging.* Magn Reson Med, 2003. **50**(5): p. 1077-88.
88. Lebel, C., T. Benner, and C. Beaulieu, *Six is enough? Comparison of diffusion parameters measured using six or more diffusion-encoding gradient directions with deterministic tractography.* Magn Reson Med, 2012. **68**(2): p. 474-83.
89. Feinberg, D.A. and K. Setsompop, *Ultra-fast MRI of the human brain with simultaneous multi-slice imaging.* J Magn Reson, 2013. **229**: p. 90-100.
90. Setsompop, K., et al., *Improving diffusion MRI using simultaneous multi-slice echo planar imaging.* Neuroimage, 2012. **63**(1): p. 569-80.
91. Setsompop, K., et al., *Blipped-controlled aliasing in parallel imaging for simultaneous multislice echo planar imaging with reduced g-factor penalty.* Magn Reson Med, 2012. **67**(5): p. 1210-24.

92. Wong, E., *Optimized phase schedules for minimizing peak RF power in simultaneous multi-slice RF excitation pulses.* In Proceedings of the 20th Annual Meeting of ISMRM, Melbourne, Australia, 2012: p. 2209.
93. Deng, W., B. Zahneisen, and V.A. Stenger, *Rotated stack-of-spirals partial acquisition for rapid volumetric parallel MRI.* Magn Reson Med, 2015.
94. Forbes, K.P., et al., *Improved image quality and detection of acute cerebral infarction with PROPELLER diffusion-weighted MR imaging.* Radiology, 2002. **225**(2): p. 551-5.
95. Wirestam, R., et al., *Theoretical and experimental evaluation of phase-dispersion effects caused by brain motion in diffusion and perfusion MR imaging.* Jmri-Journal of Magnetic Resonance Imaging, 1996. **6**(2): p. 348-355.
96. Frost, R., et al., *3D multi-slab diffusion-weighted readout-segmented EPI with real-time cardiac-reordered K-space acquisition.* Magn Reson Med, 2014. **72**(6): p. 1565-79.
97. Gallichan, D., et al., *TREMR: Table-resonance elastography with MR.* Magn Reson Med, 2009. **62**(3): p. 815-21.
98. Gallichan, D., et al., *Addressing a systematic vibration artifact in diffusion-weighted MRI.* Hum Brain Mapp, 2010. **31**(2): p. 193-202.
99. Muthupillai, R., et al., *Magnetic-Resonance Elastography by Direct Visualization of Propagating Acoustic Strain Waves.* Science, 1995. **269**(5232): p. 1854-1857.
100. Murphy, M.C., et al., *Decreased Brain Stiffness in Alzheimer's Disease Determined by Magnetic Resonance Elastography.* Journal of Magnetic Resonance Imaging, 2011. **34**(3): p. 494-498.
101. Streitberger, K.J., et al., *Brain Viscoelasticity Alteration in Chronic-Progressive Multiple Sclerosis.* Plos One, 2012. **7**(1).
102. Freimann, F.B., et al., *Alteration of brain viscoelasticity after shunt treatment in normal pressure hydrocephalus.* Neuroradiology, 2012. **54**(3): p. 189-196.

103. Johnson, C.L., et al., *3D multislab, multishot acquisition for fast, whole-brain MR elastography with high signal-to-noise efficiency.* Magn Reson Med, 2014. **71**(2): p. 477-85.
104. Johnson, C.L., et al., *Brain MR elastography with multiband excitation and nonlinear motion-induced phase error correction.* In Proceedings of the 24th Annual Meeting of ISMRM, Singapore, 2016.
105. Johnson, C.L., et al., *Magnetic resonance elastography of the brain using multishot spiral readouts with self-navigated motion correction.* Magn Reson Med, 2013. **70**(2): p. 404-12.
106. Holtrop, J.L. and B.P. Sutton, *Diffusion Weighted Imaging Using Multi-shot Spiral with a Simultaneous Multi-slice Excitation.* In Proceedings of the 23rd Annual Meeting of ISMRM, Toronto, Canada, 2015.
107. Setsompop, K., et al., *Generalized SLIce Dithered Enhanced Resolution Simultaneous MultiSlice (gSlider-SMS) to increase volume encoding, SNR and partition profile fidelity in high-resolution diffusion imaging.* In Proceedings of the 24th Annual Meeting of ISMRM, Singapore, 2016.
108. Yin, Z., R.L. Magin, and D. Klatt, *Simultaneous MR elastography and diffusion acquisitions: diffusion-MRE (dMRE).* Magn Reson Med, 2014. **71**(5): p. 1682-8.